COMPUTATIONAL STUDY OF ANTENNA COUPLING AND WAVE PROPAGATION IN HELICON PLASMA SOURCES

by

Igor V. Kamenski

26 March 1998

A thesis submitted for the degree
of Doctor of Philosophy of

the Australian National University

The thesis represents my own original research work. All authorities and sources consulted have been acknowledged.

Igor V. Kamenski
26 March 1998

Abstract

A magnetohydrodynamic numerical model, based on the finite element method, is employed to analyze the antenna radiation resistance and wave dispersion in high density, high magnetic field helicon wave driven plasma sources. The radiation resistances of commonly used antennas are compared. The effects on the radiation resistance of frequency, plasma density, density profile and system dimensions are investigated. It is shown that the plasma density gradient tends to suppress the excitation of negative azimuthal modes. The wavefield structure also demonstrates experimentally observed features such as the beat patterns of copropagating radial modes. Good agreement was found between the model and experimental measurements of the wave dispersion and antenna radiation resistance in BASIL.

A new full-wave cylindrical kinetic code UFEM, optimized specifically for helicon plasma sources, has been developed and benchmarked. Its numerical scheme is suitable for calculations in the lower hybrid frequency range where helicon sources typically operate. Comparison between the MHD and kinetic models demonstrated that the MHD model is quite accurate in the computation of the radiation resistance and wave dispersion (but not the wave dissipation) in high density sources. In low density sources both helicon and Trivelpiece-Gould waves are important. It is also suggested that the excitation of global eigenmodes can be responsible for L – H mode transitions in H-1NF heliac.

The findings highlight the importance of realistic computer modelling in formulating a self-consistent model of helicon discharge physics.

Contributions

Most of the results presented in this thesis were obtained in close collaboration with the project supervisor, Dr G. G. Borg. Chapter 2 is based mainly on Ref. [77] and Chapter 4 — on Ref. [78]. Both articles (almost entirely based on my material) were written jointly with Dr Borg. Experimental results obtained in BASIL, which are used in Chapter 3 for comparison with the MHD model, were obtained by Mr D. A. Schneider. Chapter 3 is based mainly on the Ref. [112] also written jointly with Dr Borg. I use pieces of text written by Dr Borg for the above three publications throughout the thesis.

All computer codes used in this thesis were designed by the author, as well as most of the theoretical basis for them (except where stated). All results obtained with the use of these codes were obtained by the author except those produced by the code ISMENE which were used for benchmarking in § 4.6 and which were obtained by Dr Borg.

All other contributions are acknowledged.

Acknowledgements

First, I would like to express my appreciation to the staff of the Plasma Research Laboratory of the ANU who offered me consistent help in every aspect, necessary to undertake this work, as well as sufficient "degree of freedom" to undertake my own research and develop my own experience. This created an excellent and very stimulating environment for the project.

I especially would like to thank Dr G. G. Borg (the Project Supervisor). Among the staff of the PRL, he contributed most of all to this work. His excellent knowledge of plasma science, in both experimental and theoretical aspects, were of irreplaceable value. He provided me a guiding influence during the project and gave me many helpful ideas and suggestions for this work. I appreciated the generosity with which he was always ready to discuss my numerous queries, his limitless patience in correcting my English, and his kindness in spending his time to proof read this thesis (as well as my other papers).

I am sincerely grateful to Prof S. M. Hamberger who has invited me to the PRL and arranged my graduate study here. I appreciate a great deal of his assistance in obtaining the ANU PhD Scholarship and the Overseas Postgraduate Research Scholarship which gave me the opportunity to continue research in the field of laboratory plasma after 7 years break devoted mainly to ionospheric research. I owe Prof Hamberger a great deal indeed, and wish to express my gratitude here.

Particular thanks are given to Prof R. L. Dewar (the Project Advisor) for useful and stimulating discussions on plasma theory and numerical methods. My thanks to Dr B. D. Blackwell (the Head of the Supervisory Panel of the project) for his help with many computer related problems. I wish also to acknowledge the support provided me by the staff of the School Computer Unit, in particular Ms J. Dalco.

I would like to thank Dr R. W. Boswell for a number of very useful suggestions he made reading Ref. [77] which constitutes a great deal of Chapter 2. I really benefited from his profound knowledge of experimental physics, in particular, helicon plasma sources.

Among fellow students, I would like to thank Dmitry Rudakov for useful discussions concerning H-1NF and experimental matters and constant help in many other aspects, Darryn Schneider, Alex Degeling and Chris Carter (University of Sydney) for providing me with experimental results obtained in the helicon plasma devices

BASIL, WOMBAT and HARE, respectively.

I have also benefited from the generosity of academic staff of other research organizations:

Special thanks to Prof V. L. Vdovin (Kurchatov Institute, Moscow), my teacher and supervisor in 1981–86, who introduced me to computer simulations of ICRH in tokamaks. We maintained fruitful collaborative links over these years (though it was not always easy), and I had the lucky opportunity to draw from his wealth of experience. A part of this joint work ([137], which is not included in this thesis) has been done during my stay at PRL.

I had the pleasure of collaborating with Dr V. A. Petržílka (IPP, Prague) who stimulated my interest in nonlinear rf phenomena, performed a nonlinear modification of my code FEM and obtained interesting results from it [105, 129, 130].

I would particularly like to thank Dr A. Jaun (Chalmers Institute of Technology, Gothenburg) for his useful explanations and fruitful discussions concerning ($\mathbf{A}$,ϕ)-technique. I would also like to thank Prof K. Appert (CRPP, Lausanne) for making the code ISMENE 5 available for the benchmark.

I am thankful to my wife Cath and son Victor for their understanding, support and many sacrifices they made for the sake of my PhD studies. This work would be hardly possible to accomplish without the constant help I received from my parents, Vladimir and Vera Kamenski; their support, both moral and tangible, was crucial many times. *I devote this thesis to my father; his life was always exemplary for me in every aspect.*

Author's publications

Articles in refereed journals

[1] V. L. Vdovin and I. V. Kamenskij, *3D Theory of ICRH Antenna for Large Scale Tokamaks*, Voprosy Atomnoj Nauki i Tekhniki (Nuclear Science and Technology), Ser. Termoyadernyj Sintez (Thermonuclear Fusion), **19**(2), pp. 3–10 (1985) (in Russian).

[2] G. V. Malyshev, V. M. Kul'kov, A. V. Semenov, S. L. Ermakov, I. V. Kamensky and V. N. Trusov, *Experimental Tether Systems Based on Small Satellites*, Zarubezhnaya Radioelektronika (Foreign Radioelectronics), **12**, pp. 116–127 (1992) (in Russian).

[3] I. V. Kamenski and G. G. Borg, *An Evaluation of Different Antenna Designs for Helicon Wave Excitation in a Cylindrical Plasma Source*, Physics of Plasmas **3**(12), pp. 4396–4409 (1996).

[4] G. G. Borg and I. V. Kamenski, *Collisionless Energy Coupling to Electrons by Helicon Waves in the Near Field of an Antenna*, Physics of Plasmas **4**(3), pp. 529–536 (1997).

[5] G. G. Borg, J. Bright and I. V. Kamenski, *Collisionless Energy Coupling to High Velocity Electrons in the Near Field of an Antenna: Neutral Gas Ionisation by Helicon Waves*, accepted for publication in *Plasma Physics and Controlled Fusion.*

Papers currently submitted to refereed journals

[6] I. V. Kamenski and G. G. Borg, *A 1D Cylindrical Kinetic Wave Code for Helicon Plasma Sources*, submitted to *Computer Physics Communications.*

[7] D. A. Schneider, G. G. Borg and I. V. Kamenski, *Measurements and Code Comparison of Wave Dispersion and Antenna Radiation Resistance for Helicon Waves in a High Density Cylindrical Plasma Source*, submitted to *Physics of Plasmas.*

Refereed conference proceedings

[8] V. K. Kalashnikov, I. V. Kamensky and V. P. Kim, *The Closing of Current of Space Electrodynamic Tether System with Plasma Contactors*, in Proc. 7th USSR Conf. on Plasma Accelerators and Ion Injectors, pp. 288–289, Kharkov, 1989 (in Russian).

[9] I. V. Kamensky, V. P. Kim, V. P. Kukin, V. M. Kul'kov, G. V. Malyshev, A. F. Piskunkov, G. A. Popov, G. G. Shishkin and V. N. Trusov, *Space Electrodynamic Tether System with Plasma Contactors*, 2nd German-Russian Conf. on Electric Propulsion Engines and Their Technological Applications, Moscow, 16–21 July 1993 (Moscow Aviation Institute/Justus-Liebig-Universitat, Giessen).

[10] V. L. Vdovin, V. V. Alikaev, I. V. Kamenskij and G. A. Pestryakova, *ICRF Plasma Heating and Current Drive in ITER*, Zvenigorod-94 – 24th Conf. on Plasma Phys. and Contr. Nucl. Fusion, Russia, Feb. 1994.

[11] G. G. Borg, D. A. Schneider and I. V. Kamenski, *Plasma Formation by Helicon Waves in a Linear Magnetised Plasma: Comparison between Theory and Experiment*, 8th Gaseous Electronics Meeting, Flinders University, Adelaide, South Australia, 29–31 Jan. 1996.

[12] I. V. Kamenski and G. G. Borg, *An Evaluation of Different Antenna Designs for Helicon Wave Excitation in a Cylindrical Plasma Source*, Paper No. 26, 21st Plasma Sci. and Technol. Conf., Australian Inst. for Nuclear Sci. and Engineering, Lucas Heights, Sydney, 17–18 Feb. 1997.

[13] G. G. Borg, D. A. Schneider and I. V. Kamenski, *A Comparison between Experiment and MHD Theory for Antenna–Helicon Wave Coupling in a Cylindrical Plasma Source*, Paper No. 42, 21st Plasma Sci. and Technol. Conf., Australian Inst. for Nuclear Sci. and Engineering, Lucas Heights, Sydney, 17–18 Feb. 1997.

[14] P. Pavlo, V. Petržílka, J. A. Tataronis, G. G. Borg, I. V. Kamenski and L. Krlín, *Nonlinear Density Profile Changes in Helicon Wave Plasmas*, 24th EPS Conf. on Controlled Fusion and Plasma Physics, Berchtesgaden (Germany), 9–13 June 1997.

[15] J. A. Tataronis, V. Petržílka, G. G. Borg and I. V. Kamenski, *Nonlinear Propagation of Helicon Waves in Inhomogeneous Plasma Columns*, 18th Symp. on Plasma Physics and Technology, Prague (Czech Republic), 17–20 June 1997.

[16] J. A. Tataronis, V. Petržílka, G. G. Borg and I. V. Kamenski, *Nonlinear Propagation of Helicon Waves*, 50th Gaseous Electronics Conf. of APS, Madison, WI, USA, 6–9 Oct. 1997.

[17] I. V. Kamenski, R. W. Boswell, G. G. Borg and A. W. Degeling *Computer Simulation of Helicon and Trivelpiece–Gould Wave Propagation in Helicon Plasma Sources*, 10th Gaseous Electronics Meeting, Sydney, NSW, 28–30 Jan. 1998.

[18] G. G. Borg, D. G. Miljak and I. V. Kamenski, *Helicon Wave Antenna Coupling and Heating in Low Pressure Discharges in the H–1 Heliac*, 10th Gaseous Electronics Meeting, Sydney, NSW, 28–30 Jan. 1998.

Meeting/Workshop papers, reports and preprints

[19] V. L. Vdovin and I. V. Kamenskij, *3D Structure of FMS Waves in Large Scale Tokamak Plasma*, in the USSR Contribution to the 9th Session of the Phase IIA Part 2 of the INTOR Workshop, Group B (RF Heating and Current Drive), v.1, pp. 48–89, Vienna, May 1984. Rep. EURFUBRU/XII-1/84/EDV23.

[20]. V. L. Vdovin and I. V. Kamenskij, *Coupling Calculations for ICR Waves in Plane Geometry*, in the USSR Contribution to the 11th Session of the Phase IIA Part 2 of the INTOR Workshop, Group B (RF Heating and Current Drive), pp. 3–9, Vienna, March 1985.

[21] V. L. Vdovin and I. V. Kamenskij, *Modelling of ICR Heating in INTOR*, in the USSR Contribution to the 13th Session of the Phase IIA Part 2 of the INTOR Workshop, Group B, Chapter 4, pp. 73–127, Vienna, March 1986. Rep. EURFUBRU/XII-52/86/EDV13.

[22] V. L. Vdovin, V. V. Alikaev, I. V. Kamenskij and G. A. Pestryakova, *ICRF Plasma Heating and Current Drive in ITER*, Russian Contribution on ICRF Heating/Current Drive, ITER Meeting on RF Heating, Garching (Germany), Nov. 1993. IDOMS No. G CZ IP 2 94-05-24 F.

[23] I. V. Kamenskij, Yu. V. Petrov and V. L. Vdovin, *Recent Russian ICRF Theoretical and Modelling Studies*, ITER Expert Group Meeting, Moscow, Oct. 1995. IDOMS No. S 19 IP 1 97-01-28 F 1.

[24] G. G. Borg, D. A. Schneider and I. V. Kamenski, *A Study of Antenna Coupling and Wave Propagation in Helicon Wave Plasma Formation Experiments*, Bull. Am. Phys. Soc. **40**(11), 1679 (1995).

[25] V. L. Vdovin and I. V. Kamenskij, *3D Electromagnetic Theory of ITER ICRF Multi Port Multi Loop Antenna*, ITER Progress Report, RNRC "Kurchatov Institute", ITER Physics Design Group, Moscow, May 1996. IDOMS No. S 19 IP 2 97-01-28 F 1.

[26] G. G. Borg and I. V. Kamenski, *Helicon Wave Propagation and Plasma Interaction*, Bull. Am. Phys. Soc. **41**, 1611 (1996).

[27] I. V. Kamenski and G. G. Borg, *A 1D Cylindrical Kinetic Wave Code for Helicon Plasma Sources*, Report ANU-PRL-PP-1/97, ANU, Canberra 1997.

[28] V. L. Vdovin and I. V. Kamenskij, *3D Electromagnetic Theory of ITER ICRF Multi Port Multi Loop Antenna*, Research report NIFS-479, NIFS, Nagoya (Japan), Jan. 1997.

[29] D. A. Schneider, G. G. Borg and I. V. Kamenski, *Measurements and Code Comparison of Wave Dispersion and Antenna Radiation Resistance for Helicon Waves in a High Density Cylindrical Plasma Source*, Report ANU-PRL-PP-01/98, ANU, Canberra 1998.

Chapter 1

Introduction

1.1 Helicon Plasma Sources: State of the Research

1.1.1 Helicon Plasma Sources

Plasma waves play an important role in plasma technology and space physics. Also, they have long been under study for the heating of fusion plasma. Recently, helicon wave driven plasma sources have become very important contenders as sources for a wide range of industrial applications and the low cost per unit means that they are available for investigation by many experimental research groups.

The first, accidental, observations of whistlers (helicon waves in ionospheric plasma) were reported in 1886; they manifested themselves as whistling notes heard in telephone. Since then and for a long time, the interest to this phenomenon was mainly linked to the interference it produced to long distance communications. In 1953 L. Storey [124] presented the first detailed theory for ionospheric whistlers and explained their origin (by lightning flashes) and propagation guided by geomagnetic field lines. In particular, those waves can be trapped in long ionospheric density formations ("ducts") and make multiple passes from one hemisphere to another.

Helicon waves are whistler analogues in bounded laboratory plasmas (solid state or gaseous); they typically propagate in an axially magnetized plasma column. They have been named so by P. Aigrain [2] who also suggested their use for measuring Hall coefficients in metals.

Nowadays, the formation of plasma using radiofrequency power continues to be a fruitful topic of research, and one of the principle methods of producing plasma for technological applications. Experimental study aimed at plasma production by helicon waves was started by R. Boswell [20, 21], and an active use of helicon wave produced plasmas for etching and deposition of materials used in microelectronics and optics was initialized by the work of Boswell and Henry [25] in 1985. With the peak plasma densities $\approx 4 \times 10^{18}$ m^{-3} produced with only 600 W rf power at 8 MHz [20], it was possible to achieve high deposition and etching rates (about 10 times

larger than in commercial rf diode reactors [26]).

Conventionally, helicon sources are subdivided into 2 classes. Most of them operate with argon plasmas at temperatures in the range $T_e \approx 2.5$ — 6 eV. First class are the low magnetic field ($B_0 \leq 0.02$ T) and low density ($n_e < 10^{19}$ m^{-3}) devices which typically operate at frequencies between the lower hybrid and electron cyclotron frequency and are mainly used in plasma processing. It has been recently recognized that slow, Trivelpiece-Gould modes can play an important role in such plasmas [15, 113, 114]. Another class are high density, high magnetic field sources ($n_e = 10^{19} - 10^{20}$ m^{-3}, $B_0 \leq 0.2$ T) which are mainly used in fundamental research and some other applications, such as the electrodeless gas laser [143, 144]. They typically operate at frequencies near the lower hybrid resonance (LHR).

Helicon wave produced plasmas can also be used for plasma injection into magnetic confinement devices for fusion studies [97] and in plasma particle accelerators [34].

In material processing devices [25, 92, 94, 95, 106, 107, 117, 119], helicon sources provide high density plasma which then diffuses into a processing chamber. This allows the separation of processing region from the plasma source and high plasma uniformity over the processing region. For deposition, helicon sources enable the evaporated material to form a considerable amount of plasma and, in principle, allow plasmas to be completely composed of evaporated material [52]. This provide an opportunity to precisely control the gas chemistry and obtain high chemical selectivity. Low operational pressures in the processing chamber allow anisotropic etching. Magnetic fields required for helicon plasma sources (20 — 200 G) are considerably lower than for electron cyclotron resonance (ECR) discharges (about 1 kG); in addition, they use conventional rf transmitters to drive an antenna. In capacitively coupled plasma discharges (CCPs) the energy penetration is limited to the plasma skin depth; this is one of the main reasons why they do not satisfy all requirements for ultra-large scale integration technology [93].

Nowadays, helicon sources have become commercially available for both etching and deposition of a range of materials. Helicon waves can efficiently produce plasma in magnetic fields as low as few tens of Gauss and in the frequency range 1 — 30 MHz where kW-range rf sources are cheap and readily available. Helicon sources can be run at low pressures in most gases because helicon wave dispersion (in its simplest form) is not dependent on the ion mass. Unlike other rf plasma sources, the coupling of the exciter to the plasma, to a good approximation, does not depend on the plasma collisionality but instead, on the antenna radiation resistance (R_{rad}). This considerably simplifies the source design process where one of the aims is to maximize the R_{rad}. Radiation resistances of a few Ohms are easily attainable. Due to high R_{rad}, helicon sources are easy to operate, simply by matching the input impedance.

During their 30 years history, helicon wave devices were designed mostly empirically. Thus the basics of antenna coupling to helicon waves is yet to be performed and checked experimentally. In addition, the physics of the helicon wave interaction with plasma still allows interesting effects to occur that could be employed to optimize the properties of helicon plasma sources. For example, recently [48] a wave phase velocity dependent enhancement of plasma ionisation rate has been observed in a helicon source, thus suggesting another possibility of controlling the discharge physics (and chemistry) by the wave.

1.1.2 Plasma Production Mechanism

Critical issues for any wave-supported source are how waves are excited in it, what are the wave types and where and how they deposit their energy. The importance of helicon wave produced plasmas in material processing has made understanding the physical mechanisms involved in this method of plasma production important to the optimization of existing source designs and the design of sources with new applications. In particular, the mechanism of plasma formation by helicon waves has been the object of much research due to the high density plasmas produced by helicon waves at a low power cost [33, 48, 53, 95, 97, 119].

In early experimental studies of helicon waves excited at rf frequencies performed in 1962 – 1965 by Hooke et al. [67], Kovan et al. [89], Nazarov et al. [103] Jephcott and Malein [76], Lehane and Thonemann [91] and Dolgopolov et al. [51], it was noted that the gas ionization produced by these waves was anomalously efficient, and the wave damping rates were anomalously high.

This still remains a puzzle and attracts considerable attention of many research groups. Evidence has been provided for wave–particle interactions [48, 53], nonlinear effects [125] and eigenmode resonance discharges [82, 113]. In order to elucidate the physical mechanisms responsible for plasma production, work has tended to concentrate on how the wave energy is dissipated in the plasma. This is most important when the plasma is formed at low fields ($\lesssim 0.01$ T) and filling pressures and the plasma density is low ($\lesssim 10^{19}$ m^{-3}) [53, 106], where it has been shown that traditional kinetic dissipation mechanisms cannot significantly damp the wave. At low densities, the collision frequencies are also too low so that collisions do not absorb all the wave energy. Electron cyclotron damping, which can be efficient even for frequencies $\omega \ll \omega_{ce}$, was proposed by Harvey and Lashmore-Davies [65] as a possible dissipation mechanism. However this requires plasma densities which are much higher than attained in helicon sources.

It is now believed that the helicon discharge physics is determined by ionization brought about by both the background Maxwellian electrons and the perturbation to the electron distribution function due to electrons accelerated by the wave. Various

theories have been proposed to describe the process by which the wave couples energy to electrons. Electron Landau damping combined with particle trapping was suggested by Chen [35, 38] to explain the electron acceleration. The experimental evidence now exists [38, 86, 97, 98] of the "bump-on-tail" feature on the electron energy distribution function which occurs at about the helicon wave phase velocity corresponding to 3 — 4 times the electron thermal speed. This effect is not expected because these values are too large for Landau damping to be effective. Nevertheless, energies acquired by the "bump" electrons are optimal for the primary gas ionization, and these energetic particles are reputed to cause the ionization enhancement.

To date, no satisfactory explanation of a bump-on-tail feature has been proposed, suggesting that the wave–plasma energy transfer is probably concentrated in the antenna near field. If the collision mean-free-path is longer than a wavelength, the properties of the wave in the antenna near field may play an important role in the plasma maintenance process [14, 48, 53]. Recently, Borg et al. [17, 18] have suggested that the dominant kinetic process under these conditions is a spatially transient overshoot in the rate of work done by the wave in the antenna near field. The overshoot arises due to the Landau-type interaction as a result of the transient response of the electron distribution function to a rapid variation or reversal in the direction of the wave phase velocity near the antenna, provided that the phase velocity is few times the electron thermal speed. This effect is also reproduced [17] by the UFEM code reported in this thesis.

1.1.3 Antenna Radiation Resistance

Despite numerous advantages, until recently it has not been common practice to employ plasma waves to drive rf plasma sources. Most rf plasma sources are nowadays either capacitively or inductively driven. The application of plasma waves to plasma formation, as opposed to plasma formation in capacitively coupled plasmas (CCPs) or inductively coupled plasmas (ICPs), benefits from the fact that the antenna loading is dominated by the power coupled to the propagating wave and not stray-tuning circuit losses. For helicon discharges, the antenna radiation resistance (R_{rad}) does not depend much on the wave dissipation mechanisms but rather on the dispersion properties of the wave and the antenna structure. It allows antennas to be designed practically disregarding the question of what dissipative mechanisms are operational in plasma, provided that the wave is sufficiently damped. Nonetheless, the R_{rad} is a measure of the power deposited in the plasma. It can be measured easily without perturbing the plasma, and for devices of cylindrical geometry, theoretical calculations of the R_{rad} with a 1D code should be reliable. They should at least determine whether the wave is the main vehicle by which the antenna transmits its power to the plasma as opposed to parasitic mechanisms.

The first step in analyzing the discharge physics is to determine the antenna radiated power, especially for high density plasmas. Many different antenna types can be employed to excite the wave. Their performance will depend on the modes excited and the magnitude of R_{rad} compared to the equivalent loss resistance due to Ohmic losses in the matching network. During plasma formation, the radiated power changes, and the final equilibrium is determined primarily by the fraction of rf transmitter power which is coupled to the plasma. The radiated power also depends on the plasma properties, such as the density and the density profile. An important fact that will be demonstrated in § 2.3.1 is that in linear helicon sources with an open magnetic field, the total R_{rad} is almost independent of the wave damping, provided that the waves are not reflected back toward the antenna and that the damping is not too large.

For plasmas with densities $\sim$ 10^{19} m^{-3} produced by high power at a high field ($\gtrsim$ 0.1 T), at either full ionization or high filling pressures [144], the wave damping is determined mainly by collisions (electron–ion and electron–neutral). The collision mean-free-path is so short (much shorter than a wavelength) that kinetic damping mechanisms are not very important, the power deposition is local, and the wave dissipation is rapidly thermalized. The ionization is presumably fixed at the Maxwellian rate and the rf deposited power directly enters into the plasma energy balance. In this case, the R_{rad} is the key parameter determining the energy and particle balance.

In the low density and low field sources, wave-particle interactions have been suggested as being important in coupling energy into electrons (§ 1.1.2). Under these conditions, the effects of finite electron mass are considered to be important as well. It will be shown in § 5.1 however that for the high density and field sources (even of small radius), the dominantly excited m=+1 first radial mode is not severely affected by finite electron mass and the MHD model of Chapter 2 is quite suitable at least for the computations of the R_{rad}.

1.1.4 Theoretical Treatment and Comparison with Experiment

First detailed theoretical treatment of helicon waves was performed by Klozenberg et al. [85] and Ferrari et al. [56] who calculated dispersion and radial wavefield profiles for m=0 and $m = \pm 1$ azimuthal modes in a uniform plasma cylinder with a vacuum boundary [85] and a conducting wall [56]. These were, probably, the first works utilizing not only analytical but also numerical methods. However, they did not calculate the radiation resistance which is so important in explaining phenomena observed in these plasmas. Lehane and Thonemann [91] compared the theory of Klozenberg et al. [85] to experimental dispersion measurements in a preformed

plasma. They made no attempt at mode identification other than by comparison to the theoretical dispersion calculations, which gave agreement with the help of a correction factor. It is interesting that the preformed plasma in this experiment was probably produced by helicon wave excitation, but not studied at all.

In 1966 Blevin and Christiansen [12] made an attempt to develop a theory for nonuniform plasmas, which however suffered from a number of simplifying assumptions and did not yield good agreement with experiment.

First eigenmode calculations taking into account finite electron mass were performed by Davies and Christiansen [47] and by Boswell [23] for typical conditions of a helicon plasma source with both conducting and non-conducting boundaries. The eigenmode structure was found to be produced by both helicon and Trivelpiece-Gould (TG) waves. The TG wave branch [23, 113] presently attracts considerable attention due to its potentially important role in the energy coupling. Also, the effects on the plasma response in the vicinity of the LHR have been observed experimentally [144], and the possibility for mode conversion to the LH wave at and above the LH frequency in any case exists. All these questions are unresolved and warrant further theoretical and experimental investigation.

1.2 Motivation

The present work has been motivated by the prominent lack of computer models in this field which would be adequate enough to be directly compared with experiment. The use of plasma waves in industrial type plasma sources is still in its infancy and most workers do not have the computational antenna and wave–particle modelling apparatus that has traditionally been available to workers in rf fusion plasma heating. Whilst the linear plasma wave theory is generally well understood and has enjoyed wide application to rf heating and current drive in fusion plasma science, its application in cold industrial plasmas produced by helicon waves is relatively new. Modelling of helicon sources is also complicated by the wide parameter regime over which helicon waves are used to produce plasmas.

Consequently, some rather salient facts have evaded careful experimental – theoretical verification. These include that antennas with an $m = \pm 1$ current structure have an excited spectrum that is often dominated by one mode, the m=+1 first radial mode. This mode propagates without a cutoff, under most conditions there tends to be an absence of negative azimuthal modes ($m < 0$) [19, 40, 112] and the absence of clearly observable non-linear effects. Indeed, there is even no consensus under what conditions the $m < 0$ modes can be observed. Shoji et al. [119] have reported the observation of an m=–1 mode excited using a helical antenna, at variance to most other results for similar conditions. Recent works by Chen et al. [40, 95] with a helical antenna shows a lack of excitation of an m=–1 mode, but

with only radial measurements for mode identification they were unable to estimate the extent of the dominance of the m=+1 mode or conclusively identify the modes causing beat patterns in wave field amplitude measurements. They also lack radiation resistance results and a model for the antenna-plasma coupling for comparison and explanation of the lack of $m < 0$ modes.

Finally, the important overriding unanswered question is whether the theoretical R_{rad} agrees with experiment and how much of the antenna power is parasitic (not coupled to the helicon wave). The paramount importance of the antenna as a wave launcher has not yet received much attention in the study of rf produced plasmas. Many calculations of R_{rad} for different antennas have been performed for ion cyclotron heating in fusion devices. To the best of the author's knowledge however, very little has been done to date on systematic study of R_{rad} for realistic antenna geometries in helicon sources, even though it is critical for the understanding of plasma and energy balance. Moreover, much experimental work is being performed using the same antennas modelled in this thesis.

In Chapters 2 and 3 we confront the above issues for the case of a high density, high magnetic field cylindrical source in which the antenna structure is mainly $|m|$=1. A similar study can now be performed with the use of the kinetic UFEM code (Chapter 4) for the larger size, lower density ($n_e < 10^{19}$ m^{-3}) and field ($B_0 <$ 0.02 T) sources for which the antenna coupling and wave dispersion properties could be quite different.

The existing numerical models, which treat the antenna coupling and wave excitation in helicon sources, are often oversimplified. Several models [85, 113, 114] were developed for flat plasma density profiles only. Particularly, such codes fail to properly describe the asymmetry in antenna–plasma coupling between positive and negative azimuthal modes, a strong effect which is well established experimentally [19, 95, 112], reproduced by some other codes for conditions ranging from large scale tokamaks [134, 135] to helicon sources [43, 77] and being attributed to the effect of plasma density gradient [43, 77]. Several researches and research groups [55, 72, 102] use the ANTENA code [99, 100] which suffers from the same drawback due to the stratified plasma model it employs. More sophisticated numerical schemes used in Refs. [43] and [57], yet properly account for the density gradient effects, employ a straightforward *finite difference* discretization of Maxwell's equations which tends to diverge at resonances. As a result, the model of Ref. [57] was used only for flat density profiles in the lower hybrid frequency range, and the model of Ref. [43] only for frequencies well above the LHR. The numerical scheme developed in Ref. [39] (similar in its "physics" to the MHD model of Chapter 2) uses the finite difference "shooting" approach which is also unable to treat resonances. In addition, it erroneously imposes the condition $B_r = 0$ at the plasma–*insulating* wall boundary (neglecting the rf charge on it) which does not withstand any serious criticism and

clearly contradicts the experimental results obtained by the same authors [95].

Another 1D cylindrical kinetic code ISMENE 5 [7, 133] is much more reliable and could, in principle, be adapted to model helicon sources. However, it is designed primarily for the ion cyclotron resonance heating (ICRH) in tokamaks and its "physics" is overcomplicated by the 2nd order finite Larmor radius (FLR) terms which are known to be negligible in helicon sources. This code works with a limited number of discrete toroidal eigenmodes, and it is not easy to put a realistic antenna into it. And finally, it is a very large code which is not easy to modify without very close collaboration with its author (Prof K. Appert, CRPP, Lausanne). In addition, before the benchmark with the code UFEM (§ 4.6) it was not clear whether this code guarantees the absence of numerical pollution at the LHR due to the nature of the discretization scheme employed in it.

This motivated the author to develop two numerical models, the FEM code (MHD model) and UFEM code (kinetic model) reported in this thesis. Both codes use the *finite element method.* This method is particularly suitable for the task since it allows treatment of plasma wave resonances (such as the LHR) and the mode conversion where conventional methods (such as the finite difference methods, shooting or WKB) often fail, provided that the finite element discretization is properly constructed so as to avoid numerical pollution.[1] In loose words, finite element schemes do not diverge at resonances since the solution is always "stuck" to boundary conditions. This method also allows one, in many cases, to change the physics (for example, the plasma parameters) easily without changing the algorithm.

The code UFEM (Chapter 4), in particular, has been designed with helicon plasma sources in mind. Most importantly, it can safely treat resonances and mode conversion between the fast and slow wave modes and retains the antenna geometrical details (as well as some details of the chamber, Appendix A) through the full antenna Fourier-spectrum. It is now becoming clear that the important wave–plasma interaction physics of a small helicon source occurs within the antenna near field. In fusion plasma applications, the machines are often so large that antenna near field effects can be either ignored or if required, treated separately. The main interest usually lies in the physics of resonance layer slow wave interactions, for example near the Alfvén, ion cyclotron or lower hybrid resonance layers. This is not the case in helicon sources where the plasma is small compared to the wavelength.

One simplifying assumption employed in the UFEM code is that the plasma temperature in industrial sources is low so that finite Larmor radius (FLR) effects can be ignored [18]. This affords a considerable reduction in complexity and controversy as the FLR induced equilibrium gradient terms that lead to higher order derivatives in the wave equations [30, 133] do not arise. The code can also be employed to study plasma waves in current-free cylindrical plasmas in other frequency ranges.

[1] This point is considered in Chapter 4.

In summary, the main aim of this thesis is to develop a full antenna spectrum code that employs the essential physics of low temperature plasmas and to investigate the physics of antenna–wave coupling and wave propagation.

1.3 The Thesis Structure

This thesis is structured as follows:

In Chapter 2 we perform a computational study of antenna radiation resistance and wave dispersion in high density, high magnetic field helicon plasma sources using a simple magnetohydrodynamic numerical model which neglects finite electron mass. We compare the radiation resistances of four commonly used antennas and consider the effects on the R_{rad} of frequency, plasma density, density profile form and system dimensions. We also suggest explanations for poor excitation of negative azimuthal modes in such devices and axial beat patterns of the wavefield which are often observed experimentally. The implications to the present understanding of high density helicon sources and their design are also discussed.

In Chapter 3 we compare results from the BASIL experiment with the MHD numerical model for a double saddle coil, a helical antenna and a pair of phased double saddle coils. Good agreement between the model and experimental measurements of the wave dispersion and the antenna radiation resistance is demonstrated.

In Chapter 4 we outline the theoretical basis for a new 1D cylindrical kinetic wave code UFEM (which is also described in Appendix C) designed primarily for helicon plasma sources. We introduce the pollution-free finite element numerical scheme for the solution of Maxwell's equations in terms of electromagnetic potentials which is suitable for the computations in the presence of wave resonances. We also give a short discussion of different wavetypes and resonances described by the model, discuss the numerical convergence and pollution, and present the code benchmarking results.

In Chapter 5 we consider similarities and differences between the MHD and kinetic models with respect to the high density sources. Also, we present some modelling results for the low density, low magnetic field helicon plasma device WOMBAT. In Section 5.3 we speculate about connection between the excitation of global eigenmodes in H-1NF heliac and the experimentally observed L – H transitions, a question which nowadays attracts considerable attention.

In Chapter 6 we summarize the results and discuss further development of the numerical model to account for realistic 3D geometry.

Chapter 2

MHD Plasma Model

2.1 MHD Numerical Model of the Antenna–Plasma System

In this Chapter we employ a finite frequency magnetohydrodynamic (MHD) model to analyze helicon wave coupling by four commonly used antennas in cylindrical geometry. We confine this study to the [ion cyclotron — helicon] frequency range so that a comparison can be made between low mass gases such as hydrogen and the high mass gases, typically argon.

We employ the 2×2 dielectric tensor of a cold collisional plasma, implying $\varepsilon_{33} = \infty$:

$$\underline{\varepsilon} = \begin{pmatrix} \varepsilon_1 & i\varepsilon_2 \\ -i\varepsilon_2 & \varepsilon_1 \end{pmatrix} , \tag{2.1}$$

where

$$\begin{aligned} \varepsilon_1 &= 1 - \sum_i \frac{\omega_{pi}^2(\omega + i\nu_i)}{\omega[(\omega + i\nu_i)^2 - \omega_{ci}^2]} - \frac{\omega_{pe}^2(\omega + i\nu_e)}{\omega[(\omega + i\nu_e)^2 - \omega_{ce}^2]} , \\ \varepsilon_2 &= -\sum_i \frac{\omega_{pi}^2\omega_{ci}}{\omega[(\omega + i\nu_i)^2 - \omega_{ci}^2]} + \frac{\omega_{pe}^2|\omega_{ce}|}{\omega[(\omega + i\nu_e)^2 - \omega_{ce}^2]} , \end{aligned} \tag{2.2}$$

and where ω_{pi}, ω_{pe}, ω_{ci}, ω_{ce}, ν_i, ν_e are plasma, cyclotron and collision frequencies for ions and electrons, respectively. The summation in Eqs. (2.2) is over all ion species (different ion species may occur when higher order ionization states occur in the same plasma).

Maxwell's equations, using tensor (2.1), are given by

$$\nabla \times \mathbf{B} = -\frac{i\omega}{c}\underline{\varepsilon}\mathbf{E} + \frac{4\pi}{c}\mathbf{j}_{ant} , \qquad \nabla \times \mathbf{E} = \frac{i\omega}{c}\mathbf{B} ,$$

where $\mathbf{j}_{ant}$ is the antenna current density.

Taking Fourier-components of the wave field and antenna currents as

$$\sim \exp\{i(m\theta + k_z z) - i\omega t\} ,$$

we obtain the following equation for E_θ in cylindrical coordinates $\{r, \theta, z\}$:

$$-[\alpha(rE_\theta)']' + (\beta + \gamma')(rE_\theta) = -f - g' \ , \tag{2.3}$$

where the prime denotes the radial derivative,

$$\alpha = \frac{A}{k_1^2 r} \ , \qquad \beta = \frac{k_\perp^2}{r} \ , \qquad \gamma = \frac{m\bar{\varepsilon}_2}{k_1^2 r^2} \ ,$$

$$f = iJ_\theta + \frac{\bar{\varepsilon}_2}{k_1^2} J_r \ , \qquad g = \frac{mJ_r}{k_1^2 r} \ , \tag{2.4}$$

and

$$A = \bar{\varepsilon}_1 - k_z^2 \ , \qquad k_1^2 = \frac{m^2}{r^2} - A \ , \qquad k_\perp^2 = A + \frac{\bar{\varepsilon}_2^2}{k_1^2} \ ,$$

$$\bar{\varepsilon}_{1,2} = k_0^2 \varepsilon_{1,2} \ , \qquad k_0 = \frac{\omega}{c} \ , \qquad J_{r,\theta} = \frac{4\pi k_0}{c} j_{r,\theta} \ , \tag{2.5}$$

j_r, j_θ are the Fourier-components of the antenna currents (Appendix B). The axial antenna current, j_z, drops out of the equations, since we disregard the singular equation $[\nabla \times \mathbf{B}]_z = -ik_0 \varepsilon_{33} E_z + (4\pi/c) j_z$.

In our model we treat the inner surface of the magnetic coils at $r = b$ as a perfectly conducting cylinder, on which $E_\theta = 0$. One can easily demonstrate that the regular (finite) solution of Eq. (2.3) in the absence of antenna currents at $r \to 0$ behaves as $E_\theta \sim r$ for m=0, and as $E_\theta \sim r^{|m|-1}$ for $m \neq 0$.

For m=0 we rewrite Eq. (2.3) in the following form:

$$-(\tilde{\alpha} E_\theta')' + \tilde{\beta} E_\theta = -\tilde{f} \ , \tag{2.6}$$

with

$$\tilde{\alpha} = -r \ , \qquad \tilde{\beta} = k_\perp^2 r - \frac{1}{r} \ , \qquad \tilde{f} = r\left(iJ_\theta - \frac{\bar{\varepsilon}_2}{A} J_r\right) \ ,$$

$$(\quad \tilde{\gamma} = \tilde{g} = 0 \quad) \ . \tag{2.7}$$

Thus, we reduce the problem to the equation

$$-(\alpha y')' + (\beta + \gamma')y = -f - g' \ , \tag{2.8}$$

with the boundary conditions

$$y(0) = y(b) = 0 \ , \tag{2.9}$$

where for $m \neq 0$, $y = rE_\theta$ and the coefficients are determined by Eqs. (2.4), while for m=0, $y = E_\theta$ and the coefficients are determined by Eqs. (2.7). Note that both for m=0 and $m \neq 0$, $\alpha \sim r$ and $\beta \sim 1/r$ for $r \to 0$.

Equation (2.8) is solved by the finite element method in the whole plasma–vacuum domain. Other field components are computed from E_θ. From the wave electric fields, we compute the antenna impedance Z by the "induced emf" method,

$$Z = -\frac{1}{I_0^2} \int_V \mathbf{E}(\mathbf{r}) \cdot \mathbf{j}_{ant}^*(\mathbf{r}) dV \ , \tag{2.10}$$

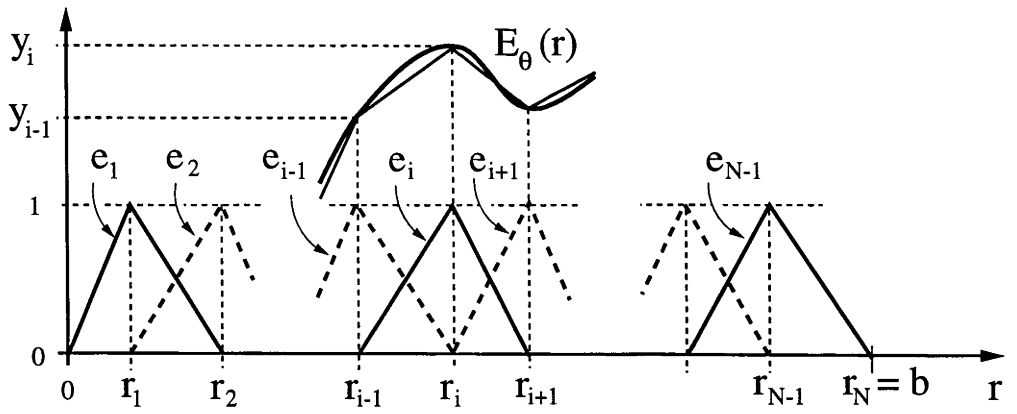

Figure 2.1: The wave field approximation by linear finite elements.

where I_0 is the peak amplitude of the antenna current, and integration is performed over the whole plasma–vacuum volume. The total antenna impedance Z can be expressed as a sum/integral over the m- and k_z- spectrum,

$$Z = \sum_m \int Z(m, k_z) dk_z \ ,$$

and R_{rad} is the real part of the impedance, $R_{rad} = Re(Z)$.

To solve Eq. (2.8) by the finite element method, we follow a standard procedure described, for example, in [62, 138]. We multiply Eq. (2.8) by a test function and integrate it by parts from $r = 0$ to $r = b$. Then, on the radial mesh $\{r_i\}$, ($r_0 = 0$, $r_N = b$), we introduce a set of triangle basis functions having finite support (Fig. 2.1)

$$e_i(r) = \begin{cases} (r - r_{i-1})/(r_i - r_{i-1}) & \text{if} \quad r_{i-1} < r \leq r_i, \\ (r_{i+1} - r)/(r_{i+1} - r_i) & \text{if} \quad r_i < r < r_{i+1}, \\ 0 & \text{elsewhere} \ . \end{cases} \tag{2.11}$$

We expand $y(r)$ in this basis set:

$$y(r) = \sum_{i=1}^{N-1} y_i e_i(r) \ . \tag{2.12}$$

Inserting (2.12) into the equations and taking each e_i as a test function, we finally obtain a linear system for the unknown weight coefficients y_i :

$$M_{ij} y_j = G_{i-1} - G_i - F_i^- - F_i^+$$

with M_{ij} being a 3-diagonal symmetric matrix:

$$M_{ij} = 0, \quad \text{if} \ \ |i - j| > 1 \ ,$$

$$M_{ii} = A_{i-1} + B_i^- - C_i^- + A_i + B_i^+ + C_i^+ \ ,$$

$$M_{i,i+1} = M_{i+1,i} = -A_i + B_i + C_i \ ,$$

$$A_i = \int_{r_i}^{r_{i+1}} \alpha (e_i')^2 dr \ ,$$

$$B_i = \int_{r_i}^{r_{i+1}} \beta e_i e_{i+1} dr \ , \quad B_i^- = \int_{r_{i-1}}^{r_i} \beta e_i^2 dr \ , \quad B_i^+ = \int_{r_i}^{r_{i+1}} \beta e_i^2 dr \ ,$$

$$C_i = -\int_{r_i}^{r_{i+1}} \gamma (e_i e_{i+1})' dr, \quad C_i^- = \int_{r_{i-1}}^{r_i} \gamma (e_i^2)' dr, \quad C_i^+ = -\int_{r_i}^{r_{i+1}} \gamma (e_i^2)' dr,$$

$$G_i = -\int_{r_i}^{r_{i+1}} g e_i' dr \ , \quad F_i^- = \int_{r_{i-1}}^{r_i} f e_i dr \ , \quad F_i^+ = \int_{r_i}^{r_{i+1}} f e_i dr \ . \qquad (2.13)$$

Integration in (2.13) is performed numerically by the 4-point Lobatto formula [1]. The boundary conditions (2.9) are explicitly taken into account by the choice of the set of basis functions $\{e_i\}$, $i = 1, \ldots, N-1$.

The singularity $k_1^2 = 0$ in Eq. (2.3) is practically never met in helicon devices, where $k_0 \ll |m|/r$ for $m \neq 0$. For $m = 0$ we solve Eq. (2.6) which has no such a singularity. The only possible singularity in our equations is the Alfvén (A-) resonance, $A \to 0$. Despite the fact that our model is capable of describing the A-resonance (for $|k_z| \leq k_0$), the antenna typically excites a k_z-spectrum with predominantly $|k_z| \gg k_0$. The A-resonance does not play an important role here since it comprises a small fraction of the radiated power.

A numerical code "FEM" has been written based on the above scheme. This code has been benchmarked by a uniform plasma filled waveguide code based on Bessel function solutions to the above wave equations [142].

Similar approaches have been previously developed [57, 138]. An essential feature of our model is that the antenna currents, having a finite radial extent, appear as a source term in the right hand side of Eq. (2.8). Such a scheme has several advantages. A single algorithm is used for the vacuum and plasma, which does not involve any special functions and analytic solutions in the regions with radial currents. We are not concerned with boundary conditions at the antenna and at the plasma–vacuum interface. We can consider an antenna of almost arbitrary configuration, placed in the plasma and/or in a vacuum.

2.2 Description of the Antenna and the Source Parameters

We perform a comparative study of four antennas using the following standard source parameters. The source is modelled by a cylindrical plasma column (of infinite length) of radius $a = 2.5$ cm surrounded by a vacuum and bounded by a conducting wall at $b = 5.3$ cm. The plasma is formed in 100% singly ionized

argon, having a parabolic density profile $n_e(r) = n_{e0}[1 - (r/a)^2]$ of central density $n_{e0} = 10^{19}$ m^{-3} (the average density is $\langle n_e \rangle = 5 \times 10^{18}$ m^{-3}). The constant axial magnetic field is taken to be $B_0 = 0.1$ T, and the antenna excitation frequency $f = 13.56$ MHz. The electron temperature is taken to be $T_e = 5$ eV of uniform profile. This temperature allows us to calculate collision rates in an otherwise cold plasma (§ 4.1).

We will not always restrict our study to the standard case. Some conclusions are worth checking for other experimental conditions, in particular, other excitation frequencies, densities, density profiles and device sizes. The standard conditions approximate numerous glass tube helicon sources of geometry similar to the electrode driven positive column. These devices are normally much longer than they are wide and the plasmas produced for magnetic fields $\gtrsim 0.1$ T are cool and dense. The MHD theory presented in this Chapter is a simple yet highly accurate model for the description of these plasmas.

The antennas used in this study are shown schematically in Fig. B.1 (Appendix B). For all antennas, the radius of the inner antenna edge is $s = 3.1$ cm, and the radial thickness of antenna wire is $d = 3$ mm.

In Fig. B.1(a) we show a double half-turn antenna. This antenna is completed by two radial elements to an outer loop, with the radius of outer edge $s_1 = 5$ cm, located near a conducting wall. Such an antenna has no z-directed elements and is the simplest for studying non-axisymmetric propagation without imposing constraints on the k_z-spectrum. This has the *a priori* advantage that experiments can be performed on plasma formation without a density restriction imposed by k_z [48].

In Fig. B.1(b) we show the m=0 single loop antenna, which also places no restriction on k_z.

In Fig. B.1(c) is a double saddle coil, which becomes the Nagoya type III antenna [95] when the azimuthal elements extend to $2\theta_a = \pi$. We do not expect a qualitative difference between these two antenna types. This antenna is a non-axisymmetric structure which launches odd m-modes.

In Fig. B.1(d) is a $|m|$=1, $\lambda/2$ positive helicity helical antenna. Here $\lambda/2$ refers to the fact that the antenna length L is 1/2 the length of a single turn helical winding, which we designate by λ. Helical antennas have the interesting property that they are directional. The helical antenna, having positive helicity, mainly launches positive m modes in the direction of positive k_z (parallel to B_0) and negative m modes in the direction of negative k_z (antiparallel to B_0). This has the potential advantage that half the power can be saved by launching the wave in one direction along the magnetic field.

The antenna lengths (L) for the double saddle coil and helical antennas are chosen so that the antenna current Fourier transforms (Appendix B (C) and (D))

have maxima for m=+1 and $k_z \approx 26$ m^{-1}, which correspond to the first radial mode of m=+1 for standard conditions. This leads to the values, $L = 12$ cm for a double saddle coil and $L = 20$ cm, and hence, $\lambda = 40$ cm for the helical antenna.

A comparison of the uniform plasma dispersion relation for various perpendicular wavenumbers and our standard conditions shows that our model is useful for a description of the fast wave down to (and below) the ion cyclotron frequency. The omission of electron mass limits the range of validity of perpendicular wave numbers to $\lesssim 300$ m^{-1} for the standard case. This means that the model does not describe radial modes higher than the second radial mode of m=+1 near their cutoffs, nor does it include the Trivelpiece–Gould modes [23, 113, 131]. It turns out that the first radial mode of m=+1 is usually by far the dominant mode and, even in small devices, its perpendicular wavelength falls well below this limit. Shamrai et al. [113] have shown that the helicon branch dominates over the Trivelpiece–Gould mode in the antenna coupling at high fields for which $\nu_e \omega_{ce} k_z a/\omega^2 \gg 1$. For standard conditions, the collision frequency $\nu_e \approx 3 \times 10^7$ s^{-1} and this quantity is greater than 20 for $k_z \geq 10$ m^{-1}. The omission of electron mass also eliminates the lower hybrid wave. To the best of the author's knowledge no experimental evidence for direct excitation of the lower hybrid wave has been reported in the literature for the kinds of antennas modelled in this Chapter. Effects have however been observed on the plasma response in the vicinity of the lower hybrid frequency [143]. The possibility in any case exists for mode transformation of the helicon mode to the lower hybrid wave above the lower hybrid frequency, but this will not directly affect the validity and interpretation of the calculated $R_{\rm rad}$ [9]. A study of the lower hybrid wave is beyond the scope of this Chapter. The lower hybrid waves and the Trivelpiece–Gould modes will be considered in Chapter 4.

2.3 Antenna Radiation Resistance Results

2.3.1 Antenna Radiation Resistance Spectra

Figure 2.2 shows the spectra of the radiation resistance (R) for the four antennas and standard conditions. We designate the radial mode number by the symbol N_r. Separate radial modes are easily identifiable, except for the second radial mode, N_r=2, of the m=0 loop antenna. From the spectra we observe that the first radial mode, N_r=1, is always dominant. The double half-turn and helical antennas excite an almost pure m=+1 mode, whilst the double saddle coil also excites a strong m=+3 mode in addition to m=+1. There is practically no indication of m=–1. The radiation resistance integrated over the k_z-spectrum for this mode, $R_\Sigma(m$=–1), is very small (of the order of 10^{-3} — 10^{-4} Ω), and no radial modes of m=–1 are observable. The k_z-spectrum of the m=0 loop is much smoother and covers a smaller

region of k_z than that of $m = +1$ and $+3$. Due to the inherent directivity, the spectrum of the helical antenna is strongly asymmetric in favour of positive k_z's.

From these results we can conclude that the R_{rad} is concentrated in propagating modes. This is at first surprising since inductive sources (rf driven sources without a magnetic field) can have high antenna loading resistances even though they couple to the plasma by transformer action. Like any transformer, their coupling depends on the plasma dissipation. Very large parasitic losses can also occur if an antenna contacts the plasma directly either by direct conductance or capacitance. Here the antenna voltage can drive a sheath current that flows in the plasma. Clearly sheath currents are not modelled here and in any case are negligible if the antenna has a low contact admittance to the plasma. For helicon wave driven sources this is usually the case. We therefore realize the major result of this Chapter. The power coupled to a plasma in a helicon wave driven plasma source depends mainly on the helicon wave. This separates the discharge physics from the antenna coupling problem.

We have also verified that the total R_{rad} varies by less than 10% for a factor of 0.1 — 100 increase in the collision frequency. These values encompass the wave damping rates observed in the experiments.

The total antenna resistance results can be summarized as follows:

- $R_{rad} = 0.0234\ \Omega$ for the double half-turn antenna;
- $R_{rad} = 0.192\ \Omega$ for the m=0 loop;
- $R_{rad} = 2.23\ \Omega$ for the double saddle coil, and $R_\Sigma(m{=}{+}1) = 1.9\ \Omega$ and $R_\Sigma(m{=}{+}3) = 0.273\ \Omega$, respectively;
- $R_{rad} = 2.13\ \Omega$ for the helical antenna.

The double saddle coil and helical antennas have similar R_{rad} which are by far the largest. These values would allow a significant fraction of the transmitter power to be coupled to the plasma because it is a simple matter experimentally to reduce the equivalent antenna loading resistance due to losses in the matching network down to a level lower than 1 Ω. This is the practical reason why it is important to study R_{rad} and compare it for different antennas.

The m=0 antenna has a low R_{rad} which would make the design of a matching network difficult at these frequencies. The double half-turn antenna has by far the lowest R_{rad}. This is unexpected on the basis of the similarity of this antenna to the double saddle coil, because the field aligned elements of the double saddle coil cannot couple to waves in a plasma that imposes $E_z = 0$. Plasma wave coupling therefore occurs via the azimuthal and radial elements. In addition, the outer azimuthal element fields are shielded due to the proximity of the conducting wall. In fact, if we move this element outside the conducting wall by taking $s_1 - d > b$, R_{rad} does not change radically and becomes 0.045 Ω.

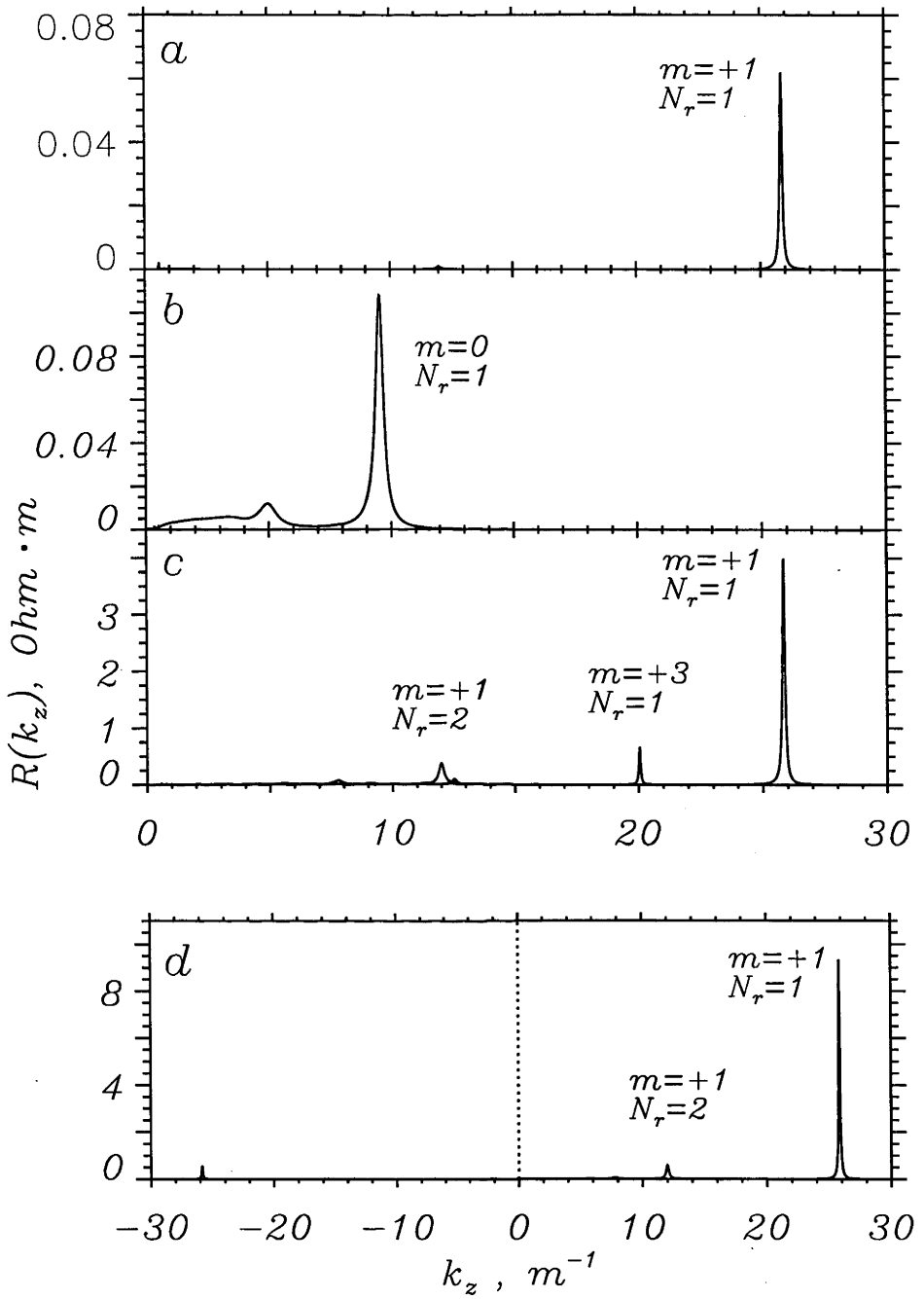

Figure 2.2: Antenna radiation resistance spectra for standard conditions: (a) double half-turn antenna, (b) m=0 loop, (c) double saddle coil, (d) helical antenna. Spectra (a), (b) and (c) are symmetric, and only $k_z \geq 0$ is shown.

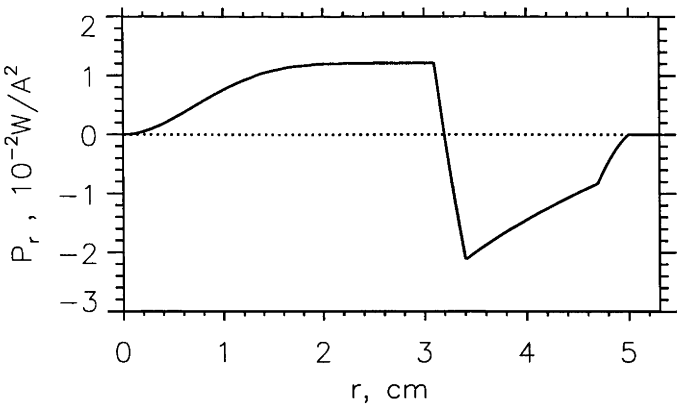

Figure 2.3: The radial Poynting vector flux (see also § 4.4) for the double half-turn antenna and standard conditions.

The poor R_{rad} of the double half-turn antenna is explained by two factors. The first is that even though the double half-turn antenna has azimuthal elements that extend 180^0 compared with 90^0 in the case of the double saddle coil, the double half-turn antenna has only one pair of azimuthal elements and they are parallel fed (Appendix B (A)). In the double saddle coil there are two pairs of azimuthal elements along the field and these are series fed. These effects already produce a factor of 8 reduction for the first radial mode of m=+1 compared with the double saddle coil. A second factor is the parasitic influence of the radial elements. The current in these is out of phase with the electric field generated by the inner azimuthal elements, so that they "reabsorb" a large portion of the power radiated by the inner coil (Fig. 2.3).

The radiation resistance of the radial elements has a negative value of $-0.034\ \Omega$. These conclusions can be verified by calculating the radiation resistance for the inner azimuthal elements alone of the double half-turn antenna for the $\{m$=+1, N_r=1$\}$ mode. We obtain $R = 0.175\ \Omega$ which is exactly 8 times smaller than the radiation resistance of the same mode for the double saddle coil (1.4 Ω).

It is worth noting from a practical point of view that antennas are best designed as series fed elements. The low R_{rad} for the double half-turn antenna is partly an artifact of the antenna geometry used in the computations. In an experiment, choosing to parallel feed antenna elements can be a costly mistake. The high current in the main antenna feed for a parallel fed antenna would increase the parasitic losses in the matching network for a given antenna radiated power. By the same token, the increased voltage for a series fed antenna is not usually a problem in low power plasma sources.

The helical antenna is the most economical antenna in the sense that the wave energy propagates mainly in one direction along the magnetic field. It is of interest to see how this property is affected by the antenna length. We varied the length L

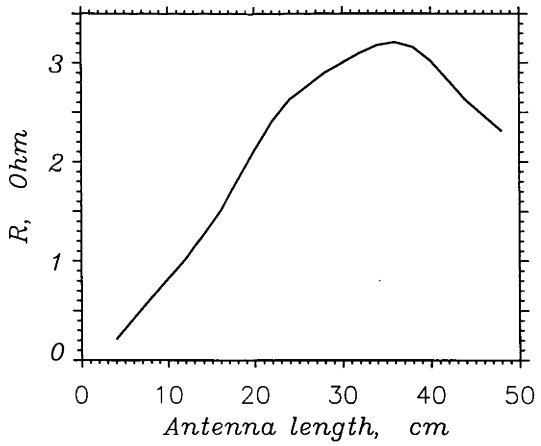

Figure 2.4: The radiation resistance of the helical antenna vs antenna length for a constant axial length of one helical turn, $\lambda = 40$ cm and standard parameters.

of the helical antenna from $L = 4$ to 48 cm, keeping the length of one turn of the helix $\lambda = 40$ cm constant (i. e., increasing the rotation angle proportionally to L). Other parameters were standard. The result is shown in Fig. 2.4. For all lengths $L \geq 4$ cm, more than 90% (more than 99% for $L \geq 20$ cm) of the radiated power goes to m=+1, and the mode $\{m$=+1, N_r=1$\}$ with $k_z \approx 26$ m^{-1} dominates the spectrum. For small L the spectrum is nearly isotropic. The antenna directivity is already satisfactory ($\geq 80\%$) at $L \geq 10$ cm.

In fact, the dependence of R_{rad} on L shown in Fig. 2.4 approximately arises from the factor $\sin\{(k_z/2 - \pi/\lambda)L\}$ in the antenna current spectrum (Appendix B (D)). A maximum in the R_{rad} occurs at $L \approx 36$ cm. This maximum versus L is at first surprising because it seems that once the helical antenna has been optimized for the excitation of a specific k_z (the first radial mode of m=+1), the antenna coupling should increase monotonically with L. This is based on the practical design criterion normally used for helical antennas, that the axial length of one turn of the helix should be equal to the axial wavelength, $\lambda = \lambda_{wave} \equiv 2\pi/k_z$. This is correct only for an infinitely long antenna. For a realistic finite length helical antenna, azimuthal elements play a very important role, and the k_z corresponding to the maximum in the antenna spectrum depends on all m, L and λ. The correct optimization criterion can be obtained using the spectrum formula in Appendix B (D). In Appendix B (D) we demonstrate that for a $\lambda/2$ helical antenna (Fig. B.1(d)) and m=+1 the λ optimum for a specific k_z is $\lambda_{opt} \approx 10.5/k_z$ (Fig. B.3). This means for our standard conditions that such an antenna is optimum with $\lambda \approx 40$ cm for m=+1, $k_z = 0.26$ cm^{-1} ($\lambda_{wave} = 2\pi/k_z \approx 24$ cm (!)). From Fig. 2.4 we also see that a finite length helical antenna is optimum for a wavelength that differs from that for an infinite antenna.

It is easy to demonstrate that the helical antenna of Fig. B.1(d) has a positive

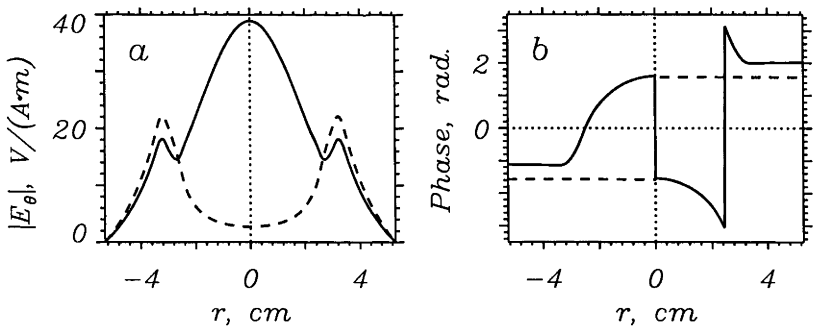

Figure 2.5: The radial profiles of $|E_\theta|$ (a) and the phase of E_θ (b) for m=+1 (designated by the solid line) and m=−1 (designated by the dashed line) at $z = 10$.cm, for the double saddle coil and standard parameters.

helicity (see Appendix B (D)). If the antenna is tuned to excite a particular k_z, it launches $k_z/m > 0$ parallel to the magnetic field and $k_z/m < 0$ modes antiparallel to the field [19, 119]. The virtual absence of wave modes for $k_z < 0$ in the helical antenna spectrum is due to the absence of modes with $m < 0$. This conclusion is in good agreement with most experiments where $m < 0$ modes have not been observed and explains the fact that helical antennas tend to form plasmas in the direction along the magnetic field where the antenna permits $m > 0$ modes to propagate.

The poor excitation of the negative m modes in high density helicon sources is due almost entirely to the effect of the plasma density profile, which prevents the wave fields of the negative m modes from penetrating to the plasma interior. (In addition, in a homogeneous plasma, the radial field structure and the location of the antenna outside the plasma boundary are not favorable for excitation of m=−1 [19], but this is a secondary effect.) The same asymmetry in the excitation of positive and negative m-modes has been observed in the WKB model applied to large scale plasmas [134, 135] (it was not so prominent there) where it has been attributed to a more extensive non-transparency region at the plasma edge for the modes $m < 0$. For small plasmas this non-transparency region can occupy the whole plasma volume. The radial profiles of the electric field of m=+1 and m=−1 modes shown in Fig. 2.5 also suggest that this asymmetry is due to different plasma transparency for positive and negative m's: while for m=+1 the wave electric field is concentrated in the plasma (Fig. 2.5(a)) and the wave propagates inward (the phase grows towards $r = 0$, Fig. 2.5(b)), for m=−1 the wave is localized near the plasma edge (Fig. 2.5(a)) and the phase is almost constant (Fig. 2.5(b)) suggesting that the field of m=−1 is radially evanescent.

To demonstrate the effect of the plasma density profile, we now analyze the radial differential equation (2.3) using WKB methods [134, 135]. Strictly speaking, a WKB-approximation is not applicable for precise computations under our standard

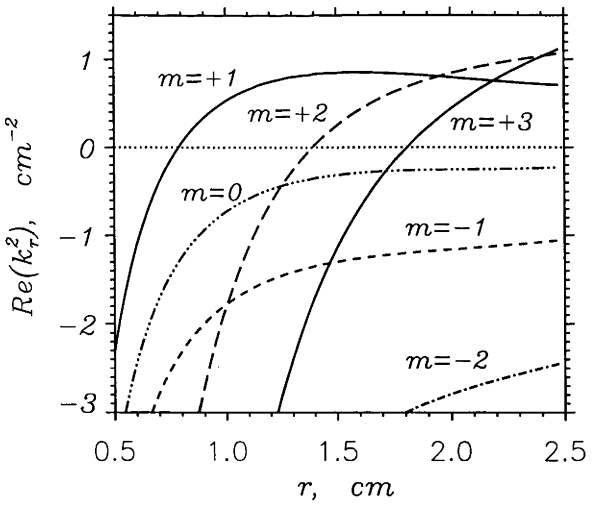

Figure 2.6: Quasiclassical $Re[k_r^2(r)]$ for standard conditions, $k_z = 25$ m^{-1} and m from -2 to $+3$.

conditions, because modes having low radial mode numbers are excited ($N_r < 6$). Nevertheless, it gives us a simple and physically evident picture that explains the poor coupling of negative m modes.

By substitution of the following variables in Eq. (2.3),

$$u = E_\theta \sqrt{\mu}\,, \qquad r = e^\tau\,, \qquad \mu = -A/k_1^2\,,$$

in the absence of external currents, we obtain the standard WKB form:

$$\frac{d^2u}{d\tau^2} + k_\tau^2(\tau) \cdot u = 0\,. \tag{2.14}$$

Equation (2.14) allows us to construct a WKB-solution for $E_\theta(r)$. For example, in the transparency region, where $Re(k_r^2) > 0$, and far from the turning points ($Re(k_r^2) = 0$) it takes the following form:

$$E_\theta(r) \sim \frac{1}{\sqrt{\mu r k_r}} \sin\left(\int_{r_1}^{r} k_r(t)dt \;+\; \frac{\pi}{4}\right)\,,$$

where r_1 is the inner turning point, and

$$k_r^2(r) = \frac{1}{\mu}\left[k_\perp^2 + \frac{r}{2}\left(\frac{2m\bar{\varepsilon}_2 - A}{k_1^2 r^2}\right)' - \frac{\mu''}{2} + \frac{(\mu')^2}{4\mu}\right]\,. \tag{2.15}$$

(Note that we must make the substitution $r = e^\tau$ first, to eliminate the singularity at $r = 0$ which is close to r_1, in order to construct a mathematically correct WKB-approximation.)

The dependence of $Re(k_r^2)$ on radius for the standard plasma parameters, $k_z = 25$ m^{-1} and different m's is shown in Fig. 2.6. The m=+1 mode has the most

extensive transparency region. Just the same, since $max[Re(k_r^2)] \simeq 1$ cm^{-2} and $a = 2.5$ cm, WKB theory can only be applied for a qualitative analysis to this case. The plasma is least transparent to modes with negative m, for which $Re(k_r^2)$ is most negative. They are radially evanescent in the plasma.

It is clear that in Eq. (2.15) and on the left hand side of Eq. (2.3) the only term dependent on the sign of m also appears with the quantity

$$\frac{d}{dr}\left(\frac{\bar{\varepsilon}_2}{k_1^2 r^2}\right) . \tag{2.16}$$

By evaluating different terms in this expression, one may deduce that for small plasma radii the difference in transparency with respect to the sign of m is caused primarily by the plasma density gradient. (However, there are still some purely geometric effects in (2.16) which become important at $r \rightarrow 0$ and which prevent the efficient excitation of m=–1 by a small antenna placed in the plasma center where the density profile is almost flat; such an option has been tried and gave negative results.)

To conclude this Section, we note that accurate computation of the imaginary part of the antenna impedance requires a much broader interval for k_z (up to 600 — 1500 m^{-1}) and a much larger number of azimuthal modes (up to 15 — 20). In experiments however, a significant part of the actual antenna inductance is due to feeder lines from the matching network that play no role in the wave coupling. Their effect is not modelled in these computations.

2.3.2 Frequency Dependence of the Antenna Radiation Resistance

For standard parameters we varied the frequency in the range 0.3 — 60 MHz. The results in Fig. 2.7 show that R_{rad} increases with frequency in all cases as expected for an inductive coupling. The double saddle coil and the helical antenna have by far the highest R_{rad} over the whole frequency range. The "plateau" in the range $f \approx 20$ — 35 MHz for the double saddle coil and the helical antenna is caused by the antenna geometry. The mode $\{m$=+1, N_r=1$\}$, which dominates the spectrum at low frequencies in both cases, disappears at $f \approx 40$ MHz for the double saddle coil and at $f \approx 35$ MHz for the helical antenna. As a result, the R_{rad} at high frequencies becomes dominated by higher order radial modes. In addition, a broad continuum appears at relatively small k_z, which we identify as the sum of many high radial modes. The spectrum becomes broader: for $f = 60$ MHz, $|k_z| \lesssim 45$ m^{-1} for the m=0 loop and $|k_z| \lesssim 70$ m^{-1} for the other antennas (Fig. 2.8(a)). At very low frequencies there is no observable waveguide cutoff, despite the fact that R_{rad} goes exponentially to zero at $f \lesssim 5$ MHz.

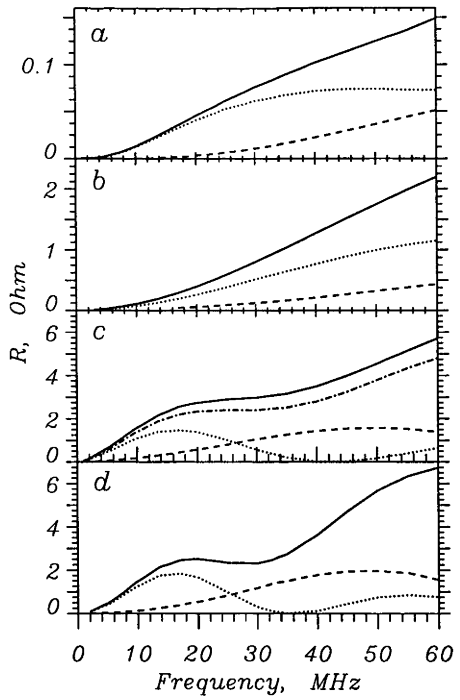

Figure 2.7: Radiation resistance vs antenna excitation frequency: (a) double half-turn antenna, (b) m=0 loop, (c) double saddle coil, (d) helical antenna. The total R_{rad} is shown by the solid line, the dotted line designates $R(N_r{=}1)$ (of m=0 for (b) and m=+1 otherwise), the dashed line designates $R(N_r{=}2)$ and the dashed–dot line in (c) designates $R_\Sigma(m{=}{+}1)$.

We also performed calculations of R_{rad} for the m=0 loop and the double saddle coil for the case of a H^+ plasma. Negligible difference was noted in R_{rad} for the double saddle coil for each gas. For the R_{rad} of the m=0 loop, shown in Fig. 2.9, there is a visible cutoff at low frequencies. This is expected because the waveguide cutoff for the fast wave is known to persist for axisymmetric modes in plasmas bounded by non-conducting walls [46]. This occurs at $f \approx 15$ MHz for our conditions. No radial modes are present below this frequency. The appearance of N_r=1 at $f \approx 16$ MHz (and then N_r=2 at $f \approx 30$ MHz), gives rise to jumps in R_{rad}.

Since we can usually separate different radial modes, we can study the wave dispersion properties. Figure 2.10 shows k_z vs frequency for $m = 0, +1$ and $N_r = 1, 2$ in argon and hydrogen plasmas. The cutoffs for m=0, as well as the cutoff for $\{m{=}{+}1,\ N_r{=}2\}$ in a H^+ plasma are quite evident in the figure. The cutoffs are expected, for these modes are well known to propagate as "body" waves [45, 46]. The first radial mode of m=+1, however, shows no cutoff in hydrogen and consequently has similar dispersion in both argon and hydrogen. The absence of a cutoff is due to the fact that the $\{m{=}{+}1,\ N_r{=}1\}$ mode propagates as a "surface" wave in a plasma with a vacuum boundary [45, 46]. The cutoff is avoided in this case because the

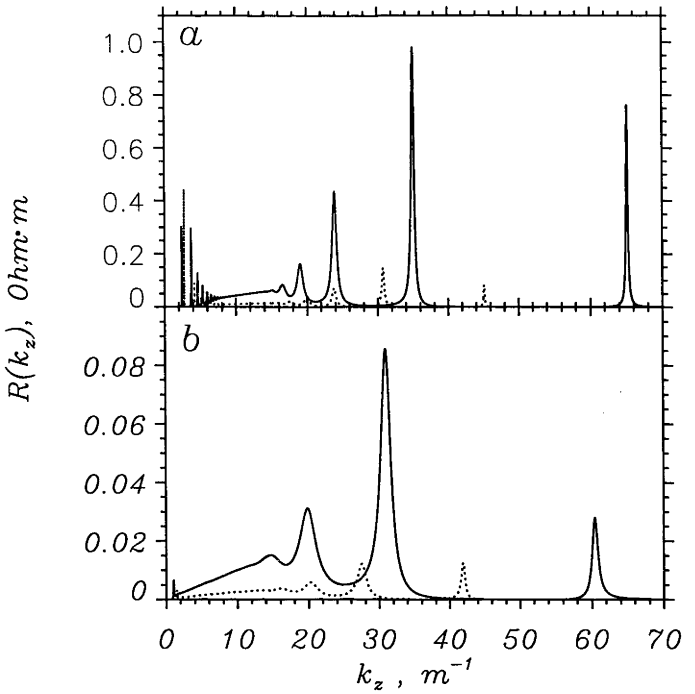

Figure 2.8: Radiation resistance k_z-spectra of the double saddle coil: (a) for $f = 60$ MHz and standard parameters, (b) for $n_{e0} = 4 \times 10^{19}$ m^{-3} and standard parameters. m=+1 is shown by the solid line, m=+3 is shown by the dotted line.

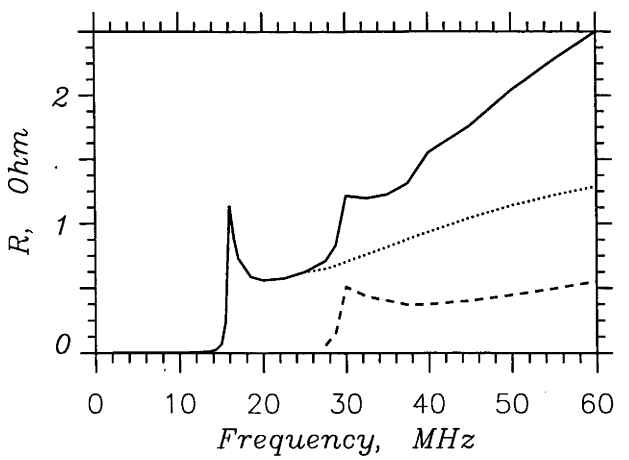

Figure 2.9: Radiation resistance vs frequency for the m=0 loop and a H^+ plasma. The designations of the curves are as in Fig. 2.7.

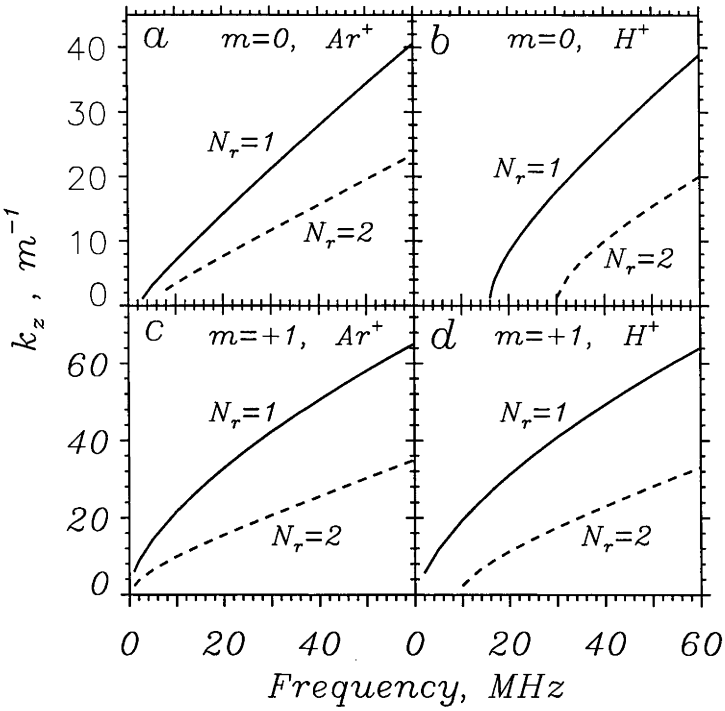

Figure 2.10: k_z of the first and second radial modes vs frequency for m=0 (a), (b) and m=+1 (c), (d) in an Ar^+ plasma (a), (c) and in a H^+ plasma (b), (d).

uniform plasma perpendicular wavenumber $\rightarrow 0$ as $\omega \rightarrow 0$. Detailed measurements have indeed established (directly or indirectly) the fact that this mode has no cutoff [48, 91, 111].

The shape of the curves of the first radial mode dispersion in Figs. 2.10(c) and (d) suggest that this wave obeys the simple high frequency whistler wave dispersion relation, $k_z^2 c^2 \approx \omega\omega_{pe}^2/\omega_{ce}$ (Eq. (4.20)), over the present range of frequencies. We have verified that the whistler wave dispersion relation gives a qualitatively correct value for the dependence of k_z over the complete experimental range of parameters for the $\{m$=+1, N_r=1$\}$ helicon wave in a uniform plasma bounded by a vacuum. It does however overestimate k_z by about 30% in some cases.

2.3.3 Effect of Plasma Density and Density Profile

Figure 2.11 shows the R_{rad} versus central plasma density in the range $n_{e0} = 2.5\times10^{17}$ — 10^{20} m^{-3} for the double saddle coil and for otherwise standard case parameters. At low densities the R_{rad} increases with density as it did in the frequency scan. In the range $n_{e0} \approx (1 - 3)\times10^{19}$ m^{-3} the total R_{rad} decreases. Once again, this results from the disappearance of the $\{m$=+1, N_r=1$\}$ mode, when this antenna is one wavelength long. At low densities, the antenna spectrum consists of a set of very narrow peaks. The interval of k_z, covered by the spectrum, is small: $|k_z| < 4$ m^{-1} for $n_{e0} = 2.5 \times 10^{17}$ m^{-3}. For large densities the spectrum is rather smooth

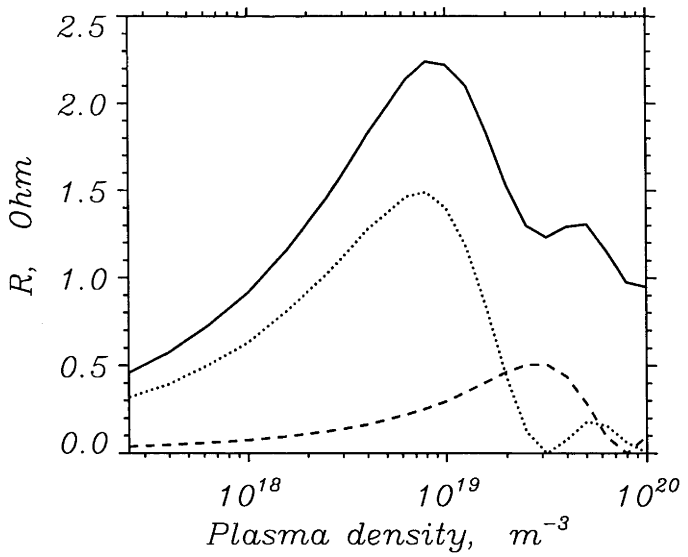

Figure 2.11: Radiation resistance vs central plasma density for the double saddle coil and standard system parameters. Designations of the curves are as in Fig. 2.7.

and broad ($|k_z| \lesssim 120$ m^{-1} for $n_{e0} = 10^{20}$ m^{-3}), and it is difficult to distinguish separate radial modes. Higher radial modes play a more important role than the N_r=1, and an extensive continuum for smaller k_z's also appears (Fig. 2.8(b)).

The important result to note is that the R_{rad} decreases and does not remain constant as it did for the frequency scan. This observation has important implications for the understanding of how the discharge formed by the wave may attain an equilibrium density. We assume that the power absorption is local in a collisional plasma. As the density rises, the R_{rad} and hence power coupled to the plasma increases at first. If the plasma losses are proportional to the plasma density, then the density will reach a value where the radiated rf power equals the power loss. If the power loss-line versus density intersects the rf radiated power at densities where R_{rad} is decreasing, the operating point is stable. This is because an increase/decrease in the density will cause a decrease/increase in the power fraction coupled to the plasma and hence a stabilization of the density.

The above conclusions only apply at a fixed density profile. In reality, the plasma density profile is also free to vary during the plasma build-up, and will be instrumental in determining the final equilibrium. We have investigated the effect of the plasma density profile on the R_{rad} of the double saddle coil. The profile function assumed was the following:

$$\frac{n_e(r)}{n_{e0}} = \left(1 - \frac{r^2}{a^2}\right)^{2^\gamma}, \tag{2.17}$$

where γ was varied from -3 to 3. For $\gamma = 3$ the profile is strongly peaked in the center, while for $\gamma = -3$ it is rather flat, except near the plasma boundary (Fig.

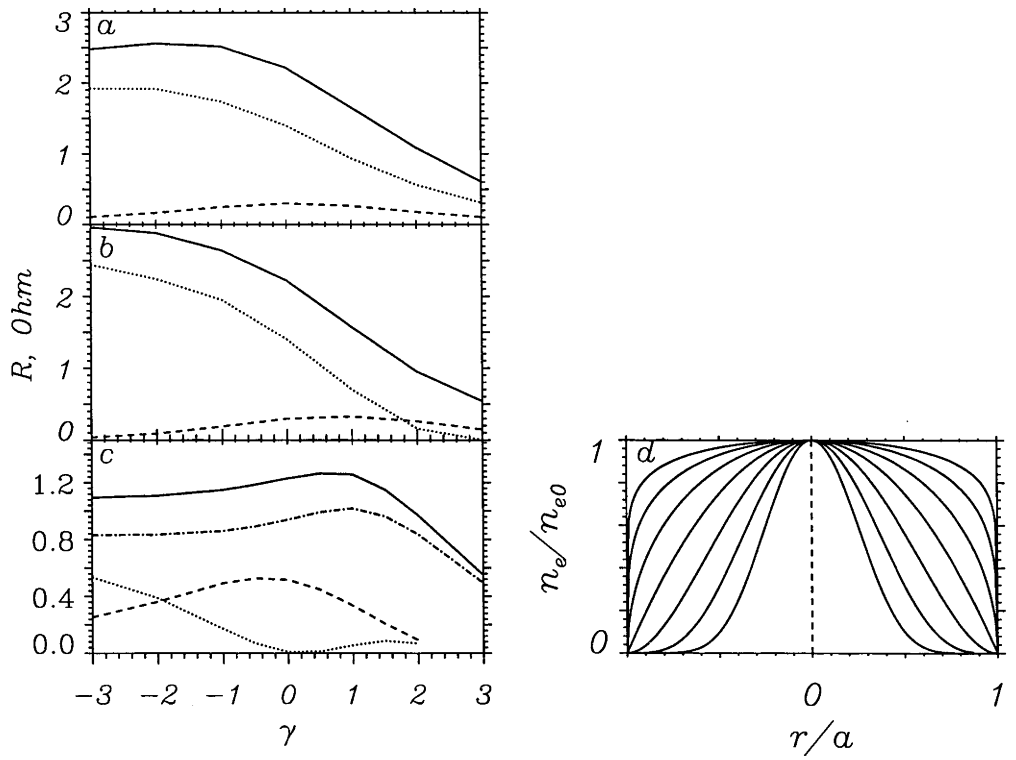

Figure 2.12: (a) — (c): Radiation resistance of the double saddle coil vs the plasma density profile parameter γ of Eq. (2.17). γ is varied (a) for fixed central density $n_{e0} = 10^{19}$ m^{-3}, (b) for fixed average density $\langle n_e \rangle = 5 \times 10^{18}$ m^{-3}, and (c) for fixed average density $\langle n_e \rangle = 1.5 \times 10^{19}$ m^{-3}. Other system parameters are standard. Designations of the curves are as in Fig. 2.7. (d): Variation of the density profile with γ from −3 to 3.

2.12(d)).

The results are presented in Figs. 2.12(a) — (c). Figure 2.12(a) shows results for a fixed central density $n_{e0} = 10^{19}$ m^{-3} and Fig. 2.12(b) for fixed average density $\langle n_e \rangle = 5 \times 10^{18}$ m^{-3}. The decrease over the range $\gamma = [-3, 0]$ is relatively small. R_{rad} decreases more rapidly as the profile becomes steeper. This indicates that for a double saddle coil the peripheral plasma strongly affects the antenna coupling as the antenna is located further from the bulk of the plasma for $\gamma > 0$. If we keep $\langle n_e \rangle$ constant at 1.5×10^{19} m^{-3}, i. e. 3 times greater than in the standard case [Fig. 2.12(c)], R_{rad} remains rather steady in the range $\gamma \approx [-3, 2]$. It is interesting, that in this case the disappearance of $\{m{=}{+}1,\ N_r{=}1\}$ (due to the effect of the antenna k_z-spectrum) at $\gamma \approx 0$ is compensated by other modes and does not affect the overall R_{rad}.

When $n_{e0} = 10^{19}$ m^{-3} is fixed [Fig. 2.12(a)], the k_z-spectrum is only slightly "compressed" to lower values when γ changes from −3 to 3. On the other hand, when the average density $\langle n_e \rangle$ is fixed [Figs. 2.12(b) and (c)], the change of the

density profile has a strong effect on the antenna spectrum. A set of sharp peaks occur at small k_z's when $\gamma = -3$ ("flat" profile). As γ increases, the k_z values of the radial modes get larger, and finally, the spectrum becomes broad and continuous at $\gamma = 3$. We conclude that, at least for small plasma radii, it is important to take into account the specific density profile. However, for fixed $\langle n_e \rangle$ and $\gamma < 1$ it is not a bad approximation to calculate R_{rad} for $m > 0$ modes using a uniform plasma model with a vacuum boundary. However, such a model is inappropriate for $m < 0$ modes.

These results complicate the above 0D plasma balance picture but do suggest that an increase in rf power at full ionization is likely to lead to a steepening of the radial profile so as to decrease the R_{rad}. The mechanism is not clear by which the rf power can actually cause such a profile change. One possible mechanism that has been suggested is the effect of the ponderomotive force [105, 108, 129, 130].

2.3.4 The Effect of Locating the Antenna in the Plasma

We may locate the double saddle coil in the plasma by making $s = 1.5$ cm, whilst keeping all other parameters as in the standard case. The total R_{rad} increases considerably to the value $R_{rad} = 7.51\ \Omega$, and $R_\Sigma(m{=}{+}1) = 5.25\ \Omega$ (despite this antenna is twice smaller than the standard one). This is to be compared to the standard case, for which $R_{rad} = 2.23\ \Omega$. The effect of placing the conducting wall at the plasma edge, $b = a = 2.5$ cm, causes R_{rad} to decrease slightly to the value $R_{rad} = 5.18\ \Omega$. In this case, the wave excited spectrum is compressed to $|k_z| \leq 20$ m^{-1}. In all cases $R_\Sigma(m{=}{-}1)$ is very small.

A surprising result occurs if, in addition to placing the antenna in the plasma ($s = 1.5$ cm) and the conducting wall at the plasma boundary ($b = a = 2.5$ cm), we make the plasma density profile uniform at the value $n_e = 5 \times 10^{18}$ m^{-3}. In this case, R_{rad} drops again to the value $R_{rad} = 3.02\ \Omega$, but at the same time $R_\Sigma(m{=}{-}1)$ becomes almost as large as $R_\Sigma(m{=}{+}1)$. We find that $R_\Sigma(m{=}{+}1) = 1.34\ \Omega$, $R_\Sigma(m{=}{-}1) = 1.11\ \Omega$. This confirms our conclusion that the plasma density gradient is primarily responsible for the poor excitation of $m{=}{-}1$. The k_z-spectrum of R for this latter case is shown in Fig. 2.13.

2.3.5 The Effect of Device Size

Helicon plasma sources vary in radius over the range 2 — 20 cm, so it is of interest to increase the machine size to see how our previous conclusions are affected. We consider two cases that are more typical of low density, low field plasma sources, bearing in mind that at lower densities the model is less reliable due to the effects of parallel electron dynamics.

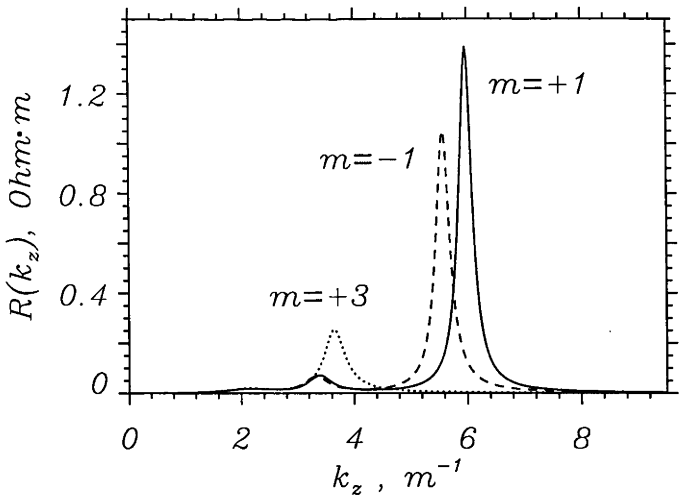

Figure 2.13: Spectrum of the radiation resistance for a double saddle coil placed in a uniform plasma, $s = 1.5$ cm, $a = b = 2.5$ cm, $n_e = 5 \times 10^{18}$ m^{-3} = *const.*

Consider a machine with dimensions about three times larger than those in the standard configuration but typical of those used for plasma processing [106] with $a = 7.5$ cm, $s = 8.1$ cm, $s_1 = 14.7$ cm and $b = 15$ cm. We therefore employ a lower plasma density $n_{e0} = 10^{18}$ m^{-3} (parabolic profile) and magnetic field $B_0 = 0.01$ T. In order to keep the excitation conditions as similar as possible for the different machine sizes, the antenna length was adjusted to optimize the excitation of $\{m{=}{+}1,\ N_r{=}1\}$ with $k_z \approx 34$ m^{-1}, even though the $\{m{=}{+}1,\ N_r{=}2\}$ mode dominates the spectrum in this case, having a radiation resistance that is about twice as large as that of $\{m{=}{+}1,\ N_r{=}1\}$. This leads to the antenna length values of $L = 9.3$ cm for the double saddle coil and $L = 15.5$ cm ($\lambda = 31$ cm) for the helical antenna. We obtain the following radiation resistances:

- $R_{rad} = 0.306\ \Omega$ for the double half-turn antenna;
- $R_{rad} = 2.28\ \Omega$ for the $m = 0$ loop;
- $R_{rad} = 3.14\ \Omega$ for the double saddle coil;
- $R_{rad} = 2.19\ \Omega$ for the helical antenna.

Again, $m{=}{+}1$ is the most efficiently excited mode. For the double saddle coil, the azimuthal modes $m{=}{-}1, {+}3$ and $+5$ are also efficiently excited: $R_\Sigma(m{=}{-}1) = 0.11\ \Omega$, $R_\Sigma(m{=}{+}3) = 0.54\ \Omega$ and $R_\Sigma(m{=}{+}5) = 0.2\ \Omega$. The lower density gradient, due to the lower n_e and larger a, is observed to improve the excitation efficiency of $m{=}{-}1$. Note also that the $m{=}0$ antenna is more efficient than in smaller devices.

For system dimensions about 5 times larger than that for the standard case: $a = 12.5$ cm, $s = 13.1$ cm, $s_1 = 24.7$ cm and $b = 25$ cm, and $n_{e0} = 5 \times 10^{17}$ m^{-3} and $B_0 = 0.005$ T, the antenna lengths have been chosen again to optimize the

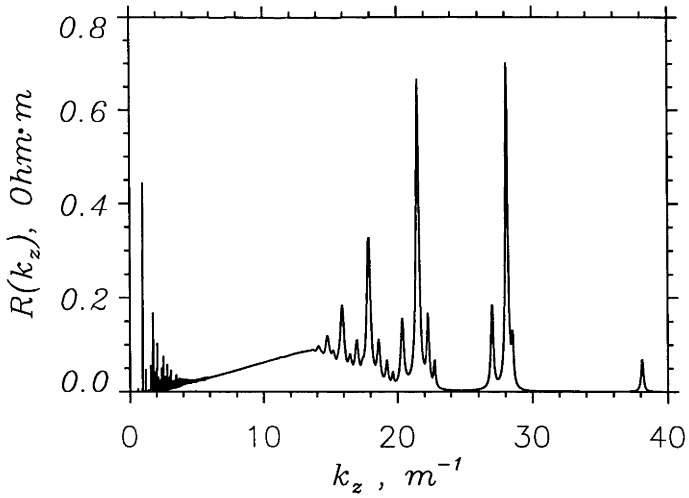

Figure 2.14: Spectrum of the total radiation resistance for a double saddle coil for $a = 12.5$ cm, $b = 25$ cm, $n_{e0} = 5 \times 10^{17}$ m^{-3} and $B_0 = 0.005$ T.

excitation of $\{m{=}{+}1,\ N_r{=}1\}$ at $k_z \approx 38$ m^{-1}. This leads to the values $L = 8.2$ cm for the double saddle coil and $L = 13.8$ cm ($\lambda = 27.6$ cm) for the helical antenna. The radiation resistances for this case are the following:

- $R_{rad} = 0.7\ \Omega$ for the double half-turn antenna;
- $R_{rad} = 4\ \Omega$ for the $m = 0$ loop;
- $R_{rad} = 3.7\ \Omega$ for the double saddle coil;
- $R_{rad} = 2.3\ \Omega$ for the helical antenna.

Once again, the $m{=}{+}1$ mode dominates the spectrum, but the double saddle coil also excites $m{=}{-}1$ [$R_\Sigma(m{=}{-}1) = 0.43\ \Omega$], $m{=}\ {+}3$, $+5$ and even $m{=}{+}7$ [$R_\Sigma(m{=}{+}7) = 0.12\ \Omega$] fairly efficiently. The k_z-spectrum of R_{rad} for this latter case is shown in Fig. 2.14. Because of the complexity of the spectrum, we do not separate different m-modes in Fig. 2.14, and only show the total $R_{rad}(k_z)$. (Note that in Figs. 2.8 and 2.14 there are sharp spikes at low k_z. Their origin is not completely understood. It has been noticed that this non-physical effect is very sensitive to the radial mesh at the plasma edge. The author believes that this is due to artificial high order radial eigenmode resonances (numerical aliasing) inside the density strata of the finite element mesh. It could also be the manifestation of some kind of numerical pollution (numerical pollution is discussed in Chapter 4), despite the fact that the numerical model presented in § 2.1 is thought to be pollution-free. In any case, we can disregard this effect since those spikes are always extremely narrow and their contribution to the integrated R_{rad} is negligible.)

The helical antenna also excites $m{=}{-}1$ quite efficiently, $R_\Sigma(m{=}{-}1) = 0.37\ \Omega$. It is interesting to note that the k_z-spectrum of this antenna consists almost entirely of

the m=+1 mode for $k_z > 0$ and almost entirely of the m=−1 mode for $k_z < 0$. This demonstrates, in principle, that the m=−1 mode may be launched antiparallel to B_0 in large devices. This was not possible for the smaller device used in the standard case.

Understanding discharge physics is likely to be more difficult in larger machines or small machines at very high density due to the presence of high radial modes. Even though the antenna length and plasma density have been adjusted in the above computations to typical experimental values, that emphasize the excitation of $\{m$=+1, N_r=1$\}$, the efficient excitation of higher order modes may nonetheless occur. In large devices this may be linked to jumps observed in the density as the rf power is increased. Lower densities at low power tend to be supported by $\{m$=+1, N_r=1$\}$. As the power is raised, Fig. 2.11 demonstrates that there is a limiting value that the density can obtain due to the extinction of this mode. At this point, in principle, the plasma can be supported by a higher radial mode of longer wavelength. This is more likely in larger machines, where $\{m$=+1, N_r=2$\}$ is the most efficiently excited mode at the observed density. As previously noted however, it is incorrect to treat radial modes with perpendicular wavenumbers $\gtrsim 300$ m^{-1} due to the neglect of electron mass in the present model.

2.4 Wave Field Structure

Nowadays experimental measurements of the wavefields of the helicon wave in cylindrical devices for antennas of the types modelled here have become quite detailed [19, 40, 95]. In this Section we discuss the field structure produced by the m=0 loop, the double saddle coil and the helical antenna for standard system parameters. The antenna center is located at z=0. The peak amplitude of the antenna current is set to 1 A so that the calculated oscillating electric field amplitudes are in V/(A·m) and magnetic field amplitudes are in T/A in Figs. 2.15 — 2.22. Typical experimental antenna currents are in the range 50 — 200 A.

Figures 2.15(a) — (d) show E_r and E_θ launched by the m=0 loop antenna. Figures 2.15(a) and (b) show contour plots of the amplitude and phase of E_r over the cross section of the plasma up to the plasma boundary (in the vacuum E_r=0 for this antenna). In the z-distribution of the fields we observe a beat structure, which we discuss below. The MHD model cannot be used to calculate wave damping due to the neglect of parallel electron dynamics.

The wave is clearly propagating in the z-direction away from the antenna, as well as in the radial direction towards the center of the plasma. The mode is forward propagating, as expected for the helicon wave. This inward/axial propagation corresponds to the slight angle of inclination of the amplitude contours to the constant magnetic field. This small angle of about 6^0 — 7^0 also occurs in the wavefield

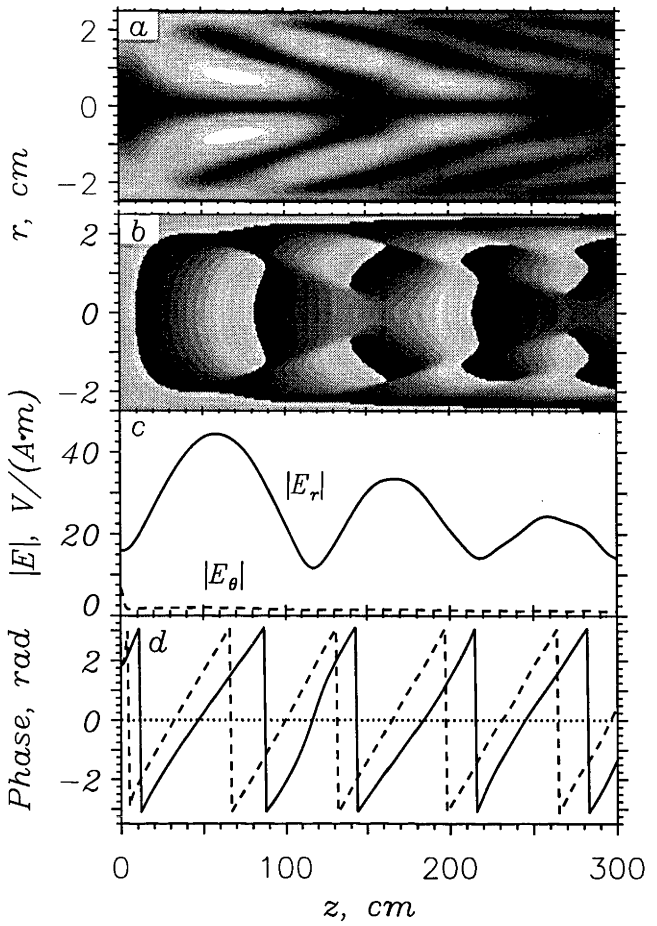

Figure 2.15: The electric fields of the m=0 loop antenna. The amplitude (a) and phase (b) of E_r in the axial cross-section inside the plasma ($r \leq a$). In the vacuum $E_r = 0$. $max|E_r| = 47$ V/(A·m). The amplitude (c) and phase (d) of E_r and E_θ at $r = 1$ cm.

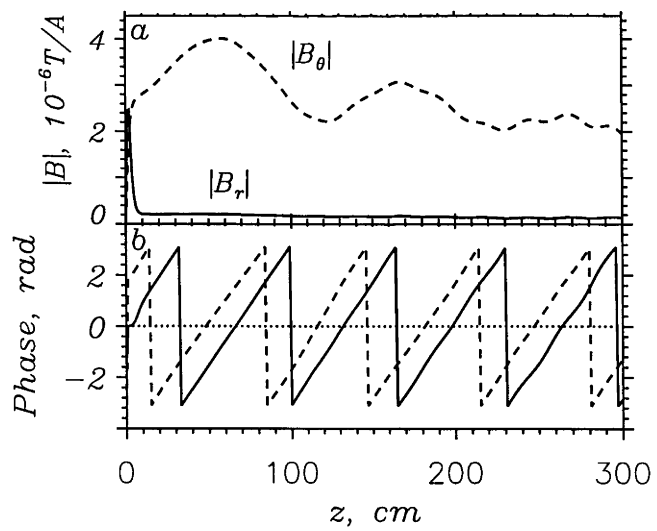

Figure 2.16: The amplitude (a) and phase (b) of B_r and B_θ for the m=0 loop antenna at $r = 1$ cm.

distribution of the same loop antenna, when located in an infinite slab homogeneous plasma that imposes no boundary conditions on the wavefields. The angular inclination of the field pattern to the axis is therefore linked to the field radial mode structure. We also note that the angle of 19.47^0 (the maximum angle of the group velocity of a plane helicon wave to the magnetic field in a uniform plasma [124]), imposes no limitation on the penetration of the fields into the plasma. The evanescent fields of the antenna ensure that the wavefields are non-zero under the antenna (in addition, the very concept of the group velocity is inapplicable in the antenna near field).

Figures 2.15(c) and (d) show the axial profiles of the electric fields at $r = 1$ cm. The extent of the beat pattern and the linearity of the phase are quite evident. The amplitude of E_θ is very small compared to E_r due to the much larger perpendicular than parallel wave number for m=0.

Figures 2.16(a) and (b) show the magnetic field components B_r and B_θ. The beat pattern is still observable on the B_θ field here, but is less evident than for E_r, a property which holds for all antennas. Another fact worth noting is that due to the complicated relation between the axial component of the Poynting flux carried by a wave and its mode numbers [142], the copropagating beat waves are observable, even though the $\{m$=0, N_r=1$\}$ mode carries most of the rf power.

Figures 2.17(a) and (b) show contour plots of E_r and Figs. 2.17(c) and (d) show axial profiles of E_r and E_θ at $r = 1$ mm and $\theta = 0$ for the double saddle coil and for standard conditions. Figure 2.18 shows the axial profiles of B_r and B_θ, and Fig. 2.19 shows contours of E_r and B_z in the azimuthal cross-section at $z = 30$ cm. Once again, the wave fields are observed to propagate away from the antenna in the z-direction, and the beat pattern along the z-direction is evident. Figures 2.17(a) and 2.19(a) indicate that E_r has a large amplitude near the plasma boundary. The interference of the m=+1 and m=+3 modes produces the beat pattern evident in the θ-distribution of Figs. 2.19(a) and (c).

Figures 2.20 — 2.22 show the same results for the helical antenna. The axial distribution of the wavefields of the helical antenna is strongly asymmetric (Figs. 2.20, 2.21), it radiates mainly in the positive z-direction. Despite the fact that the R_{rad} of this antenna is slightly smaller than that of the double saddle coil, the amplitude of the field at its maximum is about 1.3 times larger. This confirms the previous inference that the helical antenna should be more efficient than symmetric antennas for plasma formation. The field amplitude is fairly symmetric in the azimuthal cross-section [Fig. 2.22(a)], since an almost pure m=+1 mode is excited.

We now return to the question of the general nature of the axial beat structure observed for all the antennas. We demonstrate that the beat patterns are due to the interference of several radial modes, mainly those with N_r=1 and N_r=2 of the main azimuthal mode (viz. m=0 for the m=0 loop and m=+1 for the double saddle

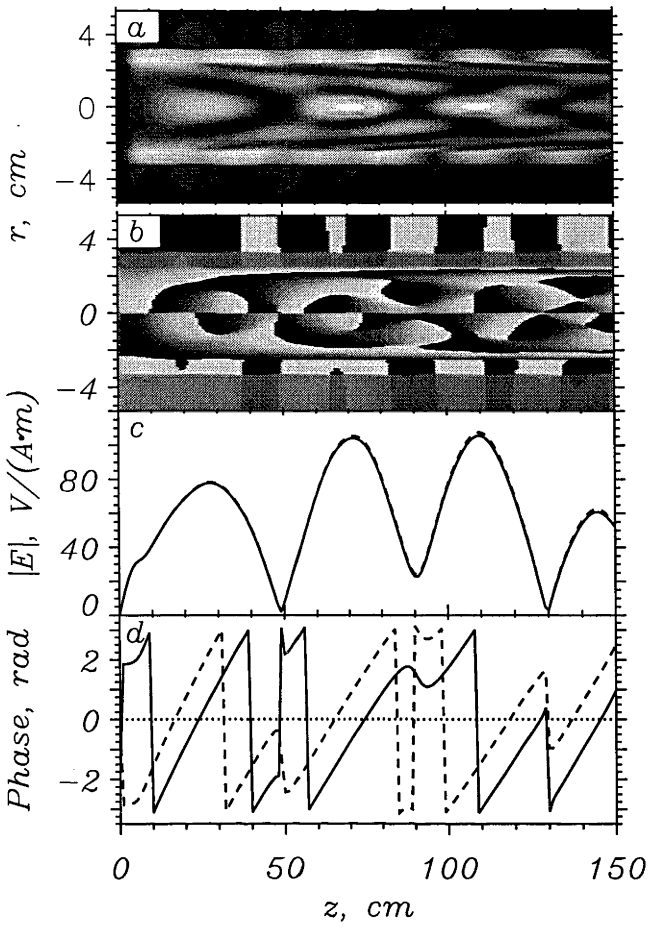

Figure 2.17: The electric fields of a double saddle coil. The amplitude (a) and phase (b) of E_r in the axial cross-section at $\theta = 0$, $max|E_r| = 107$ V/(A·m). The amplitude (c) and phase (d) of E_r and E_θ near the plasma center: $r = 1$ mm and $\theta = 0$; E_θ is shown by the dashed line; $|E_r|$ and $|E_\theta|$ almost overlap.

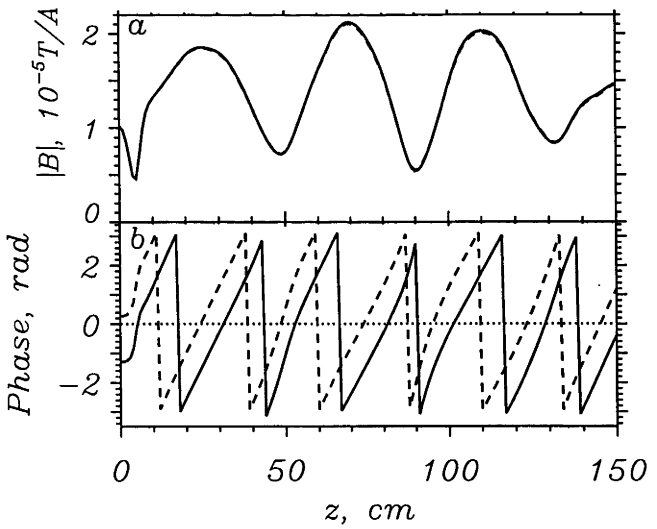

Figure 2.18: The amplitude (a) and phase (b) of B_r and B_θ for a double saddle coil at $r = 1$ mm and $\theta = 0$. B_θ is shown by the dashed line; $|B_r|$ and $|B_\theta|$ overlap.

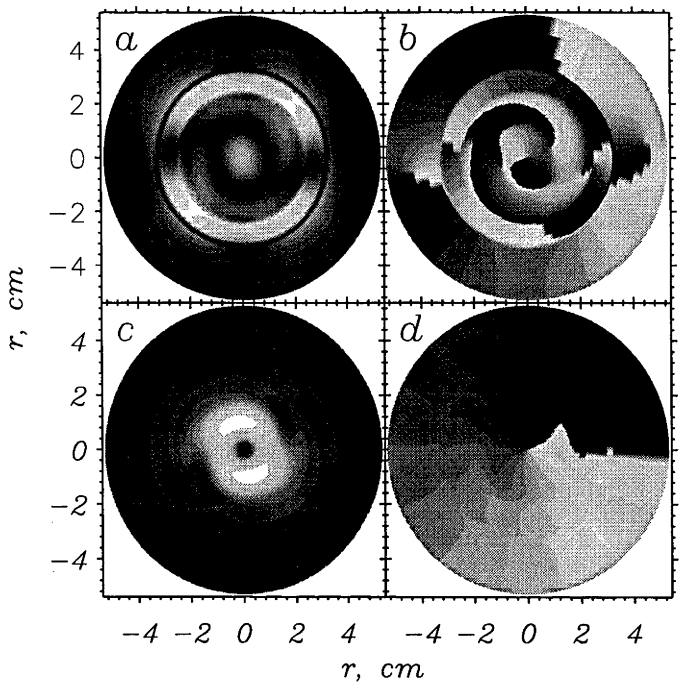

Figure 2.19: (a) $|E_r|$, $max|E_r| = 115$ V/(A·m), (b) phase of E_r, (c) $|B_z|$, $max|B_z| = 7.5 \times 10^{-6}$ T/A, and (d) phase of B_z for a double saddle coil in the azimuthal cross-section at $z = 30$ cm; $\theta = 0$ is vertical.

coil and the helical antenna). The modulation depth of the field amplitude depends on their relative contributions. Despite the fact that the N_r=2 mode has a much smaller radiation resistance than the N_r=1 mode (Fig. 2.2), the second radial mode is nonetheless evident in the wavefield spectrum in the plasma (Fig. 2.23). The higher radial modes (up to N_r=5) are less important than N_r=2, but also figure more prominently in the wavefield spectrum than in the spectrum of the R_{rad}.

To establish this fact, we have simulated the spectrum of $E_\theta(k_z)$ shown in Fig. 2.23 for the double saddle coil by the following function:

$$E_\theta(k_z) = \sum_{N_r} \frac{\alpha_{N_r} \sin(k_z L/2)}{k_z^2 - (k_{zN_r} + i\delta_{N_r})^2} ,$$

where k_{zN_r} is the resonant k_z of N_r'th radial mode. The coefficients α_{N_r} and δ_{N_r} were matched "empirically" to fit the spectrum in Fig. 2.23. With just 2 modes, N_r=1 and N_r=2, the beat structure is similar to that in Figs. 2.17(c) and (d), and with 5 radial modes we obtain a very accurate representation. This suggests that the axial beat patterns observed in experiments [40, 53] are the result of copropagating radial modes.

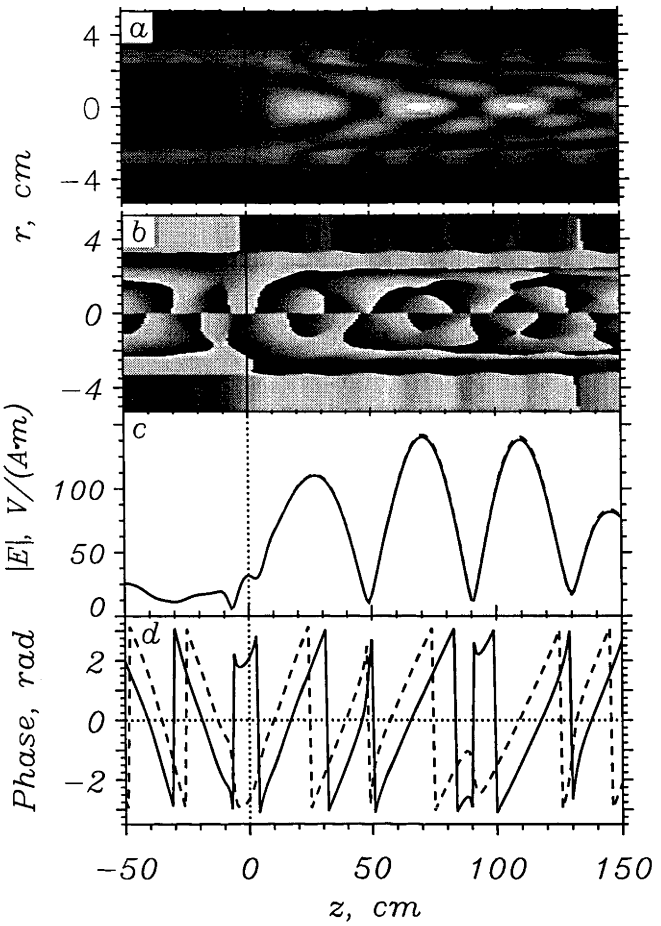

Figure 2.20: The electric fields of a helical antenna. The amplitude (a) and phase (b) of E_r in the axial cross-section at $\theta = 0$, $max|E_r| = 142$ V/(A·m). The amplitude (c) and phase (d) of E_r and E_θ at $r = 1$ mm and $\theta = 0$; E_θ is shown by the dashed line; $|E_r|$ and $|E_\theta|$ overlap.

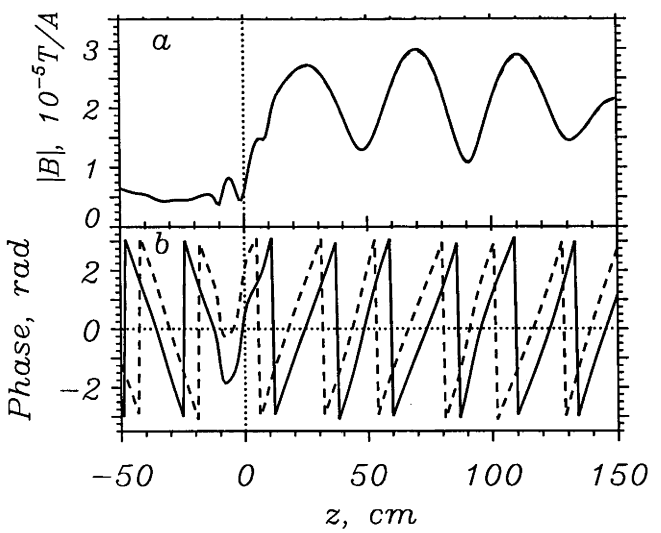

Figure 2.21: The amplitude (a) and phase (b) of B_r and B_θ for a helical antenna at $r = 1$ mm and $\theta = 0$. B_θ is shown by the dashed line; $|B_r|$ and $|B_\theta|$ overlap.

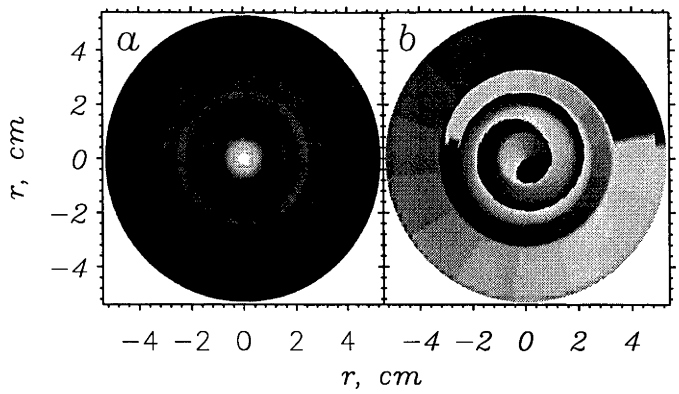

Figure 2.22: (a) $|E_r|$, $max|E_r| = 142$ V/(A·m), and (b) phase or E_r, for a helical antenna in the azimuthal cross-section at $z = 70$ cm.

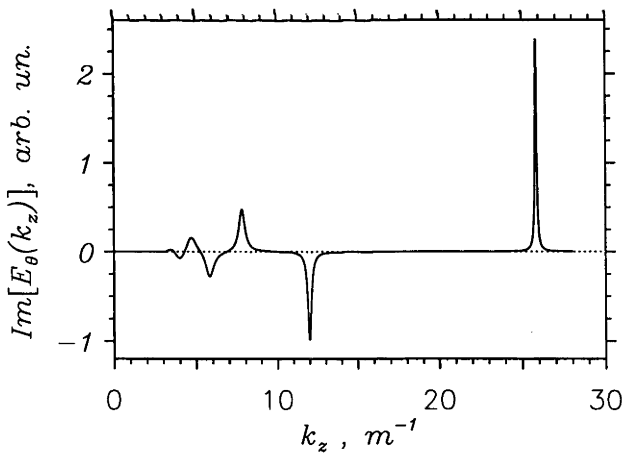

Figure 2.23: k_z-spectrum of the imaginary part of $E_\theta(r, m, k_z)$ for m=+1 at $r = 1$ mm for the double saddle coil and standard conditions. The spectrum is antisymmetric with respect to k_z=0.

Chapter 3

Comparison with Experiment in BASIL

In this Chapter we compare the experimental results obtained in high density, high magnetic field helicon source BASIL with computer simulations using the MHD numerical model described in Chapter 2.

The BASIL experiment is a linear magnetized plasma originally designed as an electrodeless noble gas laser [143, 144]. The uniform static magnetic field is approximately 1.4 meters long with a maximum static magnetic field of 0.2 T. The discharge is produced in an axially mounted pyrex tube of 43 mm inside diameter ($a = 2.15$ cm), with the antenna being external to the tube mid-way along the static field. Radiofrequency powers up to 10 kW could be coupled to the plasma at 7 MHz. The outer conducting boundary used in the code corresponds to the inside of the magnetic field coils in BASIL, $b = 6$ cm. No waves reflected from the plasma ends were observed experimentally, so we choose an infinite cylinder (Appendix A (A)) as the most adequate model for BASIL.

Three antennas were used in the experiment:

- A conventional double saddle coil antenna shown in Fig. B.1(c). Its length is $L = 13$ cm and the angular span of its azimuthal elements is $2\theta_a = 90^0$.
- A pair of phased double saddle coils shown in Fig. B.2(a) each having $L = 13$ cm and $2\theta_a = 45^0$.
- A $(3/2)\lambda$ helical antenna (Fig. B.1(d)) of total length 27 cm and $\lambda = 18$ cm. Compared to the antenna shown in Fig. B.1(d), this antenna has only one azimuthal element at both ends and is capable of exciting the m=0 mode. However, the excitation efficiency of m=0 was always very poor compared to m=+1. This antenna has a positive helicity (Appendix B (D)), strongly coupling to k_z and azimuthal modes satisfying $k_z/m > 0$. Judging from the antenna structure, one may conclude that in the direction along B_0, where

$k_z/m > 0$, the m=+1 mode should be best excited (we will also call it the "$m >$ 0" or "m=+1" direction in this Chapter), whilst in the direction antiparallel to B_0 (the "$m < 0$" or "m=–1" direction) mainly m=–1 would be allowed to propagate.

All antennas are constructed from a 3.7 mm diameter wire ($d = 3.7$ mm in the code). The radius of the inner antenna edge, $s = 2.75$ cm.

The discharge starts with a transient high density phase that later collapses to a much lower but axially uniform density. The actual dynamics of the early phase of the discharge is quite complex [111, 112]. The final steady state density is approximately uniform along the field. All measurements presented in this Chapter are for the late, steady state phase of the discharge.

Measurements were made over a range of parameters with the static magnetic field varied between 0.0384 T to 0.15 T which spans the lower hybrid (LH) frequency for argon. Several sets of radial electron density and temperature profiles, azimuthally and longitudinally scanned wave magnetic field and antenna radiation resistance measurements were performed. The experimental $n_e(r)$ profiles [111, 112] were then radially symmetrized so as to yield the best match to experimental points and the same volume-averaged density and used in the code. The electron temperature profiles were taken uniform at the level of an average experimentally measured $T_e(r)$. These data were obtained for argon, neon and helium and used for the dispersion and radiation resistance comparison with the code. The parallel wave numbers (k_z) were determined by Fourier analysis of the complex signal (amplitude and phase) from the network analyser [112]. For comparison, the dominant k_z's were taken from the code calculated spectra of the antenna radiation resistance. Since the code does not include the effects of finite electron mass, it is not capable of describing higher than the first – second radial mode for the present experimental conditions.

A curious phenomenon that the density is peaked near 0.0768 T for argon is possibly related to the fact that this is near the LH frequency. Mode transformation between the helicon and the LH wave is in any case not described by the code. However, it will be shown to have no consequence for the agreement between the experimental and the calculated radiation resistances. The rf power (for the double saddle coil) ranged from 1 kW to 10 kW, yet the linear model yielded good agreement with experimental radiation resistance suggesting that nonlinear effects were probably unimportant.

The probe arrays permitted detailed measurements of the azimuthal and axial wave numbers of the helicon waves. The Fourier analysis of experimental data indicated that in both the double saddle coil and helical antenna cases the dominant measured wave mode was the m=+1 azimuthal mode, and also showed the very striking lack of the m=–1. The antenna spectra calculated by the numerical model

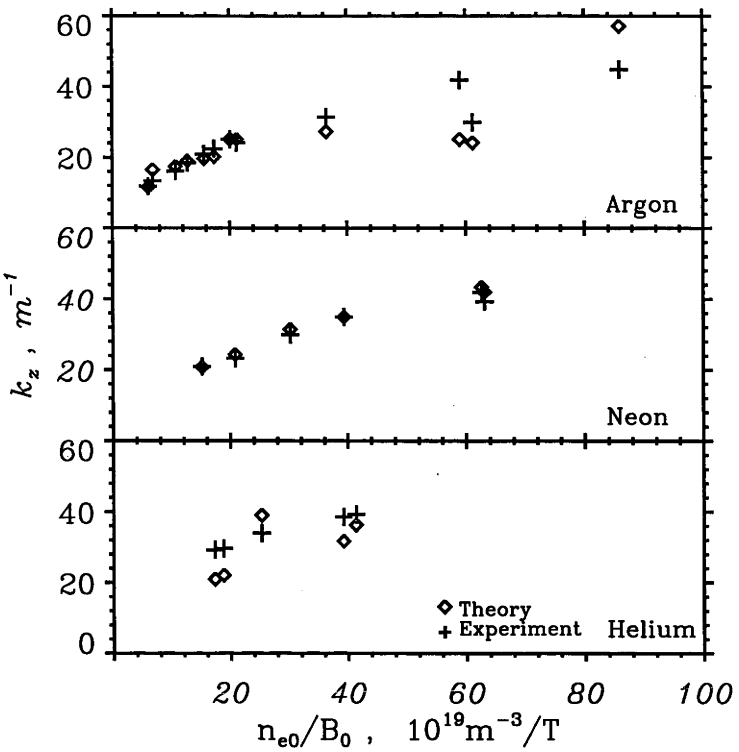

Figure 3.1: Comparison between the experimental and numerical model results of the wave dispersion for argon, neon, and helium for a double saddle coil.

for the measured plasma conditions show a very high radiation resistance for m=+1 compared to all other modes.

The radial magnetic wave field measurements indicated the absence of high order radial modes. All discharges are very similar in the predominance of an m=+1 and first radial mode in the steady state phase of the discharge. These observations are in qualitative agreement with the code.

For the helical antenna, axial measurements of plasma parameters and the wave-field quantities indicate that the plasma density does not extend far on the $m < 0$ side of the antenna; the plasma decays away by 10 cm from the antenna end, while on the other ($m > 0$) side, it reaches the end of the static field. There is a gradual build up in wave amplitude under the antenna.

Figure 3.1 compares the measured wavenumbers with those calculated by the code as a function of the ratio of the central density to magnetic field for the double saddle coil. This choice of independent variable is motivated by the simplified dispersion relation for helicon waves (Eq. (4.20), [33]) which depends uniquely on

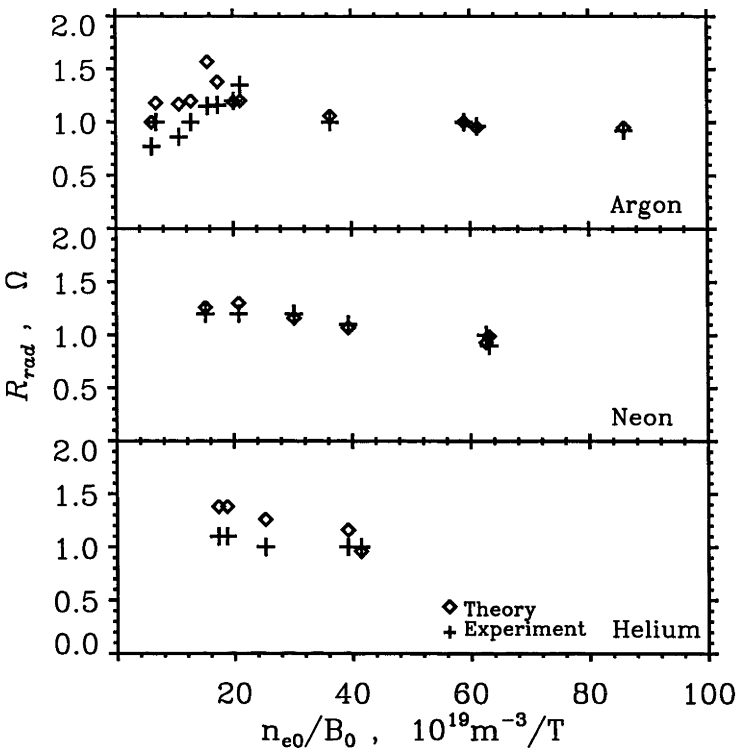

Figure 3.2: Comparison between the experimental and model results of the antenna radiation resistance for argon, neon, and helium for a double saddle coil antenna.

this ratio according to the relation

$$|\mathbf{k}|k_z = \frac{\omega\omega_{pe}^2}{\omega_{ce}c^2} \equiv \frac{4\pi\omega e}{c}\frac{n_e}{B_0} \,. \tag{3.1}$$

This expression is valid for fast waves at frequencies well above the ion cyclotron frequency. Figure 3.1 shows (from top to bottom) results for argon, neon and helium plasmas. The agreement is rather good. The data in Fig. 3.1 cannot be considered a dispersion relation due to the discontinuous effect that the density profiles have on the data. Therefore a theoretical "dispersion relation" cannot be plotted, only the theory points.

If one gets good agreement in the wavenumber predicted by theory, then the antenna radiation resistance comparison should be a reliable way of revealing the presence of parasitic loading. Figure 3.2 shows the comparison of the code calculated and the experimentally measured total antenna radiation resistances. The agreement is also good. These results are not strongly affected by dissipative processes. All that is required is that the wave does not return with significant amplitude to the antenna region after reflection from the ends of the plasma. This was indeed the case in BASIL. One can safely conclude that the helicon wave transports the energy

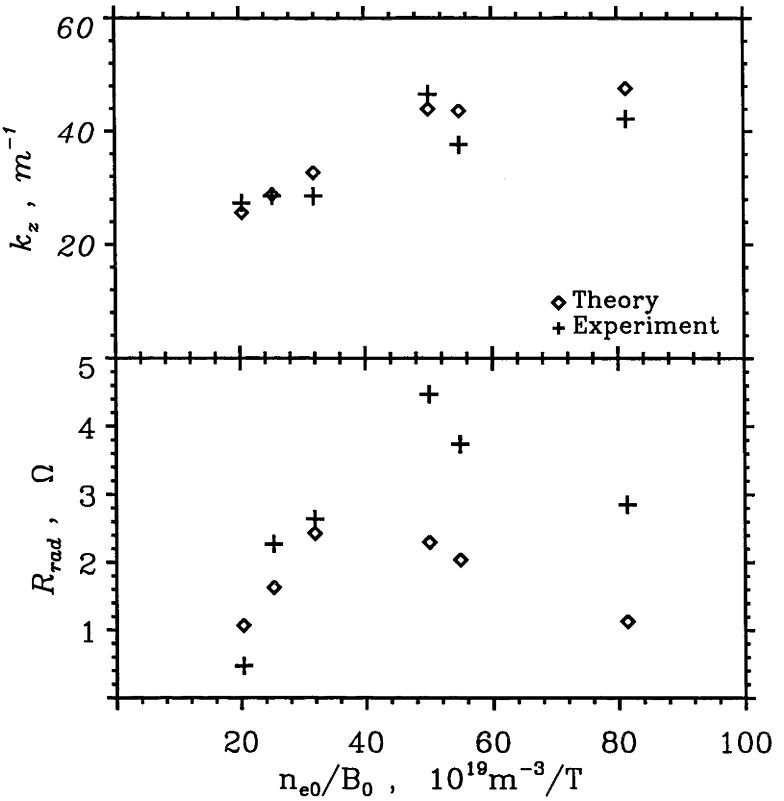

Figure 3.3: Comparison between the experimental and model results of the wave dispersion and antenna radiation resistance in argon plasma for the helical antenna.

launched by the antenna. Somehow this energy is acquired by the plasma. It is beyond the scope of this Chapter to examine this question in detail. It should be pointed out however that the calculations with a new code, UFEM (Chapter 4 and § 5.1), which takes into account the parallel electron dynamics, indicate that it is not obvious that the power deposition is entirely determined by the propagating helicon wave; a significant portion of it may be concentrated at the plasma periphery and near the antenna elements.

The case of the helical antenna is interesting because of the fact that the plasma only forms on one side of the antenna. Figure 3.3 shows the same results for this case. The wavenumber agreement is again quite reasonable, however the high wavenumber selectivity of the helical antenna leads to a lower range of observed wavenumbers even though the same range of fields was used as for the double saddle coil. The antenna radiation resistance agreement is satisfactory except at high densities where the experimental results are higher than theory. This cannot suggest a considerable parasitic loading since the same effect would have been evident in the double saddle coil results. We have been unable to satisfactorily resolve this discrepancy even by use of the UFEM code (Chapter 4), varying the plasma density within the margins

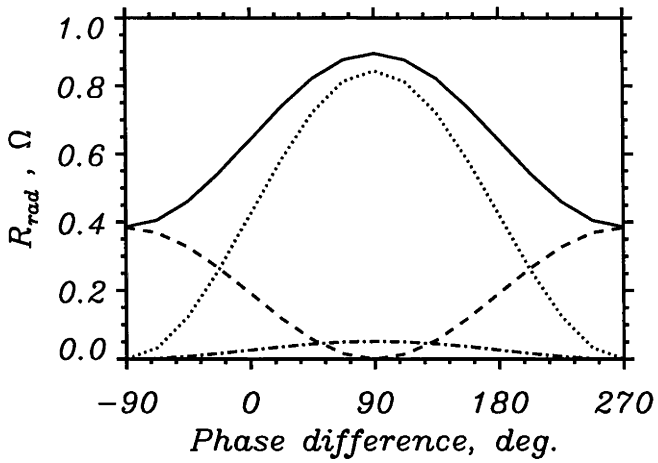

Figure 3.4: The radiation resistance calculated by the numerical model for the phased antenna. Total R_{rad} is shown by the solid line, $R(m{=}{+}1)$ by the dotted line, $R(m{=}{+}3)$ by the dashed line and $R(m{=}{+}5)$ by the dot-dash line.

of possible experimental error and putting a reflector (conducting boundary) on the $m{=}{-}1$ side of the antenna in this code (Appendix A (D)) in order to simulate the absence of plasma density on this side; in terms of wave dispersion and antenna radiation resistance, both codes produced very similar results (§ 5.1), and the virtual absence of the wave field on the $m{=}{-}1$ side of the antenna made the wave reflection unimportant. However, radiation resistances $3 - 4\ \Omega$ were found numerically when the density was taken $\approx 30\%$ larger than measured experimentally for those cases. This enables us to suspect the existence of considerable systematic error in the measurements of n_e at high densities and magnetic fields.

In theory, the radiation resistance can be considered as a product of two factors. First is the spectrum of the plasma response which can be calculated with the "flat" antenna current spectrum. Second is the square of the antenna current (m,k_z)-spectrum. For the helical antenna, the effect of the plasma density on R_{rad} can be more pronounced than for the double saddle coil since the antenna current k_z-spectrum of $(3/2)\lambda$ helical antenna (Appendix B (D), [111]) is much more selective to specific k_z's, and hence, the R_{rad} is more sensitive to the plasma response, especially for conditions when k_z corresponding to the maximum in the antenna current spectrum is close to the k_z corresponding to the strong $\{m{=}{+}1,\ N_r{=}1\}$ mode (which was really the case in the above computations).

To the best of the author's knowledge, this is the first comparison of the helicon wave dispersion and antenna radiation resistance in a high density and field source that is free of adjustable parameters. A similar detailed comparison of the dispersion relation has been performed by Davies and Christiansen [47] for the case of a low density ($n_e < 5 \times 10^{17}$ m^{-3}) and low field ($B_0 < 0.04$ T) preformed plasma. According to these authors, the effects of finite electron mass cannot be neglected

for prediction of the dispersion relation as they could in our case. This conclusion appears to agree with more recent work [37, 114].

In several attempts to launch an m=–1 mode, a pair of phased double saddle coils was used in the plasma pre-formed by another double saddle coil antenna driven at 7.1 MHz (since the phased coils were unable to maintain the discharge over the full range of phase difference, [111]). The dependence of the radiation resistance on the phase difference between the coils shown in Fig. 3.4 is entirely governed by the factor $i + e^{i\varphi}\sin(m\pi/2)$, where φ is the phase difference, in the antenna current spectrum (Appendix B (C)). A qualitatively similar variation of the relative amplitudes of azimuthal wave numbers was observed in the experiment [111]. At $\varphi = -90^0$, when the m=+1 mode was absent in the spectrum, a strong m=+3 mode was observed instead of m=–1. The numerical model demonstrated a negligible $R(m$=–1). In the experiment, the amplitude of m=–1 was negligible.

Chapter 4

Kinetic Plasma Model

4.1 Warm Plasma Dielectric Tensor

The MHD numerical model described in Chapter 2 is limited to the description of a cold dense plasma in which E_z can be disregarded and the wave dissipation is dominated by collisions. As mentioned in § 2.2, there are several important phenomena of interest which cannot be described using the plasma dielectric tensor (2.1), such as the wave resonances in warm plasma, the excitation of specific warm plasma wave modes, the mode conversion and the kinetic wave damping due to the wave–particle interaction when the wave phase velocity, ω/k, is of the same order as the particle thermal velocity (such as the Landau damping). Here we consider them in more detail.

Starting from the linearized Vlasov equation with the collisional term in the particle conserving model [11],

$$\frac{\partial f_1}{\partial t} + \mathbf{v}\cdot\frac{\partial f_1}{\partial \mathbf{r}} + (\mathbf{v}\times\overline{\omega}_c)\cdot\frac{\partial f_1}{\partial \mathbf{v}} + \frac{q}{m}(\mathbf{E}_1 + \mathbf{v}\times\mathbf{B}_1)\cdot\frac{\partial f_0}{\partial \mathbf{v}} = \nu(\frac{n_1}{n_0}f_0 - f_1)\ , \tag{4.1}$$

where f is the distribution function, n is the density, ν is the collision frequency, ω_c is the cyclotron frequency for specific particles (electrons or ions), the subscript 1 indicates perturbed quantities and 0 — the equilibrium quantities (f_0 is the Maxwellian distribution), the following form of the plasma dielectric tensor can be derived [99]:

$$\underline{\varepsilon} = \begin{pmatrix} \varepsilon_1 & i\varepsilon_2 & 0 \\ -i\varepsilon_2 & \varepsilon_1 & 0 \\ 0 & 0 & \varepsilon_3 \end{pmatrix}\ ,$$

$$\varepsilon_1 = 1 + \sum_\alpha \frac{\omega_{p\alpha}^2}{2\omega|k_z|v_{T\alpha}}\left[Z(\zeta_{-1}^\alpha) + Z(\zeta_1^\alpha)\right]\ ,$$

$$\varepsilon_2 = \sum_\alpha \frac{\omega_{p\alpha}^2}{2\omega|k_z|v_{T\alpha}}\left[Z(\zeta_{-1}^\alpha) - Z(\zeta_1^\alpha)\right]\ ,$$

$$\varepsilon_3 = 1 - \sum_\alpha \frac{\omega_{p\alpha}^2 Z'(\zeta_0^\alpha)}{k_z^2 v_{T\alpha}^2 + i\nu_\alpha |k_z| v_{T\alpha} Z(\zeta_0^\alpha)} , \tag{4.2}$$

where $\zeta_n^\alpha = (\omega + i\nu_\alpha + n\omega_{c\alpha})/|k_z|v_{T\alpha}$, $v_{T\alpha} = \sqrt{2T_\alpha/m_\alpha}$ is the particle thermal velocity, the summation is over all charged particles (electrons and ions), $\omega_{c\alpha}$ accounts for the charge sign. Z is the well known plasma dispersion function [59],

$$\begin{aligned} Z(\zeta) &= \frac{1}{\sqrt{\pi}} \int_{-\infty}^{\infty} \frac{e^{-x^2}}{x-\zeta} dx, \qquad Im(\zeta) > 0 , \\ Z'(\zeta) &= -2[1 + \zeta Z(\zeta)] , \end{aligned} \tag{4.3}$$

which can also be expressed through the tabulated [1] complex error function,

$$\begin{aligned} Z(\zeta) &= i\sqrt{\pi} e^{-\zeta^2} [\mathrm{sgn}(k_z) + \mathrm{erf}(i\zeta)] , \\ \mathrm{erf}(z) &= \frac{2}{\sqrt{\pi}} \int_0^z e^{-t^2} dt . \end{aligned} \tag{4.4}$$

Note that, unlike in the original work of Fried and Conte [59], the plasma dispersion function defined as above satisfies the symmetry requirement

$$Z(\zeta) = \begin{cases} Z(\zeta), & k_z > 0 \\ -Z(-\zeta), & k_z < 0 \end{cases} \tag{4.5}$$

derived by Stix [123] on the basis of the causality principle.

In the MHD limit, $\zeta \gg 1$,

$$Z(\zeta) \approx -\frac{1}{\zeta} - \frac{1}{2\zeta^3} \cdots , \tag{4.6}$$

and the tensor (4.2) reduces to (2.1) with

$$\varepsilon_3 = 1 - \sum_i \frac{\omega_{pi}^2}{\omega(\omega + i\nu_i)} - \frac{\omega_{pe}^2}{\omega(\omega + i\nu_e)} . \tag{4.7}$$

The assumptions made in the derivation of the tensor (4.2) are that the particle Larmor radius, ρ, is small compared to the scale length of the wave field variation, l (typically a wavelength),

$$\rho/l \ll 1 , \tag{4.8}$$

and the wave frequency is not close to the harmonics of the particle gyro-frequencies,

$$\omega \not\approx N\omega_c, \qquad N = 2,\ 3,\ \ldots , \tag{4.9}$$

where the additional wave type (electron or ion Bernstein waves) can appear.

The treatment of wave behavior near the ion cyclotron harmonics and ion–ion hybrid resonances requires a higher order expansion in finite Larmor radius (FLR) and leads to higher order differential equations [7, 28, 42, 44, 128, 133] (the dielectric

tensor becomes a differential operator). In general, this procedure consists of the replacement of $\mathbf{k}_\perp$ in the homogeneous hot plasma dielectric tensor expanded up to the second order in $k_\perp \rho$ by $-i\partial/\partial \mathbf{r}_\perp$, where this replacement is unambiguous (and discarding the terms where it cannot be done unambiguously, which makes the whole procedure a bit dubious), so as to satisfy energy conservation. A significant simplification can be achieved by the use of the "reduced order" form of the dielectric tensor [120, 136] which describes only the fast magnetosonic wave (FMW) but properly accounts for the mode-converted energy through the FMW dissipation, and so eliminates problems related to the numerical resolution of the short-wavelength ion Bernstein waves. This is of interest, primarily, for the ion-cyclotron resonance heating (ICRH) scenarios in numerous fusion-oriented devices [61] and usually requires at least 2D numerical schemes for proper modelling. However, in the helicon wave frequency range, $\omega_{ci} \ll \omega \ll \omega_{ce}$, the FLR effects are often not important.

The collision frequencies which we employ in tensor (4.2) include the electron–ion and ion–electron collisions [29, 69],

$$\nu_{ei} \approx 3 \cdot 10^{-6} \alpha Z_i^2 f_i \ , \qquad \nu_{ie} \approx 5 \cdot 10^{-8} \alpha \frac{Z_i^2}{\sqrt{M_i}} \ , \tag{4.10}$$

where

$$\alpha = \frac{n_e}{T_e^{3/2}} \left[23 + \ln \left(\frac{T_e^{3/2}}{\sqrt{n_e}} \right) \right] \ , \tag{4.11}$$

as well as the collisions between different ion species, which can be important in multi-species plasmas (or with different states of ionization of the same ion),

$$\nu_{ii'} \approx 7 \cdot 10^{-8} Z_i^2 Z_{i'}^2 \frac{\sqrt{M_{i'}}}{M_i} \left(1 + \frac{M_{i'}}{M_i} \right) \frac{n_e f_{i'}}{T_{i'}^{3/2}} \Lambda_{ii'} \ , \tag{4.12}$$

$$\Lambda_{ii'} = 23 - \ln \left[\frac{Z_i Z_{i'} (M_i + M_{i'})}{M_i T_{i'} + M_{i'} T_i} \sqrt{\left(\frac{f_i Z_i^2}{T_i} + \frac{f_{i'} Z_{i'}^2}{T_{i'}} \right) n_e} \right] \ . \tag{4.13}$$

In Eqs. (4.10) — (4.13) n_e is in cm^{-3}, T is in eV, the ion mass, M_i, is in atomic units, Z_i is the ion charge and $f_i = n_i/n_e$.

For *helicon plasma sources*, we often must also take into account the electron–neutral collisions, $\nu_{en} = n_n \sigma_{en} v_{Te}/\sqrt{2}$, the typical cross-section, $\sigma_{en} \sim 5 \times 10^{-15}$ cm^{-2}. Also, since the plasma in this case is usually confined within a non-conducting (glass) tube, the electron–wall collisions can provide a significant wave dissipation mechanism at the plasma edge. Supposing that electrons are magnetized and their perpendicular energy distribution is Maxwellian near the wall, the electron–wall collision frequency can be evaluated as

$$\nu_{e/wall} = \frac{2\omega_{ce}}{\sqrt{\pi}} \int\limits_{x/\rho_e}^{\infty} \frac{e^{-t^2} dt}{\frac{\pi}{2} + \arcsin \left(\frac{x}{\rho_e t} \right)} \ , \tag{4.14}$$

where ρ_e is the electron gyro-radius and x is the distance to the wall. At distances $x \leq 3\rho_e$, where the electron–wall collision frequency is not very small, Eq. (4.14) can be very accurately approximated by the formula

$$\nu_{e/wall} \approx \frac{2\omega_{ce}}{\pi} \exp\left(-2.3\frac{x}{\rho_e}\right) . \tag{4.15}$$

4.2 Overview of the Wave Types Described by the Model

In this Section we present a brief overview of the wave phenomena which can be expected from the numerical model with plasma described by the dielectric tensor (4.2). We will omit the ion–cyclotron frequency range where the physical situation is complicated. We do not intend to present a careful and comprehensive analysis of plasma waves here, which is far beyond the scope of this thesis; we will rather confine ourselves to introduce the terminology adopted in the RF community.

The Maxwell's equations in the absence of external currents are given by

$$\nabla \times \nabla \times \mathbf{E} - \underline{\bar{\varepsilon}}\mathbf{E} = 0 , \tag{4.16}$$

where we use the dimensional form of the dielectric tensor (4.2), $\bar{\varepsilon} = k_0^2\varepsilon$, $k_0 = \omega/c$. In a uniform plasma we obtain non-trivial solutions, $\mathbf{E} \not\equiv 0$, for the plane wave of the form $\sim \exp\{i(\mathbf{k}_\perp \cdot \mathbf{r}_\perp + k_z z)\}$ only if

$$\bar{\varepsilon}_1 k_\perp^4 - Bk_\perp^2 + C = 0, \tag{4.17}$$

where

$$\begin{aligned} B &= (\bar{\varepsilon}_1 - k_z^2)(\bar{\varepsilon}_1 + \bar{\varepsilon}_3) - \bar{\varepsilon}_2^2, \\ C &= \bar{\varepsilon}_3[(\bar{\varepsilon}_1 - k_z^2)^2 - \bar{\varepsilon}_2^2] . \end{aligned}$$

Equation (4.17) is the wave dispersion relation expressed with respect to $k_\perp$ (the wave vector perpendicular to the external magnetic field, B_0). Two wave branches result from Eq. (4.17) which are conventionally termed the *fast wave* (FW) (with smaller $k_\perp$ and, hence, larger phase velocity, $\omega/k_\perp$), and the *slow wave* (SW) (with larger $k_\perp$). Resonances occur when $k_\perp$ approaches ∞. In the present model this is the case when $\varepsilon_1 \to 0$ leading to the lower and upper hybrid resonances. In the vicinity of a resonance, the above plasma waves are expected to undergo mode conversion to a hot plasma slow mode not described in the present simplified model [127]. Near a resonance, the wavelengths of different wave branches may become comparable, and the wave energy can be transferred from one wave branch to another. The latter phenomenon is known as *mode conversion*. Even if only one wave

branch (typically the FW) is directly excited by an antenna, the wave of another type may originate in the plasma due to mode conversion.

For frequencies in the **Alfvén range**, $\omega < \omega_{ci}$ ($\omega \not\ll \omega_{ci}$), the fast wave is usually evanescent in the low density edge plasma, and there are two types of slow wave described by the present model, known as the *kinetic Alfvén wave* (KAW) and the *surface quasi-electrostatic wave* (SQEW), respectively. The former occurs if $\beta \gg m_e/M_i$ and the latter if $\beta \ll m_e/M_i$, where β is the ratio of plasma kinetic to magnetic pressure. Since the SQEW subsists at low β, it propagates in the boundary of a fusion plasma whence its name.

The dispersion relation and the damping rate for the KAW in a uniform plasma are given by [133]

$$\begin{aligned} \omega^2 &= c_A^2 k_z^2 \left[1 + k_\perp^2 \rho_i^2 \left(\frac{3}{4} + \frac{T_e}{T_i}\right)\right] , \\ \gamma &= \sqrt{\frac{\pi}{8}\frac{m_e}{m_i}} \frac{k_\perp^2 c_A^2}{\omega_{ci}^2} |k_z| c_s , \end{aligned}$$

where

$$c_A = \frac{B_0}{\sqrt{4\pi \sum_\alpha n_\alpha m_\alpha}}$$

is the Alfvén speed, and $c_s = \sqrt{T_e/m_i}$ is the ion sound speed.

The SQEW has the following uniform plasma dispersion [133]:

$$\omega^2 = \frac{c_A^2 k_z^2}{1 + k_\perp^2 c^2/\omega_{pe}^2} .$$

It is a *backward wave*, i. e. its phase and group velocity are opposite to each other.

It can be seen from these dispersion relations that the KAW propagates on the high density side of the Alfvén resonance layer and the SQEW on the low density side. In the MHD limit, ($\omega \ll \omega_{ci}$, $E_z = 0$, $\rho_i = 0$), these waves become the *shear Alfvén wave*, it propagates along $\mathbf{B_0}$ and has a simple dispersion,

$$\omega^2 = c_A^2 k_z^2 . \tag{4.18}$$

The spatial location in the plasma where the condition (4.18) (or, more precisely, $k_z^2 = \bar{\varepsilon}_1$) is satisfied is called the *Alfvén resonance* (A-resonance) layer. Strictly speaking, this is not a resonance in the present plasma model. In the latter case, the Alfvén resonance is resolved by mode conversion of the FW to either the KAW or the SQEW depending on the local value of the plasma β. The SQEW can also be excited directly by the antenna. It undergoes cutoff near the Alfvén resonance layer where $k_\perp$ approaches zero [13].

In the **helicon wave frequency range**, $\omega_{ci} \ll \omega \sim \omega_{LHR} = \sqrt{\omega_{ce}\omega_{ci}}$, typical for the high density, high magnetic field helicon plasma sources, the FW is known

as the *helicon* wave. (In the ion cyclotron frequency range it becomes the *fast magnetosonic wave* (FMW).) The E_z component of the FW electric field can often be neglected, and the most general dispersion relation resulting from Eq. (4.17) for the FW is

$$k_\perp^2 = \bar{\varepsilon}_1 - k_z^2 - \frac{\bar{\varepsilon}_2^2}{\bar{\varepsilon}_1 - k_z^2} \,. \tag{4.19}$$

For $\omega_{ci} \ll \omega \ll \omega_{ce}$ Eq. (4.19) can be further reduced to

$$\omega = \frac{\omega_{ce} c^2 k k_z}{\omega_{pe}^2} \,, \tag{4.20}$$

(where k is the modulus of the wave vector) which is the well-known helicon wave dispersion relation [3]. Commonly, this wave branch is very robust. It can be efficiently excited by an antenna, and its dissipation in the plasma is small. The particle thermal motion only slightly modifies its dispersion, compared to the cold plasma approximation. Often, this is the only propagating mode, the bulk of the plasma is nontransparent for the SW for frequencies below ω_{LHR}. If, however, the plasma density drops to a sufficiently low value at the edge, the peripheral plasma can become transparent for the SW for densities up to the location of the *lower hybrid resonance* (LHR) followed by the SW cutoff (which originates due to the finite wave damping in the model). For the conditions of high density helicon sources, this resonance–cutoff pair is commonly located in a very thin edge layer; the SW does not develop any propagating wave structure and manifests itself as a narrow "spike" in the radial electric field at the plasma edge.

The condition for the LHR, $\varepsilon_1 = 0$, in the uniform cold collisionless plasma can be written as

$$1 + \frac{\omega_{pe}^2}{\omega_{ce}^2} - \frac{\omega_{pi}^2}{\omega^2} = 0 \,. \tag{4.21}$$

The wave collisional dissipation and particle thermal motion slightly modify the above condition (but not strongly [3, 127]). This relation shows that the location of the LHR is almost independent of $\mathbf{k}$ and, for a given frequency and magnetic field, is determined only by the density.

If the operational parameters are chosen so that the LHR is deep inside the plasma (such as those employed in the lower hybrid heating (LHH) schemes, [61]), the SW, which is known as the *lower hybrid wave* (LHW) in this case, can propagate between the plasma edge and the LHR. Its dispersion is given approximately [127] by

$$k_\perp^2 \simeq \frac{k_z^2 \omega_{pe}^2 \omega_{ce}^2}{(\omega_{pe}^2 + \omega_{ce}^2)(\omega^2 - \omega_\infty^2)} \,,$$

where

$$\omega_\infty^2 = \frac{\omega_{ce}\omega_{ci}}{1 + \omega_{ce}^2/\omega_{pe}^2} \approx \omega_{ci}\omega_{ce} \equiv \omega_{LHR}^2 \,.$$

This wave is quasi-electrostatic ($|E_r| \gg |E_\theta|,\ |E_z|, \quad |k_\perp| \gg |k_z|$) and *backward propagating*.

For frequencies **well above the LHR frequency**, $\omega_{LHR} \ll \omega \ll \omega_{ce}$, as is the case for typical low density, low magnetic field helicon plasma source, $\omega \lesssim 0.1\omega_{ce}$, $\omega_{pe} > 10\omega_{ce}$, the SW is often referred to as the *Trivelpiece–Gould (TG) mode* or TG wave [113, 131]. For $\omega_{pe} \gg \omega_{ce}$ its dispersion can be approximated [113] by the following simple formula:

$$\omega = \omega_{ce}\frac{k_z}{k} - i\nu_e \ . \tag{4.22}$$

Like the LH wave, the TG wave is quasi-electrostatic and backward propagating. In helicon plasma sources these waves are usually strongly damped by collisions and deposit their energy in a narrow surface layer of the plasma column. In fact, helicon and TG waves belong to the same wave branch: depending on the direction of the wave propagation with respect to the magnetic field, the helicon mode can become the TG mode and vice versa [15]. Note that under these conditions, the LHR is not present in the plasma (so that LH heating is not possible) and nor there is any mode conversion of the TG mode [15]. (From this point of view, we would disagree with Shamrai and Taranov [113, 114] that the TG wave is generated by the linear mode conversion of the helicon wave at the plasma edge; we would rather say that it is directly excited by the antenna.)

4.3 Numerical Scheme

In this Section we present the theoretical foundations of the finite element numerical algorithm which allows us to obtain pollution-free solutions of Maxwell's equations with the plasma dielectric tensor (4.2).

In the MHD model of Chapter 2 it was possible to formulate the differential equations with respect to only one field component. Dealing with a dielectric tensor like (4.2), we are, in practice, forced to formulate the differential equations using several field components. This immediately brings up the question whether the finite element scheme employed is affected by numerical pollution. The *numerical* or *spectral pollution* is the production of unphysical, "fake" modes which commonly appear when certain resonance conditions for the wave exist, and if the discretization scheme is constructed without proper account for this phenomenon. It often presents a formidable problem for algorithms based on the finite element method, since the "polluted" modes cannot be eliminated by higher precision or better numerical resolution, and there is often no way of separating them from the real physical solutions but to check the model against another code which does not exhibit the problem (if such a code is available). The numerical pollution was carefully analyzed in [6, 62, 138, 139]. In the presence of resonances in plasma, different

wavefield components (and/or their derivatives) usually exhibit different types of singular behavior which must be reproduced by the discretization scheme, otherwise the pollution occurs. The heuristic rule to detect a potentially polluted scheme has been formulated in [62]. It states that at the resonance, where some of the terms in the equations vanish, their discretized form should be satisfied over the entire length of a finite element. If they can be satisfied only at one point per interval, the numerical scheme tends to produce a polluted solution (§ 1.2.3 and Fig. 1.14 in [62]). In the framework of this methodology, it has been suggested to use the so-called hybrid finite elements, i. e. different sets of finite element basis functions for different field components (and their derivatives) which are also often set on different meshes. This technique was successfully realized in several codes [5, 63, 136, 138]. It has, however, some disadvantages:

- If we want to construct a code operable in a broad range of frequencies and plasma parameters, we may discover that the hybrid finite element discretization suitable for a resonance of one type (say, for the Alfvén resonance) fails for the resonance of another type (say, for the LHR). Moreover, different discretizations in the plasma and the vacuum may be required to avoid pollution.

- The hybrid elements of the lowest order (piecewise-linear and piecewise-constant) often show a rather slow convergence rate in a warm plasma, while the hybrid elements of higher orders [62] are difficult to program.

Another approach, which is in principle applicable in 1D, is to use the so-called "penalty method" [88, 96, 104, 109, 141]. It consists in the addition of an extra term, $\eta\nabla(\nabla\cdot\mathbf{E})$, where η is the penalty factor, to the Maxwell's equations in terms of electric field,

$$\nabla\times\nabla\times\mathbf{E}-\underline{\underline{\varepsilon}}\mathbf{E}=\frac{4\pi i\omega}{c^2}\mathbf{j}_{ext}\ . \tag{4.23}$$

Above a certain threshold of η this may shift the parasitic modes out of the desired region of the spectrum, but simultaneously brings up the question about the distortion of the plasma response [104].

As pointed out in [10], the commonly used discretization of Eq. (4.23) is actually disadvantageous, since the term $\nabla\times\nabla\times\mathbf{E}$ is the very source of the pollution. The discretized form of the operator $\nabla\times$ has a large null space which not only contributes to the system poor condition and the pollution problem, but, at least in more than 1D, often requires one to use sophisticated programming techniques (such as the compact pointer storage method, [136]) for matrix storage and inversion to fit the computer memory. As a possible remedy, it was first suggested in [10] to use the vector and scalar potentials, $(\mathbf{A},\,\phi)$, so that

$$\mathbf{B}=\nabla\times\mathbf{A}\ ,\qquad \mathbf{E}=-\nabla\phi+ik_0\mathbf{A}\ , \tag{4.24}$$

with the Coulomb gauge

$$\nabla \cdot \mathbf{A} = 0 \ . \tag{4.25}$$

Using the potentials (4.24), (4.25), Maxwell's equations can be re-written in the form

$$\begin{cases} \nabla^2 \mathbf{A} + k_0^2 \underline{\varepsilon} \cdot \mathbf{A} + i k_0 \underline{\varepsilon} \cdot \nabla \phi = -\dfrac{4\pi}{c} \mathbf{j}_{ext} \\ \\ \nabla \cdot (\underline{\varepsilon} \cdot \nabla \phi) - i k_0 \nabla \cdot (\underline{\varepsilon} \cdot \mathbf{A}) = -4\pi \rho_{ext} \ , \end{cases} \tag{4.26}$$

where $\mathbf{j}_{ext}$ and ρ_{ext} are the current and charge density of an external source. If we take the divergence of the first equation of (4.26) and use the charge continuity, $i\omega\rho_{ext} = \nabla \cdot \mathbf{j}_{ext}$, the system (4.26) gives

$$\nabla^2 (\nabla \cdot \mathbf{A}) = 0 \ . \tag{4.27}$$

This demonstrates that if the Coulomb gauge condition, Eq. (4.25), is imposed on the domain boundaries, it propagates throughout the whole domain due to the Laplacian structure of Eqs. (4.26).

The *finite difference* discretization of Eqs. (4.26) was employed in the code ORION [10]. In [10] it was also demonstrated that this method eliminates the pollution, provided that the numerical algorithm is capable of maintaining the gauge condition (4.25). The variational form for the *finite element* discretization of Eqs. (4.26) has been found in [73, 74].

The *boundary conditions* on a cylindrical perfectly conducting wall for the potentials (4.24) are

$$A_\theta = 0 \ , \qquad A_z = 0 \ , \qquad \phi = 0 \ . \tag{4.28}$$

We explicitly impose them as the *essential* conditions [62] on the functional space of $(\mathbf{A}, \phi)$.

To obtain the weak (Galerkin) variational form necessary to solve Eqs. (4.26) by the finite element method, we multiply the first equation of (4.26) by an arbitrary test vector $\mathbf{F}^*$ and the second equation by the test scalar function G^* and integrate them over the system volume V. The test 4-vector $(\mathbf{F}, G)$ must belong to the same functional space as $(\mathbf{A}, \phi)$. Using the vector identity

$$\nabla^2 \mathbf{A} = \nabla(\nabla \cdot \mathbf{A}) - \nabla \times \nabla \times \mathbf{A} \ ,$$

the final expression for the variational form can be obtained as a system of two

coupled equations,

$$\begin{cases} \int\limits_V [(\nabla \times \mathbf{F}^*) \cdot (\nabla \times \mathbf{A}) + (\nabla \cdot \mathbf{F}^*)(\nabla \cdot \mathbf{A}) - \mathbf{F}^* \cdot \mathbf{C}]\, dV \\ \qquad\qquad = \dfrac{4\pi}{c} \int\limits_V (\mathbf{F}^* \cdot \mathbf{j}_{ext}) dV \\ \int\limits_V (\nabla G^* \cdot \mathbf{C}) dV = 4\pi i k_0 \int\limits_V G^* \rho_{ext} dV \ , \end{cases} \tag{4.29}$$

where

$$\mathbf{C} = \underline{\overline{\varepsilon}} \cdot (\mathbf{A} + i\nabla\varphi) \ ,$$

and where, for the sake of simplicity, we use the dimensional tensor $\overline{\underline{\varepsilon}} = k_0^2 \underline{\varepsilon}$ and the normalized scalar potential, $\varphi = \phi / k_0$.

In the derivation of Eqs. (4.29), the surface terms

$$\int\limits_S d\mathbf{S} \cdot (\mathbf{F}^* \times \nabla \times \mathbf{A}) \qquad \text{and} \qquad \int\limits_S d\mathbf{S} \cdot (G^* \cdot \mathbf{C})$$

(integration is over the conducting boundary S) have been dropped because ($\mathbf{F}$, G) must satisfy the same boundary conditions, Eqs. (4.28), as ($\mathbf{A}$, ϕ) (since it belongs to the same functional space). The term

$$\int\limits_S d\mathbf{S} \cdot \mathbf{F}^* (\nabla \cdot \mathbf{A}) \tag{4.30}$$

has been canceled to impose the gauge condition, Eq. (4.25), on the domain boundaries. Simultaneous cancellation of another term analogous to (4.30) at $r \to 0$, in principle, allows the fields to acquire a weak logarithmic ($\sim \log(r)$) singularity on the axis [73, 74]. However, we will further see that in 1D cylindrical geometry we have to impose additional constraints on the functional space of ($\mathbf{A}$, ϕ) at $r \to 0$. For any azimuthal mode number m, at least two components of ($\mathbf{A}$, ϕ) must be zero on the axis, which automatically eliminates the singularity of this type.

The remarkable feature of the variational form (4.29) is that it keeps the term with $\nabla \cdot \mathbf{A}$. In fact, this is the very term which eliminates the pollution. As mentioned before, the variational form based on Eqs. (4.26) with the condition (4.25) imposed on the domain boundaries must maintain this condition everywhere. It has been demonstrated in [73, 74, 75] that polluted modes usually do not obey the Coulomb gauge condition (at least, it seems to be highly improbable that such unphysical modes can satisfy this condition in the entire volume). Thus, the variational form (4.29) eliminates polluted modes together with $\nabla \cdot \mathbf{A}$. The accuracy with which the numerical algorithm can keep $\nabla \cdot \mathbf{A} = 0$ indicates the "accuracy" with which the solution is pollution-free. Strictly speaking, it has been rigorously proven that

this approach is pollution-free only for a vacuum, where the comparison between numerical and analytical solutions has been performed [73, 75]. On the other hand, the code PENN [73, 74] based on this scheme has been extensively benchmarked against several other codes, and the evidence for the absence of numerical pollution given in [73, 74] for hot plasma is very convincing. In § 4.6 we will also present the benchmarking results for our code which confirm this assumption.

To proceed further, it is necessary to determine the field behavior on the axis, $r \to 0$. A simple analysis of Maxwell's equations with the dominating terms $\sim 1/r$ shows that the solution regular on the axis must behave asymptotically at $r \to 0$ as

$$\begin{aligned} \{A_r, A_\theta, E_r, E_\theta, B_r, B_\theta\} &\sim r^{|m|-1} , \\ \{A_z, \phi, E_z, B_z\} &\sim r^{|m|} , \quad \text{for} \quad m \neq 0 , \end{aligned} \tag{4.31}$$

and

$$\begin{aligned} \{A_r, A_\theta, E_r, E_\theta, B_r, B_\theta\} &\sim r , \\ \{A_z, \phi, E_z, B_z\} &\sim const , \quad \text{for} \quad m = 0 , \end{aligned} \tag{4.32}$$

where m is the azimuthal mode number. (The analysis is analogous to that presented in [138]. Since at $r \to 0$ we can consider the plasma parameters constant, the reader can also refer to [127] (§ 5.5.2) where the analytic solutions for the fields in a uniform plasma cylinder with the tensor (4.2) were obtained.) This form of asymptotic behavior is general and is valid regardless of the plasma. Equations (4.31), (4.32) show that among the components of ($\mathbf{A}$, ϕ) only (A_r, A_θ) for $|m| = 1$ and (A_z, ϕ) for $m = 0$ are non-zero ($\sim const$) on the axis.

For the finite element discretization of Eqs. (4.29) we use the same set of "hat" basis functions as in Chapter 2, Eq. (2.11) and Fig. 2.1, with the addition of 0'th and N'th elements,

$$e_0(r) = \begin{cases} (r_1 - r)/r_1 & \text{if} \quad 0 \le r \le r_1 \\ 0 & \text{elsewhere} \end{cases} ,$$

$$e_N(r) = \begin{cases} (r - r_{N-1})/(r_N - r_{N-1}) & \text{if} \quad r_{N-1} < r \le r_N \\ 0 & \text{elsewhere} \end{cases} ,$$

$r_0 = 0$, $r_N = b$ (the conducting boundary). Another option would be the use of cubic Hermite elements as in [7, 74], which exhibit better convergence rate in warm plasma. However, the gain in terms of computational speed and computer memory with the use of cubic elements is 2 — 4 compared to the linear ones [73], while the amount of analytic and programming work in this case is at least 10 times larger. For a 1D model, limited computer resources are nowadays not a large problem. In addition, for an accuracy of 2 — 3 % the "efficiencies" of both schemes are comparable [73].

To obtain a linear system from the variational form (4.29), we

- take one Fourier-harmonic of the potentials, $(\mathbf{A},\,\phi)$, $(\mathbf{F},\,\mathrm{G})$ $\sim \exp\{i(m\theta + k_z z)\}$; this leaves only the radial derivatives and integration over r in Eqs. (4.29),

- represent the approximate form of potentials $(\mathbf{A},\,\phi)$ through the finite element basis functions,

$$\{A_r, A_\theta, A_z, \phi\}(r) = \sum_{i=0}^{N} \{A_{r(i)}, A_{\theta(i)}, A_{z(i)}, \phi_{(i)}\} e_i(r) \ , \tag{4.33}$$

  where the coefficients $\{A_{r(i)}, A_{\theta(i)}, A_{z(i)}, \phi_{(i)}\}$ are to be found, and

- run the test 4-vector $(\mathbf{F},\,\mathrm{G})$ through the basis set,

$$\begin{aligned}(F_r, F_\theta, F_z, G) = (e_0,0,0,0), \quad (0,e_0,0,0), \quad (0,0,e_0,0), \quad \dots \\ \dots \quad (0,0,e_i,0), \quad \dots \quad \dots \quad (0,0,0,e_N) \ .\end{aligned}$$

We finally arrive at the following linear system, Eqs. (4.34) — (4.37), with the $(4N-3)^2$, 15-diagonal band matrix (although a bit cumbersome, we reproduce it here since it is needed for the remaining analysis):

$$\begin{aligned}
& A_{r(i-1)}K_{1r(i-1)} + A_{r(i)}S_{1r(i)} + A_{r(i+1)}K_{1r(i)} \\
+ \ & A_{\theta(i-1)}K_{1\theta(i-1)} + A_{\theta(i)}S_{1\theta(i)} + A_{\theta(i+1)}K_{1\theta(i)} \\
- \ & i\varphi_{(i-1)} \left\{ p_{i-1} + \int\limits_{r_{i-1}}^{r_i} \overline{\varepsilon}_1 e_i e_i' r dr \right\} + \varphi_{(i)} S_{1\varphi(i)} \\
- \ & i\varphi_{(i+1)} \left\{ p_i + \int\limits_{r_i}^{r_{i+1}} \overline{\varepsilon}_1 e_i e_i' r dr \right\} = -\frac{4\pi}{c} \int\limits_{r_{i-1}}^{r_{i+1}} j_r e_i r dr \ ,
\end{aligned} \tag{4.34}$$

$$\begin{aligned}
- \ & A_{r(i-1)}K_{1\theta(i-1)} - A_{r(i)}S_{1\theta(i)} - A_{r(i+1)}K_{1\theta(i)} \\
+ \ & A_{\theta(i-1)}K_{1r(i-1)} + A_{\theta(i)}S_{1r(i)} + A_{\theta(i+1)}K_{1r(i)} \\
- \ & \varphi_{(i-1)} \left\{ q_{i-1} + \int\limits_{r_{i-1}}^{r_i} \overline{\varepsilon}_2 e_i e_i' r dr \right\} + \varphi_{(i)} S_{2\varphi(i)} \\
- \ & \varphi_{(i+1)} \left\{ q_i + \int\limits_{r_i}^{r_{i+1}} \overline{\varepsilon}_2 e_i e_i' r dr \right\} = -\frac{4\pi}{c} \int\limits_{r_{i-1}}^{r_{i+1}} j_\theta e_i r dr \ ,
\end{aligned} \tag{4.35}$$

$$\begin{aligned}
& A_{z(i-1)}K_{3z(i-1)} + A_{z(i+1)}K_{3z(i)} \\
+ \ & A_{z(i)} \left\{ \int\limits_{r_{i-1}}^{r_{i+1}} \left(\overline{\varepsilon}_3 - \frac{m^2}{r^2} - k_z^2 \right) e_i^2 r dr - a_{i-1} - a_i \right\} \\
+ \ & \varphi_{(i-1)}K_{3\varphi(i-1)} + \varphi_{(i)}S_{3\varphi(i)} + \varphi_{(i+1)}K_{3\varphi(i)} \\
= \ & -\frac{4\pi}{c} \int\limits_{r_{i-1}}^{r_{i+1}} j_z e_i r dr \ ,
\end{aligned} \tag{4.36}$$

$$
\begin{aligned}
& iA_{r(i-1)}\left\{p_{i-1}-\int_{r_{i-1}}^{r_i}\overline{\varepsilon}_1 e_{i-1}e_i^{'}rdr\right\}-A_{r(i)}S_{1\varphi(i)} \\
+\ & iA_{r(i+1)}\left\{p_i-\int_{r_i}^{r_{i+1}}\overline{\varepsilon}_1 e_{i+1}e_i^{'}rdr\right\} \\
+\ & A_{\theta(i-1)}\left\{-q_{i-1}+\int_{r_{i-1}}^{r_i}\overline{\varepsilon}_2 e_{i-1}e_i^{'}rdr\right\}+A_{\theta(i)}S_{2\varphi(i)} \\
+\ & A_{\theta(i+1)}\left\{-q_i+\int_{r_i}^{r_{i+1}}\overline{\varepsilon}_2 e_{i+1}e_i^{'}rdr\right\} \\
+\ & A_{z(i-1)}K_{3\varphi(i-1)}+A_{z(i)}S_{3\varphi(i)}+A_{z(i+1)}K_{3\varphi(i)} \\
+\ & \varphi_{(i-1)}K_{4\varphi(i-1)}+\varphi_{(i+1)}K_{4\varphi(i)} \\
+\ & \varphi_{(i)}\left\{\int_{r_{i-1}}^{r_{i+1}}\left(\frac{m^2}{r^2}\overline{\varepsilon}_1+k_z^2\overline{\varepsilon}_3\right)e_i^2rdr-2m\int_{r_{i-1}}^{r_{i+1}}\overline{\varepsilon}_2 e_i e_i^{'}dr+b_{i-1}+b_i\right\} \\
=\ & \frac{4\pi\omega}{c}\int_{r_{i-1}}^{r_{i+1}}\rho e_i rdr\ , \qquad (4.37)
\end{aligned}
$$

where

$$
\begin{aligned}
K_{1r(i)} &= \int_{r_i}^{r_{i+1}}\left(\overline{\varepsilon}_1-\frac{m^2+1}{r^2}-k_z^2\right)e_i e_{i+1}rdr+a_i\ , \\
K_{1\theta(i)} &= i\int_{r_i}^{r_{i+1}}\left(\overline{\varepsilon}_2-\frac{2m}{r^2}\right)e_i e_{i+1}rdr\ , \\
K_{3z(i)} &= \int_{r_i}^{r_{i+1}}\left(\overline{\varepsilon}_3-\frac{m^2}{r^2}-k_z^2\right)e_i e_{i+1}rdr+a_i\ , \\
K_{3\varphi(i)} &= -k_z\int_{r_i}^{r_{i+1}}\overline{\varepsilon}_3 e_i e_{i+1}rdr\ , \\
K_{4\varphi(i)} &= \int_{r_i}^{r_{i+1}}\left(\frac{m^2}{r^2}\overline{\varepsilon}_1+k_z^2\overline{\varepsilon}_3\right)e_i e_{i+1}rdr-m\int_{r_i}^{r_{i+1}}\overline{\varepsilon}_2(e_i e_{i+1})^{'}dr-b_i\ , \\
S_{1r(i)} &= \int_{r_{i-1}}^{r_{i+1}}\left(\overline{\varepsilon}_1-\frac{m^2+1}{r^2}-k_z^2\right)e_i^2rdr-a_{i-1}-a_i\ , \\
S_{1\theta(i)} &= i\int_{r_{i-1}}^{r_{i+1}}\left(\overline{\varepsilon}_2-\frac{2m}{r^2}\right)e_i^2rdr\ , \\
S_{1\varphi(i)} &= i\int_{r_{i-1}}^{r_{i+1}}[\overline{\varepsilon}_1 e_i e_i^{'}r-m\overline{\varepsilon}_2 e_i^2]dr\ , \\
S_{2\varphi(i)} &= \int_{r_{i-1}}^{r_{i+1}}[\overline{\varepsilon}_2 e_i e_i^{'}r-m\overline{\varepsilon}_1 e_i^2]dr\ ,
\end{aligned}
$$

$$S_{3\varphi(i)} = -k_z \int_{r_{i-1}}^{r_{i+1}} \overline{\varepsilon}_3 e_i^2 r dr \ ,$$

$$a_i = \int_{r_i}^{r_{i+1}} (e_i')^2 r dr \ , \qquad b_i = \int_{r_i}^{r_{i+1}} \overline{\varepsilon}_1 (e_i')^2 r dr \ ,$$

$$p_i = m \int_{r_i}^{r_{i+1}} \overline{\varepsilon}_2 e_i e_{i+1} dr \ , \qquad q_i = m \int_{r_i}^{r_{i+1}} \overline{\varepsilon}_1 e_i e_{i+1} dr \ ,$$

and where $\varphi = \phi/k_0$, $\mathbf{j}$ and ρ are the external (antenna) current and charge density and prime designates the radial derivative. Equations (4.34) — (4.37) represent the general case, $i \neq 1, \ N$.

On the *conducting shell*, $i = N$ (r_N=b), we set $A_{\theta(N)} = A_{z(N)} = \varphi_{(N)} = 0$ simply by taking the finite element representation, Eq. (4.33), of $\{A_\theta, A_z, \phi\}$ (as well as $\{F_\theta, F_z, G\}$) without the Nth term. The last equation in the system obtained with $(\mathbf{F}, G) = (e_N, 0, 0, 0)$ is different from the general case, Eq. (4.34):

$$\begin{aligned} & A_{r(N-1)} K_{1r(N-1)} + A_{\theta(N-1)} K_{1\theta(N-1)} \\ + \ & A_{r(N)} \left\{ \int_{r_{N-1}}^{r_N} \left(\overline{\varepsilon}_1 - \frac{m^2+1}{r^2} - k_z^2 \right) e_N^2 r dr - a_{N-1} - 1 \right\} \\ - \ & i\varphi_{(N-1)} \left\{ p_{N-1} + \int_{r_{N-1}}^{r_N} \overline{\varepsilon}_1 e_N e_N' r dr \right\} = -\frac{4\pi}{c} \int_{r_{N-1}}^{r_N} j_r e_N r dr \ . \end{aligned}$$

On the axis, $i = 0$ ($r_0 = 0$), we take $\{\mathbf{A}, \phi\} = 0$ for all components by canceling the 0th terms in Eq. (4.33) for them (as well as for $\{\mathbf{F}, G\}$), except $\{A_r, A_\theta\}$ (and $\{F_r, F_\theta\}$) for $|m| = 1$ and $\{A_z, \phi\}$ (and $\{F_z, G\}$) for $m = 0$ which are $\sim const$ (Eqs. (4.31), (4.32)). It is easy to see that we are forced to do so, otherwise some of the integrals in Eqs. (4.34) — (4.37) diverge at $r \to 0$ and the system (4.34) — (4.37) becomes degenerate. For programming, it is convenient to eliminate the $i = 0$ terms completely: we can always place the point r_1 sufficiently close to 0, so that $A_{r(0)} \simeq A_{r(1)}$, $A_{\theta(0)} \simeq A_{\theta(1)}$ for $|m| = 1$ and $A_{z(0)} \simeq A_{z(1)}$, $\varphi_{(0)} \simeq \varphi_{(1)}$, for $m = 0$, and add the corresponding terms in Eqs. (4.34) — (4.37) for them. Thus, for any m we disregard all the coefficients of $\{\mathbf{A}, \phi\}$ with $i = 0$ but make the "correction" of the corresponding matrix elements for $A_{r(1)}$ and $A_{\theta(1)}$ for $|m| = 1$ and for $A_{z(1)}$ and $\varphi_{(1)}$ for $m = 0$.

To achieve the necessary precision with the linear finite elements, it is sufficient to employ a 3-point Simpson formula on an element half-length, $r_{i-1} \leq r \leq r_i$, to compute most of the integrals containing the $\overline{\varepsilon}$ elements in Eqs. (4.34) — (4.37). It is also quite accurate for integrals of the form,

$$\int \overline{\varepsilon}_1 e_i^2 \frac{dr}{r} \qquad \text{and} \qquad \int \overline{\varepsilon}_1 e_i e_{i+1} \frac{dr}{r} \tag{4.38}$$

sufficiently far from $r = 0$, or more precisely, for such r_i and $\Delta r_i = r_i - r_{i-1}$ that either $r > 0.1a_{eff}$ or

$$\begin{cases} r_i \leq 0.1a_{eff} \\ \\ \dfrac{\Delta r_i}{r_i} < 0.65 - \sqrt{0.36 - \left(10\dfrac{r_i}{a_{eff}} - 0.4\right)^2} \end{cases}, \tag{4.39}$$

where a_{eff} is the "effective" plasma radius calculated in the assumption of parabolic-like density profile near $r = 0$:

$$a_{eff} = \sqrt{2n_e(0)/|n_e''(r)|_{r=0}} \, .$$

For $r_i < 0.1a_{eff}$ and outside the region on the $(r, \Delta r)$ plane given by Eq. (4.39), the following formulae provide the required accuracy for the integrals (4.38):

$$\int \overline{\varepsilon}_1 e_i^2 \frac{dr}{r} \simeq \overline{\varepsilon}_{1*} \int e_i^2 \frac{dr}{r} \, , \qquad \int \overline{\varepsilon}_1 e_i e_{i+1} \frac{dr}{r} \simeq \overline{\varepsilon}_{1*} \int e_i e_{i+1} \frac{dr}{r} \, ,$$

where $\overline{\varepsilon}_{1*}$ is the value of $\overline{\varepsilon}_1$ at the midpoint of an interval. The expressions for the remaining integrals can be obtained analytically.

The linear system, Eqs. (4.34) — (4.37), is then solved by Gaussian elimination. The above numerical scheme has been realized in the code UFEM which is described in Appendix C.

To conclude this Section, we briefly summarize the advantages of the approach taken:

- It allows us to construct a finite element algorithm which is pollution-free regardless of the types of resonances encountered by the wave in the plasma.
- The precision of the Coulomb gauge, $\nabla \cdot \mathbf{A} = 0$, provides the "measure" of the pollution. The plasma response is not distorted by the elimination of polluted modes.
- The vacuum is accounted for by a simple change in the dielectric tensor. The antenna can have an arbitrary shape and location.
- Despite involving an additional function, compared to Eq. (4.23), the discretization of all the $\{\mathbf{A}, \phi\}$ components can be made using the same set of basis functions. Due to the Laplacian structure of the equations, the matrix in the linear system is usually very well conditioned, with the largest elements concentrated on and near the main diagonal, (the reader can also refer to [73]). The matrix is also "dense": 60% of the matrix band in Eqs. (4.34) — (4.37) is "filled" (non-zero).

4.4 Numerical Convergence, Power Deposition and Energy Flux

With a sufficient number of m- and k_z- modes to describe the antenna-radiated wave spectrum, the numerical convergence depends only on the radial mesh. The wave energy characteristics, such as the power deposition and the Poynting vector, as quadratic forms of the wave field, usually show a slower convergence rate than the wave field quantities themselves with increasing r-mesh density [7, 73]. So, it is convenient to employ them to evaluate the accuracy of the solution.

We take the *local power deposition* as

$$q(\mathbf{r}) = \frac{1}{2} Re[\mathbf{E}^*(\mathbf{r}) \cdot \mathbf{j}(\mathbf{r})] \ , \tag{4.40}$$

where $\mathbf{E}$ is the wave electric field and $\mathbf{j}$ is the current induced by the wave in plasma,

$$j_i = \sigma_{ij} E_j \equiv \frac{i\omega}{4\pi} (\delta_{ij} - \varepsilon_{ij}) E_j \ . \tag{4.41}$$

Strictly speaking, the $q(\mathbf{r})$ defined by the Eq. (4.40) is rather the local *rate of work* done by the wave in a plasma than the local power deposition or absorption. The latter has been defined by evaluating the work done on a particle along its trajectory and is a positive definite quantity [101, 132]. The local rate of work done by the wave however can be locally negative in a warm plasma because particles accelerated by the wave at one point can return their energy to the wave later on [18]. Note that the definition of the local power absorption is mainly relevant for fusion plasmas where power deposition on a magnetic surface is required. For helicon sources where particle dynamics effects along a field line are of interest, the rate of work done by the wave is a more useful quantity (for a detailed discussion of this point see [18]). In any case, the useful data required is the effect of the wave on the electron energy distribution function. This permits important estimates to be made such as electron heating and direct wave induced ionisation. The response of the electron energy distribution is best derived by solution of the Boltzmann equation using the detailed linear wave electric field obtained from the code [17].

The *total* power deposition rate inside a plasma cylinder of radius r, $Q(r)$, can be expressed through the anti-Hermitian part of the dielectric tensor and split into (m, k_z)-modes:

$$\begin{aligned} Q(r) &= \int_0^r \int_0^{2\pi} d\theta \int dz \; q(\mathbf{r}') r' dr' \\ &= \frac{\pi c^2}{2\omega} \sum_m \int dk_z \int_0^r \Big\{ Im(\bar{\varepsilon}_1)[|\tilde{E}_r|^2 + |\tilde{E}_\theta|^2] \\ &+ 2Im(\bar{\varepsilon}_2) Im(\tilde{E}_r \tilde{E}_\theta^*) + Im(\bar{\varepsilon}_3)|\tilde{E}_z|^2 \Big\} r' dr' \ . \end{aligned} \tag{4.42}$$

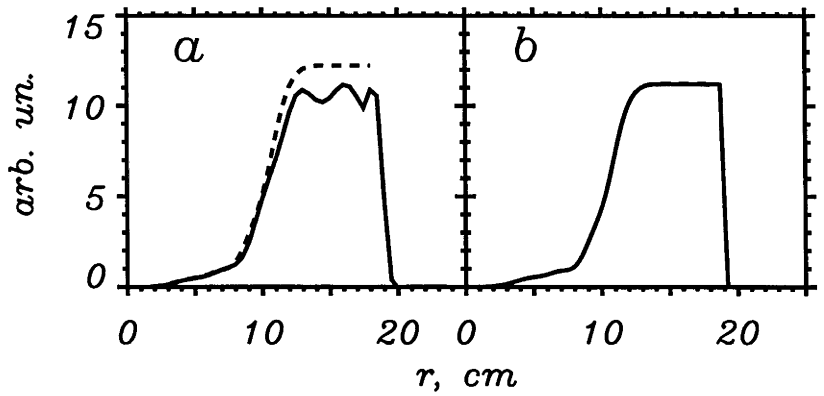

Figure 4.1: The radial profiles of the total radial flux of electromagnetic energy, $Pr(r)$ (solid line), and the total power deposition inside a cylinder of a radius r, $Q(r)$ (broken line), for the cases of poorly (a) (60 r-mesh points) and well (b) (812 r-mesh points) converged solution. $Pr(r)$ and $Q(r)$ practically coincide in plasma in case (b). The plasma radius, $a = 18$ cm, antenna is located at $r = [18.75, 19.05]$ cm.

Obviously, $Q(r)$ is positive for any r.

The *total* flux of the electromagnetic energy going into the cylinder of a radius r is the radial component of the Poynting vector flux integrated over the cylinder surface,

$$\begin{aligned} P_r(r) &= r\frac{c}{8\pi}\int_0^{2\pi} d\theta \int dz\ Re[\mathbf{E}(\mathbf{r}) \times \mathbf{B}^*(\mathbf{r})]_r \\ &= \frac{\pi r c}{2}\sum_m \int dk_z\ Re[\tilde{E}_z \tilde{B}_\theta^* - \tilde{E}_\theta \tilde{B}_z^*] \ . \end{aligned} \tag{4.43}$$

In Eqs. (4.42), (4.43), $\tilde{\mathbf{E}}$ and $\tilde{\mathbf{B}}$ are the Fourier-harmonics, $\mathbf{E}(r, m, k_z)$ and $\mathbf{B}(r, m, k_z)$, respectively.

It is straightforward to derive from Maxwell's equations that $P_r(r) = Q(r)$ at any radius within the antenna radius, $r \leq r_{ant}$. We will use this integral relation to study the convergence properties of the algorithm and to evaluate the accuracy of the solution.

Figure 4.1 demonstrates typical cases of poorly and well converged solution. The manifestation of poor convergence is usually the "zigzagged" shape of $P_r(r)$ and its poor agreement with $Q(r)$. Typically, this is the case when the local r-mesh step is not sufficiently small compared to the local radial wavelength. In the case of good convergence, the curves of $P_r(r)$ and $Q(r)$ coincide reasonably well. In addition, if the antenna is in a vacuum, the maximum of the curve $P_r(r)$ near the antenna must coincide with the antenna radiated power computed from the impedance, $W = (1/2)Re(Z) \cdot I_0^2$.

The curve $P_r(r)$ also provides valuable information about the radial propagation

and dissipation of the wave energy.

4.5 Numerical Pollution; the Asymptotic Region at $r \to 0$

As indicated in § 4.3, the precision with which the algorithm maintains the Coulomb gauge, $\nabla \cdot \mathbf{A} = 0$, or more precisely, the relative value of $\nabla \cdot \mathbf{A}$, i. e. $a|\nabla \cdot \mathbf{A}|/|\mathbf{A}|$ (where a is the typical radial dimension of the system, for example, the plasma radius) can be considered as the *pollution factor* indicating the level of the numerical pollution of the solution. As a rule, the properly converged solution yields low $a|\nabla \cdot \mathbf{A}|/|\mathbf{A}|$. Practical computations and convergence study show that usually $a|\nabla \cdot \mathbf{A}|/|\mathbf{A}| \leq 0.03 - 0.05$ is acceptable.

Figure 4.2 shows a typical radial profile of $a|\nabla \cdot \mathbf{A}|/|\mathbf{A}|$; in the bulk of the system volume $a|\nabla \cdot \mathbf{A}|/|\mathbf{A}| \leq 10^{-3}$. Usually the pollution factor grows from the conducting boundary, where the gauge condition, $\nabla \cdot \mathbf{A} = 0$, has been imposed, towards the plasma center. It has been noted that for azimuthal modes $|m| \geq 3$ this growth can be very sharp near $r = 0$, while for $|m| \leq 1$ the pollution factor remains small everywhere. By applying very dense r-meshes near the center we can virtually suppress this growth. Surprisingly, this does not affect the field structure (except at a very small region near $r = 0$) indicating that even with the large pollution factor near $r = 0$ the resulting wave field is, in general, pollution-free. We have found an explanation for this effect in the observation that the approximation of the fields by linear finite elements often fails to reproduce exactly the asymptotic field behavior of the type $\sim r^{|m|}$ for $|m| \geq 3$ (Eq. (4.31)). The accuracy of the linear approximation at $r \to 0$ can be evaluated as follows. In Eqs. (4.34) — (4.37), the least accurate at $r \to 0$ are the integrals of the type $\int_{r_{i-1}}^{r_i} e_i^2 r dr$. By comparing them to the integrals in which the proper function, $\sim r^{|m|}$, is used for e_i we find that the relative accuracy of the linear representation of the fields at $r \to 0$ is

$$\frac{|m|(|m|-1)}{6}\left(\frac{\Delta r_i}{r_{i-1}}\right)^2 . \tag{4.44}$$

Obviously, for $|m| \leq 1$ when all field components are "linear" (Eq. (4.31)), this problem does not exist. Computations show that it practically does not exist for $|m| = 2$ either, since A_r and A_θ are still linear. Even for $|m| \geq 3$, the field amplitude usually shows reasonable behavior at $r \to 0$, however the phase can be significantly distorted. At the same time, a very accurate field representation is required to maintain $\nabla \cdot \mathbf{A} \approx 0$. Equation (4.44) shows that the application of a more dense r-mesh should improve the solution (the best results in terms of $a|\nabla \cdot \mathbf{A}|/|\mathbf{A}|$ were achieved with irregular piecewise-exponential r-meshes of the type $r_i = r_0 \exp\{\alpha \cdot (i - i_0)\}$ since they minimize the pollution factor with the minimum number of

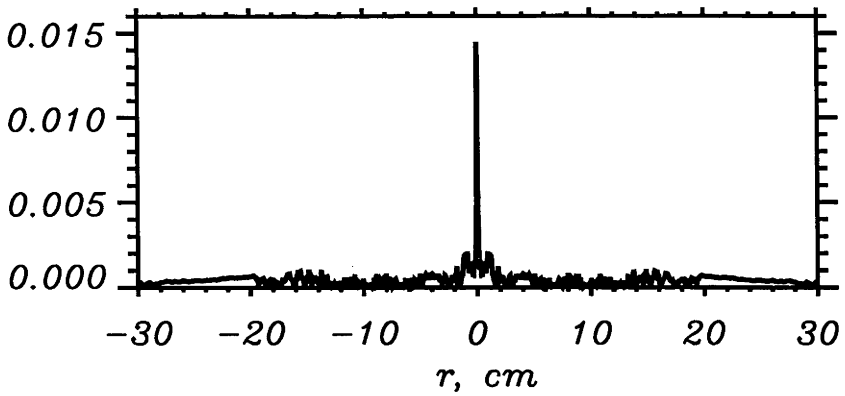

Figure 4.2: The radial profile of the pollution factor, $a|\nabla \cdot \mathbf{A}|/|\mathbf{A}|$, in the case of well converged solution for the conditions of Fig. 4.1(b), $m = -1, \ldots + 3$.

r-mesh points due to almost constant $\Delta r_i/r_i$). Unfortunately, Eq. (4.44) also shows that the mesh density must grow infinitely towards the center. In fact, if we want to reproduce the fields near $r = 0$ correctly for any m, we are forced to employ the analytic "solution" (Eq. (4.31)) at $r \to 0$.

With cubic finite elements, the solution remains unperturbed at $r \to 0$ for much larger $|m|$'s [73]. However, the analogous analysis indicates that the same problem may arise for $|m| > 8$ — 9.

The match between the finite elements and the asymptotic solution, Eq. (4.31), can be achieved in several ways:

- 1. We can make e_0 and the inner half-element of e_1 (which can be made sufficiently "long") to be $\sim r^{|m|}$, $r^{|m|-1}$ (depending on the field component) instead of linear functions.

- 2. We can assume the "asymptotic" relationship (Eq. (4.31)) between the ith and $(i-1)$th coefficients of the fields at a certain radius, r_{i*}, and hence, eliminate all $i < i_*$ from the linear system, Eqs. (4.34) — (4.37).

- 3. We can find a solution using linear elements and then "forget" about it within some radius r_m and continue the obtained solution "analytically" according to Eq. (4.31) for $r < r_m$.

All these approaches have been tried and gave similar results. However, the third one, which is simultaneously the simplest one, gave the best results in terms of $a|\nabla \cdot \mathbf{A}|/|\mathbf{A}|$. It has therefore been employed in the code UFEM. There is no general recipe which yields the value of the "match" radius r_m in each particular case, and strictly speaking, it depends on m: the larger is the $|m|$, the larger is the "asymptotic region". However, in practical computation, this region is usually quite evident. If we use the modes $|m| > 2$ and see the unphysical phase distortion near $r = 0$, the easy way to eliminate it is to increase the r_m.

We can also suggest another possible explanation for the growth of the pollution factor at $r \to 0$. In the asymptotic region (Eq. (4.31)) where the operator ∇^2 becomes "almost simply" a coefficient (depending on r), Eqs. (4.26) and (4.27) suggest that in this region the variational form, Eqs. (4.29), and the resulting linear system, Eqs. (4.34) — (4.37), either cannot keep $\nabla \cdot \mathbf{A} = 0$ or the 4 matrix lines corresponding to each r_i must be linearly dependent. It turns out that between these 2 "options": either to keep $\nabla \cdot \mathbf{A} = 0$ or to produce a "good" solution, the variational form tends to "choose" the second one, because commonly this problem practically does not affect the global field structure. This can also explain a strange effect we have observed: with a very dense r-mesh near $r = 0$, the application of double precision for the computation of the matrix elements in Eqs. (4.34) — (4.37) can sometimes produce a result worse than with the single precision; $\nabla \cdot \mathbf{A} = 0$ is maintained more precisely leading to higher degeneration of the linear system at small r. However, this observation still remains the author's hypothesis which has not yet been checked numerically. In any case, this would force one to use the analytic solution at $r \to 0$ as well.

4.6 Comparison with the Code ISMENE 5

To make an independent benchmarking of the code UFEM, we performed a detailed quantitative comparison between the wave field structures and the antenna impedances produced by the UFEM code and the ISMENE 5 code [7, 133] (borrowed from the CRPP, Lausanne) for the same conditions in four frequency ranges. The comparison is also of interest because, *a priori*, it is not clear whether the discretization scheme employed in ISMENE is suitable for computations when the LHR is present in the plasma.

The code ISMENE 5 is a 1D cylindrical kinetic code which solves electromagnetic wave equations in terms of $\mathbf{E}$ using cubic Hermite finite elements. It accounts for the 1st and 2nd order FLR terms and was designed primarily to study AWH and ICRH in tokamaks. Since this code works with a limited number of discrete k_z's (toroidal eigenmodes), and since it is not easy and straightforward to put a realistic antenna in it, a comparison was made for single $(m,\ k_z)$-modes. In each case a sufficiently well excited mode was chosen from the antenna radiation resistance spectrum.

We use the following set of parameters. The "cylindrical torus" (Appendix A (B)) of major radius $R_{tor} = 1$ m, conducting wall ("minor") radius $b = 30$ cm and plasma radius, $a = 18$ cm. The single-species fully ionized plasma has the following density and temperature profiles:

$$n_e(r) = n_{e0}\left(1 - 0.98\frac{r^2}{a^2}\right)^{0.7}, \qquad T_{e,i}(r) = T_0\left(1 - 0.95\frac{r^2}{a^2}\right)^2.$$

Since ISMENE only takes into account electron–ion collisions in the ε_{33} component of plasma dielectric tensor, we set the collision frequencies to zero in both codes (except the "LH case" (4)) to make the plasma conditions fully equivalent. The antenna used is an idealized monochromatic "helical antenna" [6] which launches a unique eigenmode and has the Fourier spectrum

$$j_r = 0 \ , \qquad j_\theta = I_0 k_z \ , \qquad j_z = -I_0 \frac{m}{r}$$

with the current amplitude, $I_0 = 267$ A, located at $r = 19$ cm. The temperature is chosen small enough to minimize the difference between the two codes arising from the neglect of FLR effects in UFEM.

(1) The typical **Alfvén wave case**, $\omega < \omega_{ci}$, was realized with a H^+ plasma, the magnetic field, $B_0 = 0.1$ T, frequency, $f = 1$ MHz, $n_{e0} = 10^{13}$ cm^{-3}, $T_0 = 4$ eV, m=–1, $k_z = 0.1$ cm^{-1} (10th toroidal mode, n=10). The analysis of the dispersion relation, Eq. (4.17), for this case shows that the conditions for the Alfvén resonance (§ 4.2) exists at $r \approx 12$ cm. The plasma is transparent ($Re(k_\perp^2) > 0$) for both the KAW (r < 12 cm) and the SQEW (r > 12 cm), but the latter is heavily damped near the plasma edge. The antenna impedance, Z, obtained by UFEM is $Z = 45.3 - 61.2i\ \Omega$ which is very close to the impedance obtained by ISMENE, $Z = 43.1 - 60i\ \Omega$. Figure 4.3 also demonstrates good agreement between the radial profiles of the wave electric fields obtained from the two codes.

Comparison of the two codes for this case at relatively high temperature, for example at $T_0 = 40$ eV and the same low magnetic field, $B_0 = 0.1$ T, showed a significant difference in the wave field structure in the plasma center. This is attributed to the neglect of FLR effects in UFEM.

(2) The typical **helicon wave case**, $\omega > 10\omega_{ci}$, is obtained if, compared to the previous case (1), we substitute H^+ by Ne^+ and take the mode m=+1, $k_z = 0.08$ cm^{-1} (n=8). In fact, n=8 is a very strong and, practically, single isolated mode (the first radial mode) in the radiation resistance spectrum for m=+1 for these conditions. The antenna impedances, $Z = 18.4 - 1153i\ \Omega$ (UFEM) and $Z = 20.4 - 1137i\ \Omega$ (ISMENE) are in good agreement. Figure 4.4 shows the wave field radial profiles for this case; with the exception of $Im(E_z)$, the match is practically perfect. The very sharp field variation near the plasma edge (the "LH spike", § 4.2), which occurs in both codes, was numerically resolved using a very fine radial mesh in this region.

(3) The **Trivelpiece–Gould mode case**, where $\omega \gg \omega_{LHR} = \sqrt{\omega_{ce}\omega_{ci}}$. The excitation of a strong TG wave (§ 4.2) can be observed if we take an Ar^+ plasma, $B_0 = 20$ G, $f = 13.56$ MHz, $n_{e0} = 3 \times 10^{11}$ cm^{-3}, m=+1, $k_z = 0.5$ cm^{-1} (n=50), other parameters are as in case (1). In this case, the plasma is entirely transparent ($Re(k_\perp^2) > 0$) for the TG wave, and the plasma interior, $r < 10$ cm, is

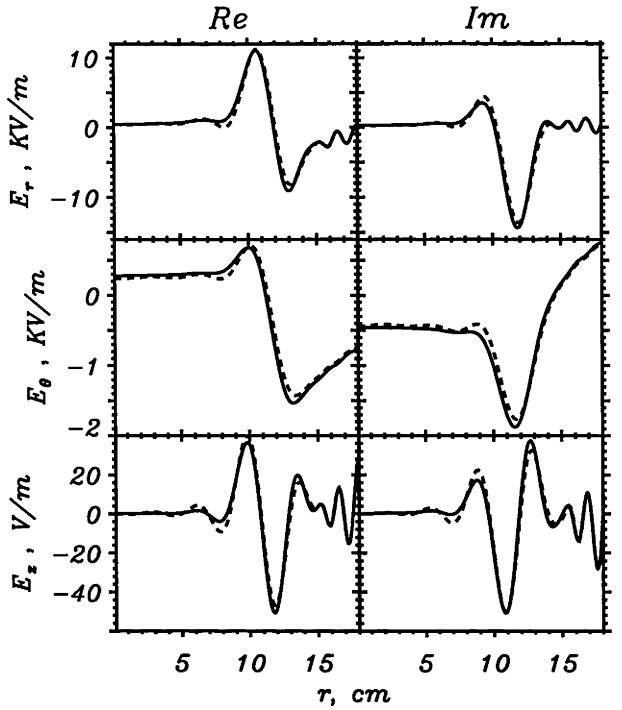

Figure 4.3: The radial profiles of the wave electric field in plasma ($r < 18$ cm) for the Alfvén wave case (1) obtained from UFEM (the solid line) and ISMENE (the broken line).

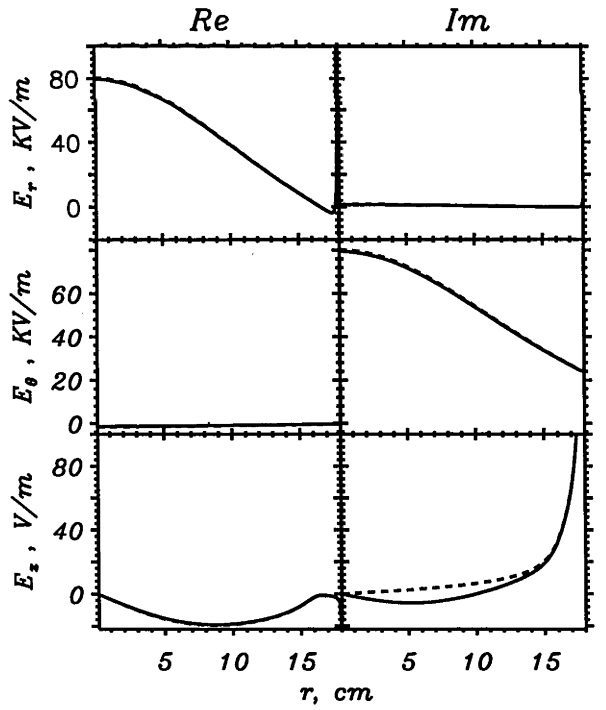

Figure 4.4: The radial profiles of the wave electric field for the helicon wave case (2). Notations are as in Fig. 4.3.

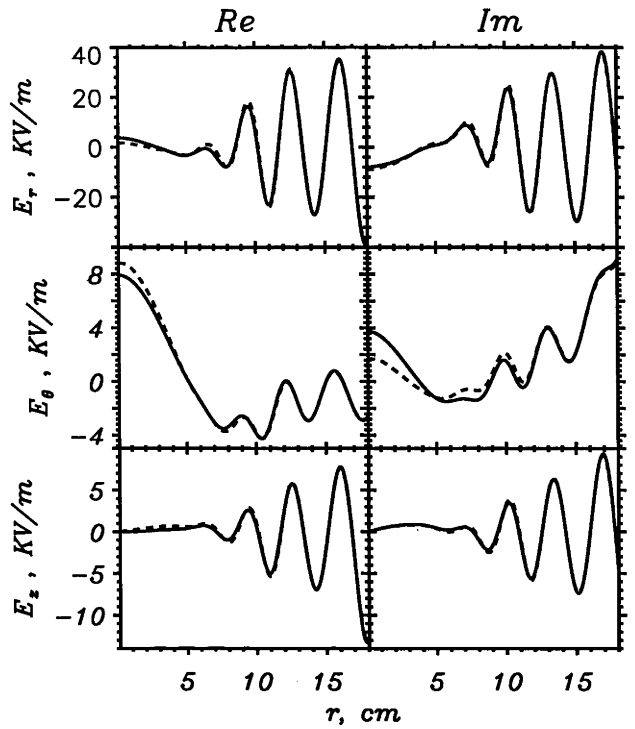

Figure 4.5: The radial profiles of the wave electric field for the TG mode case (3). Notations are as in Fig. 4.3.

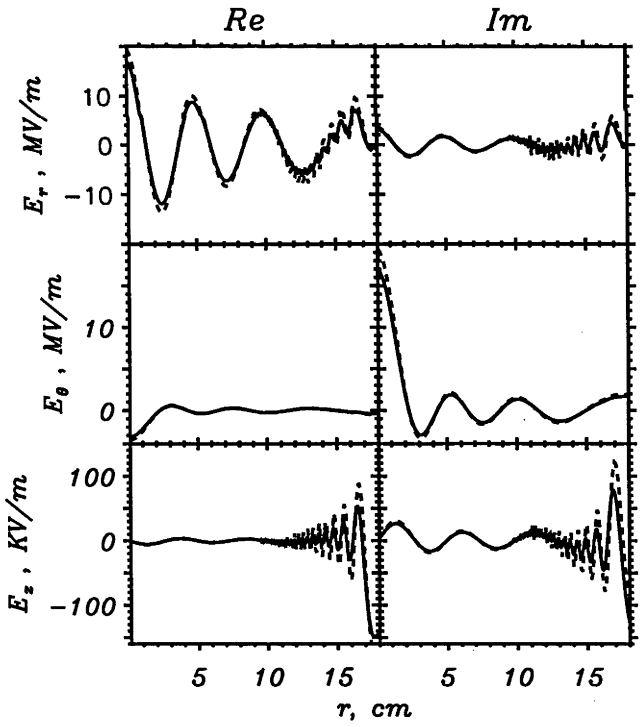

Figure 4.6: The radial profiles of the wave electric field for the LH wave case (4). Notations are as in Fig. 4.3.

also transparent for the helicon wave. The impedances, $Z = 264 - 4931i\ \Omega$ (UFEM) and $Z = 252 - 5151i\ \Omega$ (ISMENE) are again in good agreement. Figure 4.5 also demonstrates good agreement between the wave electric fields for this case.

(4) The **lower hybrid wave case**, where $\omega \sim \omega_{LHR} = \sqrt{\omega_{ce}\omega_{ci}}$. The excitation of the LH wave can be achieved in a D^+ plasma, with $B_0 = 20$ T, $f = 1$ GHz, $n_{e0} = 6.1 \times 10^{13}$ cm^{-3}, $T_0 = 6$ eV, m=+1, $k_z = 0.24$ cm^{-1} (n=24). In this case, we take a parabolic density profile with zero edge density, $n_e(r) = n_{e0}(1 - r^2/a^2)$, to reduce the wave field discontinuity at the plasma edge. We also include electron–ion collisions in ε_{33}. Other system parameters are as in case (1). The analysis of the wave dispersion shows that in this case the plasma is almost entirely transparent for the fast wave. The conditions for the lower hybrid resonance (§ 4.2) are met at $r \approx 9$ cm. For the LHW the plasma is transparent ($Re(k_\perp^2) > 0$) only for $r > 9$ cm. The antenna impedance obtained is $Z = 5 \times 10^4 - 3.25 \times 10^5 i\ \Omega$ (UFEM) and $Z = 5.86 \times 10^4 - 3.58 \times 10^5 i\ \Omega$ (ISMENE) and are again in good agreement. Figure 4.6 shows the wave field radial profiles for this case.

We conclude that there is good overall agreement (commonly, with an accuracy of 10 — 15 %) between the UFEM and ISMENE codes. This agreement is remarkable considering the variety of physical phenomena over the range of plasma parameters and frequencies from the Alfvén range, $\omega < \omega_{ci}$, up to well above the LH frequency and the different nature of the finite element discretization schemes employed in each code. As the code ISMENE itself has been benchmarked against several other codes [73, 74], the results presented in this Section give us a great deal of confidence in the validity of the code UFEM within the physical limits of the model chosen to describe the plasma (§ 4.1).

Chapter 5

Results

5.1 Comparison between MHD and Kinetic Models for BASIL

In this Section we compare the results computed by the two codes, FEM which employs the MHD numerical model of Chapter 2 and UFEM (Chapter 4 and Appendix C) which uses the kinetic plasma model. Our goal is to validate the use of the MHD model in the computation of helicon wave dispersion and antenna radiation resistance in high density sources like BASIL (Chapter 3) and to briefly analyze the differences between the two models with respect to such devices.

To demonstrate the comparison, we have chosen the following set of parameters which closely approximates one of the experimental cases of Chapter 3 and which is rather typical. We use BASIL parameters and $(3/2)\lambda$ helical antenna of Chapter 3 with $I_0 = 50$ A, $B_0 = 1537$ G, $f = 7$ MHz, $n_e(r) = 3.7 \times 10^{13}(1 - r^2/a^2)$ cm^{-3}, $T_e = 4$ eV $= const$, Ar^+ plasma with 4% ionization in the plasma center ($\approx$ 28 mTorr neutral gas filling pressure).

If we limit the spectrum to $m = \{-1, 0, +1, +3\}$ and $|k_z| \leq 1$ cm^{-1}, the total antenna impedance obtained by the two codes is $Z_\Sigma = 2.56 - 14.07i$ Ω (FEM) and $Z_\Sigma = 1.96 - 13.58i$ Ω (UFEM) with the following distribution between the azimuthal modes (FEM / UFEM):

- $Z(m{=}{-1}) = 0.0076 - 5.27i$ Ω / $0.148 - 5.38i$ Ω,
- $Z(m = 0) = 0.072 - 1.2i$ Ω / $0.098 - 1.15i$ Ω,
- $Z(m{=}{+1}) = 2.48 - 7.06i$ Ω / $1.71 - 6.51i$ Ω,
- $Z(m{=}{+3}) = 0.0019 - 0.547i$ Ω / $0.001 - 0.546i$ Ω

It is typical that UFEM produces the total R_{rad} 10 — 30 % smaller than FEM and that $R(m{=}{-1})$ is larger than in FEM but still much smaller than $R(m{=}{+1})$

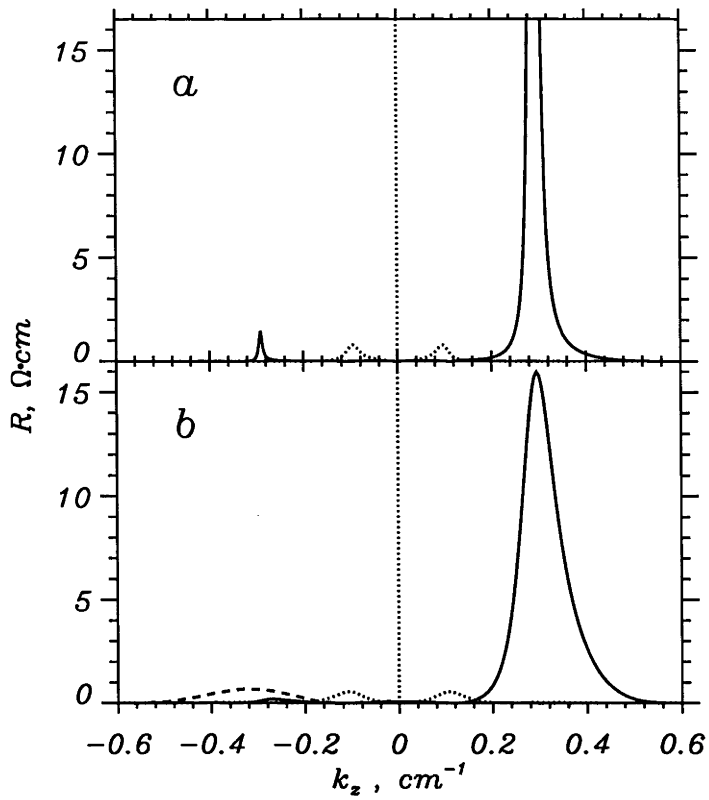

Figure 5.1: Radiation resistance k_z-spectra of $(3/2)\lambda$ helical antenna produced by (a) FEM code (MHD model) and (b) UFEM code (kinetic model) for BASIL. $B_0 =$ 1537 G, $f = 7$ MHz, $n_e(r) = 3.7 \times 10^{13}(1 - r^2/a^2)$ cm^{-3}, $T_e = 4$ eV, Ar^+, 4% ionization in the plasma center. m=+1 is shown by the solid line, m=0 by the dotted line and m=–1 by the dashed line.

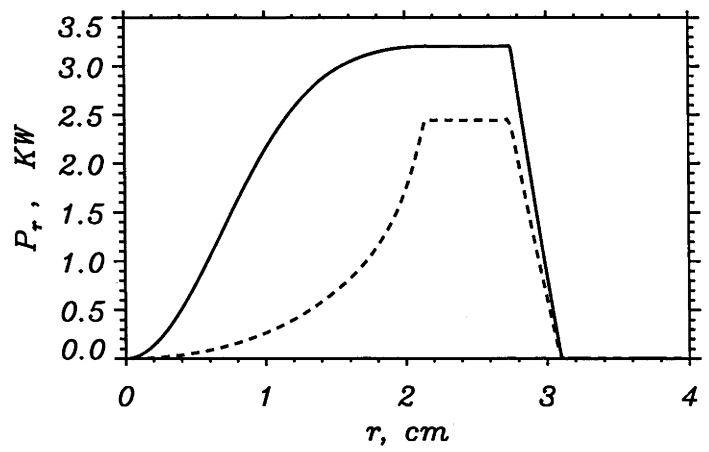

Figure 5.2: Radial electromagnetic energy flux for conditions of Fig. 5.1 by FEM code (solid line) and UFEM code (dashed line).

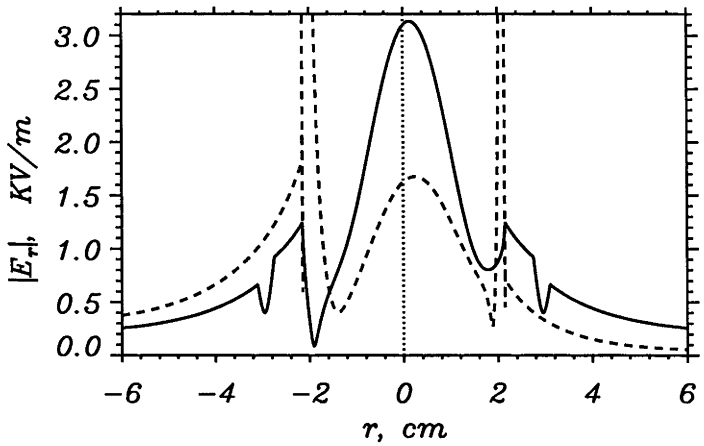

Figure 5.3: Radial profile of $|E_r|$ for conditions of Fig. 5.1 by FEM code (solid line) and UFEM code (dashed line) at $\theta = 0$, $z = 15$ cm.

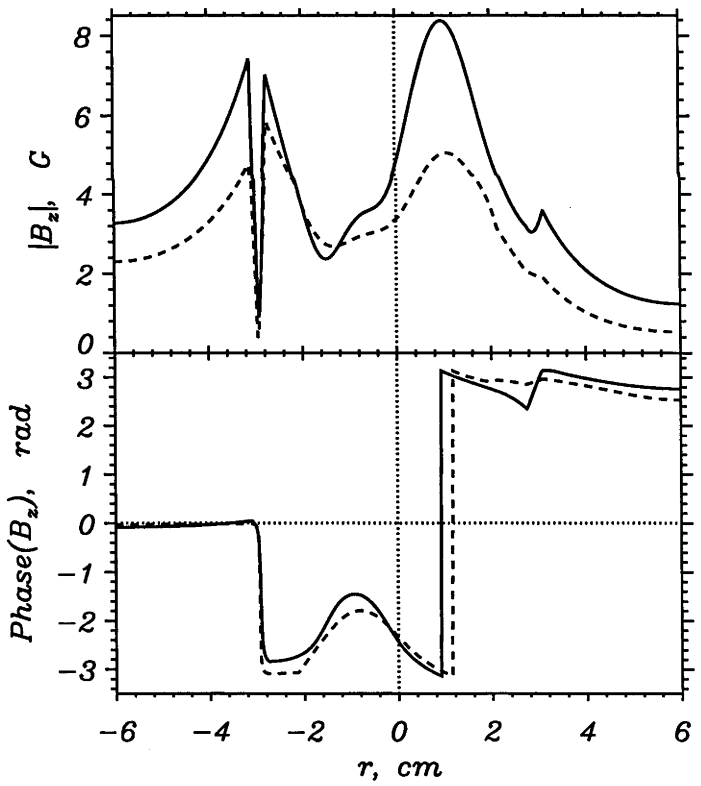

Figure 5.4: Radial profile of B_z as in Fig. 5.3.

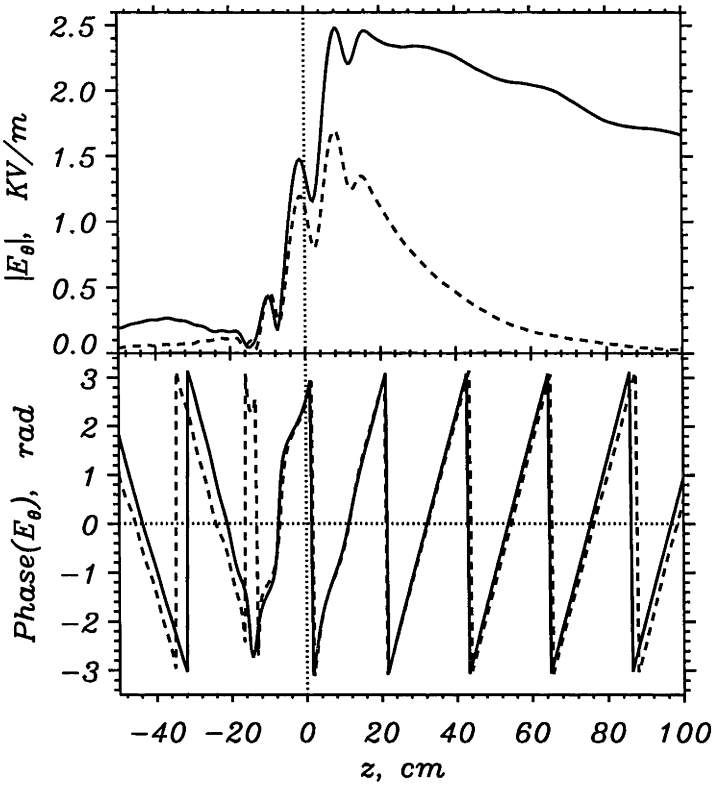

Figure 5.5: Axial profile of E_θ at $r = 1$ cm, $\theta = 0$ for conditions of Fig. 5.1 by FEM code (solid line) and UFEM code (dashed line).

which dominates the spectrum. The mode $\{m{=}{+}1,\ N_r{=}1\}$ has the largest R_{rad} in the spectrum in both codes.

The radiation resistance k_z-spectra are shown in Fig. 5.1. Clearly, FEM underestimates the wave dissipation. (In Fig. 5.1 (a) we do not show the total "height" of the first radial mode of $m{=}{+}1$ for FEM which reaches 175 Ω·cm.)

The positions of separate radial modes are very close in both codes. The maxima for the $m{=}{+}1$ mode occur at $k_z = \pm 0.292$ cm^{-1} (FEM) and k_z =[–0.267, 0.295] cm^{-1} (UFEM); for $m{=}0$ at $k_z = \pm 0.096$ cm^{-1} (FEM) and $k_z = \pm 0.108$ cm^{-1} (UFEM). The maxima in the spectrum of $m{=}{-}1$ (k_z =[–0.34, –0.02, 0.22] cm^{-1} (FEM) and k_z =[–0.318, –0.015, 0.213] cm^{-1} (UFEM)) cannot be considered as radial modes of $m{=}{-}1$ as they are rather due to the antenna current k_z-spectrum of this mode (Appendix B (D)) than the plasma response. If we can distinguish separate radial modes, analogous computation over a certain interval of k_z usually shows that for well excited modes (such as the first radial mode) their radiation resistances are also close in both codes. For example, for this case, $R(m{=}{+}1,N_r{=}1) \approx 2.3\ \Omega$ (FEM) and $R(m{=}{+}1,N_r{=}1) \approx 1.6\ \Omega$ (UFEM) which is $\approx 93\%$ of $R(m{=}{+}1)$ in both codes. We can conclude that the results obtained with the use of the MHD model presented in Chapters 2 and 3 are quantitatively quite accurate for the antenna radiation resistance and the spectrum (dispersion) of helicon waves. However, we

will further see that the detailed wavefield structures produced by the two codes can be significantly different.

Figure 5.2 shows that the radial electromagnetic energy flux (§ 4.4) in UFEM drops much faster over the radius, especially near the plasma edge, than in FEM due to the excitation of heavily damped surface slow wave (the LH wave, § 4.2).

Figure 5.3 demonstrates the radial profiles of $|E_r|$ for this case produced by FEM code (solid line) and UFEM code (dashed line) at $\theta = 0$, $z = 15$ cm, i. e. 1.5 cm from one of the antenna ends. The LHW manifests itself as a sharp "spike" of E_r near the plasma edge. Commonly, among the field components, the E_r only shows the "LH spike". In Fig. 5.3 we do not show the total amplitude of E_r at the "spikes" which is ≈ 34 kV/m (left) and ≈ 25 kV/m (right). As discussed in § 4.2, for such conditions the plasma is transparent for the LH wave only in a thin low density surface layer which is limited on the high density side by the LH resonance/cutoff pair. The layer is commonly so thin that the LHW does not have enough space to develop a radially propagating wave structure. It is interesting to note that even if we take a more realistic density profile with sufficiently high, non-zero edge density so as to eliminate the LHR in the UFEM code, the code shows the "LH spike" at the edge anyway: the finite element numerical scheme employed in it (§ 4.3) makes a kind of continuous smooth approximation for radial system parameters which is impossible to avoid. We must also note here that this "LH spike" has not been observed experimentally in BASIL due to difficulties in measuring the wave electric field in plasma, especially in a thin surface layer.

The wave magnetic fields (Fig. 5.4) and E_θ (Fig. 5.5) usually demonstrate an agreement between the two codes which is closer than for E_r in the antenna near field, yet the wave amplitude in UFEM is always smaller in the plasma center where it is determined by the helicon mode. It is difficult to make a direct comparison between the two codes in the far field where the helicon mode (in UFEM) completely dominates the wavefield structure since its axial damping is much larger in UFEM than in FEM (Fig. 5.5).

5.2 Helicon and Trivelpiece-Gould Waves in WOMBAT

In this Section we demonstrate some results of the simulations performed for the low density, low magnetic field helicon plasma source WOMBAT [48]. We approximate it as a half-infinite cylinder (Appendix A (D)). In WOMBAT, the "antenna region" tube (0.5 m long) is closed at one end by a conducting plate and is followed by a large (2 m long) diffusion chamber. No waves reflected from the diffusion chamber have been observed experimentally in the antenna region. A double half-turn antenna

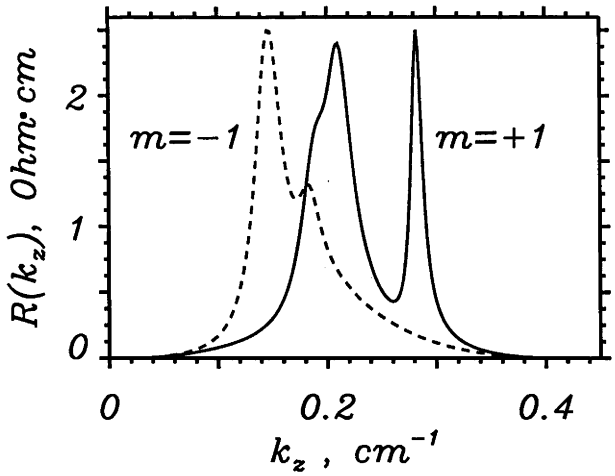

Figure 5.6: Spectrum of the antenna radiation resistance; m=+1 is shown by the solid line, m=–1 is shown by the dashed line.

([48], Appendix B (A)) is located at 7.5 cm from the conducting plate. The Ar^+ plasma is confined in a glass tube (we account for the electron–wall collisions, Eq. (4.14)) with inner radius $a = 9$ cm, and has a parabolic density profile with non-zero edge density, $n_e(r) = 3 \times 10^{11}\{0.2 + 0.8(1 - (r/a)^2\}$ cm^{-3}. The electron temperature profile is flat, $T_e = 3$ eV $= const$, the ion temperature, $T_i = 0$. The neutral gas concentration is $n_n \approx 3 \times 10^{13}$ cm^{-3} $= const$ which corresponds to the filling pressure $p \approx 0.9$ mTorr at $T = 300^0$ K and 1% ionization in the plasma center. The antenna excitation frequency, $f = 13.56$ MHz, the peak antenna current, $I_0 = 50$ A, the magnetic field, $B_0 = 50$ G. The radius of the inner antenna edge is $s = 9.7$ cm, the conducting shell radius, $b = 18.5$ cm.

The antenna radiation resistance obtained for the above conditions is $R_{rad} = 0.722\ \Omega$ which is close to the typical experimentally measured value. R_{rad} consists, almost entirely, of the modes m=+1 and m=–1, $R(m{=}+1) = 0.39\ \Omega$, $R(m{=}-1) = 0.332\ \Omega$, the contribution of other azimuthal modes is negligible. Figure 5.6 shows the k_z-spectrum of the radiation resistance. In accordance with the experimental observations [49], for the bulk of the spectrum the phase velocity parallel to the magnetic field (B_0) of the m=–1 mode is greater than that of m=+1. First radial mode of m=+1 of the helicon wave is clearly identifiable in Fig. 5.6 at $k_z \approx 0.29$ cm^{-1}, but higher order radial modes are obscured by a broad spectrum of TG waves.

The wavefield structure is presented in Figs. 5.7 — 5.11. In Figs. 5.7(a) and 5.10 we have chosen the isogrid so as to reveal the pattern inside the plasma. Clearly, the wavefield is the combination of the helicon and TG modes. The TG wave structure is quite evident for E_r, E_z (Figs. 5.7 and 5.8), B_θ and B_z, while the structure of E_θ and B_r is almost purely "heliconic". The resonance cone of the TG waves ($\theta \approx \omega/\omega_{ce} \approx 0.097 \approx 5.55^0$, see Eq. (4.22) and Ref. [15]) is also evident in Figs. 5.7(b) and 5.9; it intersects the z-axis ($r = 0$) at $z \approx 95$ cm. The

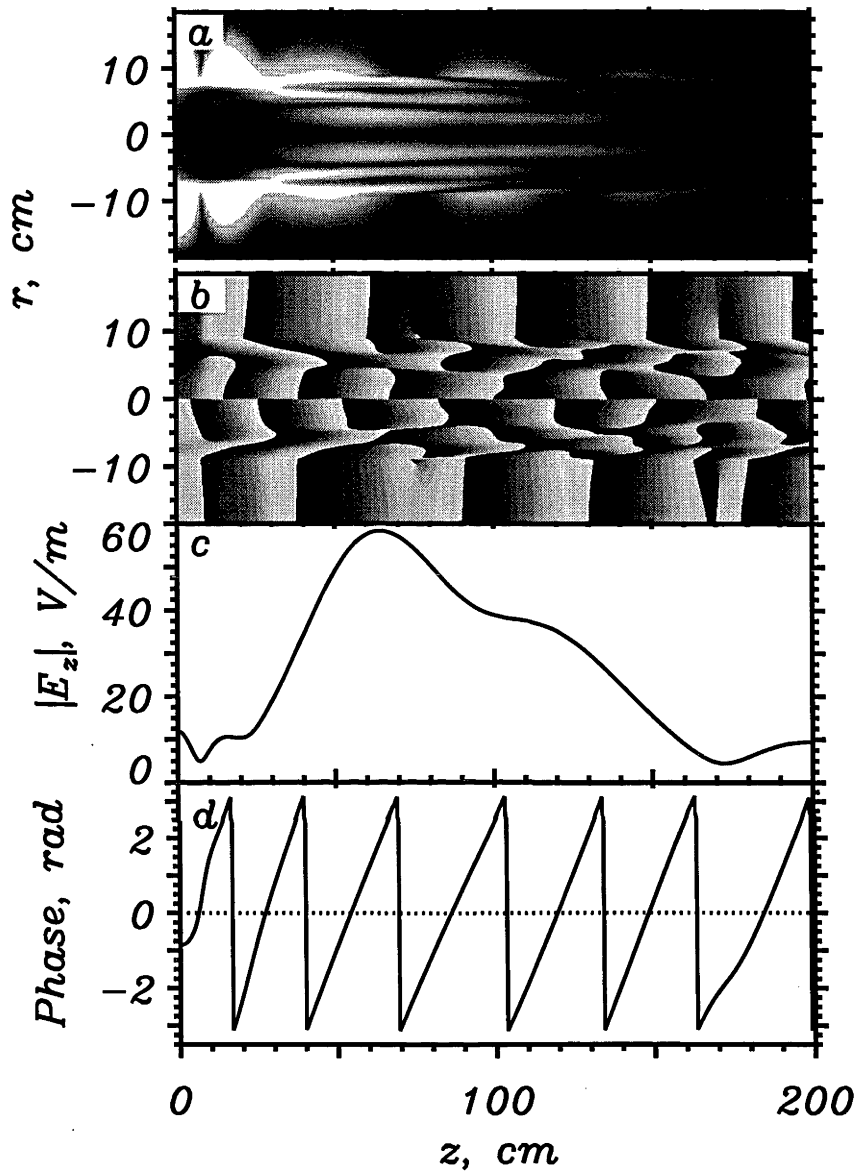

Figure 5.7: The amplitude (a) and phase (b) of E_z in the axial cross-section $\theta = 0$; $max|E_z| = 456$ V/m is near the antenna; near the plasma center $max|E_z| \approx 60$ V/m. The amplitude (c) and phase (d) of E_z at $\theta = 0$, $r = 3$ cm.

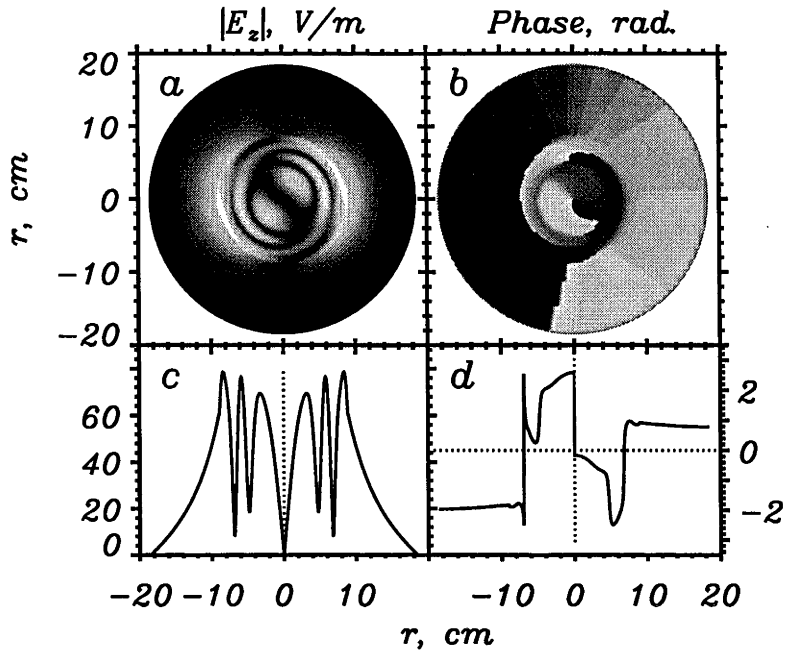

Figure 5.8: The amplitude (a) and phase (b) of E_z in the azimuthal cross-section $z = 50$ cm; $max|E_z| = 85$ V/m; $\theta = 0$ is horizontal. The amplitude (c) and phase (d) of E_z at $\theta = \pi/4$, $z = 50$ cm.

phase of the TG wave must be, in theory [15], constant and the TG wave phase velocity is infinite along the resonance cone. Practical computations with realistic system parameters show that the interaction between the helicon and TG modes and numerous wave reflections from the plasma boundary make the picture of the wave propagation rather complicated. The wave animation (Fig. 5.9) demonstrates that the disturbance propagates from the antenna along the resonance cone very quickly (but with a finite velocity) and the TG mode structure near the plasma edge propagates faster along B_0 than the helicon mode structure in the plasma center (not very far from the antenna where it can be identified). Down the plasma column this produces a complicated amplitude and phase distribution. For example, the amplitude of E_z shown in Figs. 5.8(a) and (c) at $z = 50$ cm resembles the third radial mode of the helicon wave, however it is not: Fig. 5.8(d) shows that the phase grows outwards near the plasma edge, as should be expected for TG modes (§ 4.2).

TG modes are mainly responsible for the dissipation of a large fraction ($\approx 1/2$) of the radiated power in the peripheral plasma near the antenna (Fig. 5.10). This is likely to be responsible for "hollow" plasma density profiles often observed in experiments [48, 52] in early phase of the discharge. The maximum of the power dissipation in the plasma center at $z \approx 40$ cm (Figs. 5.10 and 5.11) is probably due to two factors: the axial beat wavefield structure (§ 2.4) of the helicon mode which can

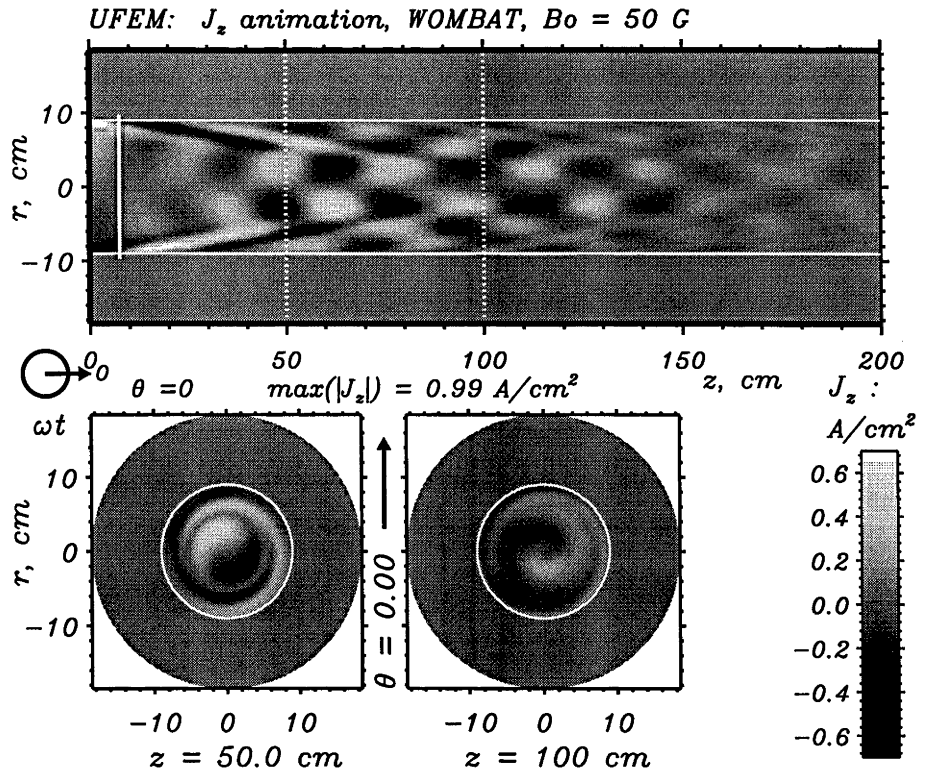

Figure 5.9: A frame from the wave animation subroutine of the UFEM code demonstrating interaction between helicon and TG waves in WOMBAT. The axial component of the wave-induced current in plasma is shown.

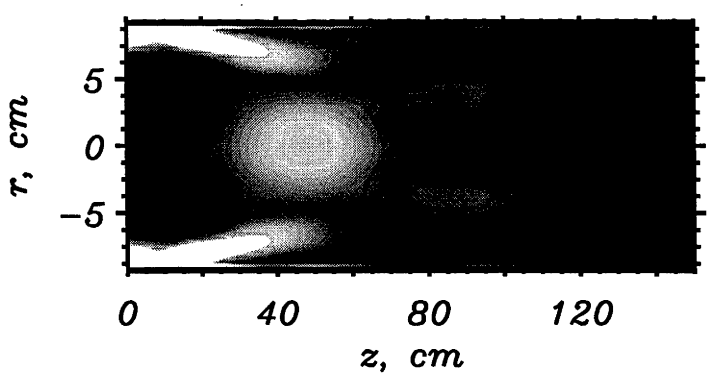

Figure 5.10: The local power deposition ($q = (1/2)Re(\mathbf{j} \cdot \mathbf{E}^*)$) in the axial cross-section $\theta = 0$; $max(q) = 0.9$ W/cm^3 is near the antenna; in the plasma center $max(q) \approx 0.05$ W/cm^3.

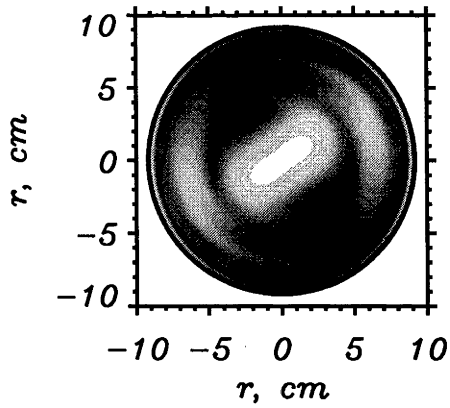

Figure 5.11: The local power deposition in the azimuthal cross-section $z = 50$ cm; $max(q) = 0.0543$ W/cm^3.

be expected with the spectrum as in Fig. 5.6, and the transient "overshoot" in the rate of work done by the wave in the antenna near field [18]. This can be connected to the enhanced ionization downstreams the plasma column recently observed in the experiments in WOMBAT [48].

5.3 L – H Mode Transitions in H-1NF are Connected to RF Heating?

Very interesting results were obtained when the UFEM code was applied to model rf plasma heating in H-1NF. In this Section we will discuss possible explanations for L – H transitions in H-1NF as well as some similarities between H-1NF and low density helicon sources. The latter comparison can be also beneficial for understanding of the discharge physics in helicon sources.

H-1NF is a medium-size helical axis stellarator (heliac) [64] which we model here by a periodic cylinder (Appendix A (B)) with the "torus" major radius, $R_{tor} = 1$ m. In reality, the plasma and chamber configurations in H-1NF are very complicated and can be quite adequately modelled only with the use of a fully 3D code. Qualitatively, the main difference between the 1D periodic cylinder and a 3D model can be the different spectra of global eigenmodes (different location and excitation efficiency of specific modes, possible appearance of continua and "gaps" in the spectrum, etc.). Also, due to complicated magnetic geometry, the kinetic wave dissipation can be larger than predicted by the cylindrical model and global resonances can be broadened by toroidal and poloidal mode coupling [136, 138]. However, the author believes that some important qualitative conclusions can be drawn from the present 1D cylindrical model as well.

It has been known for some time that during the experiments in H-1NF with the

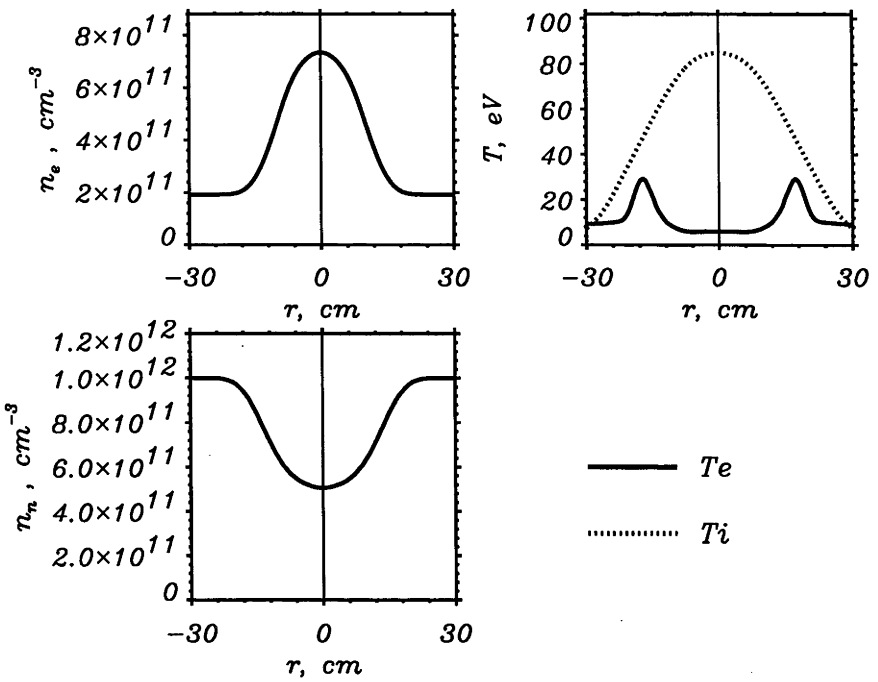

Figure 5.12: Radial profiles of plasma parameters in H-1NF in H-mode used in the code. "High edge density" case.

use of rf system for plasma formation and heating [16], the plasma can undergo the transition into the so-called "high confinement mode" (H-mode) [115, 116]. Compared to the "low confinement mode" (L-mode), the H-mode is characterized by higher plasma density, much lower level of fluctuations, high ion temperature (Fig. 5.12) and a potential "well" in the plasma center. L – H transitions were observed in several gases during the scans over the power coupled to the rf antenna and the confinement field. All these phenomena are currently not understood. In this Section we discuss two possible explanations of the L – H mode transition in H-1NF. We will not consider the effect of L – H transitions on confinement, stability and transport, hence this analysis is far from being complete. However, one of the hypotheses discussed below (or their combination) may provide a starting point for further detailed analysis.

We must also mention that, since there were certain doubts concerning the applicability of the UFEM code for these conditions due to the neglect of FLR effects, it has been also checked by the ISMENE code ([7, 133], § 4.6) that FLR effects are really unimportant here, at $\omega > 200\omega_{ci}$.

The plasma parameters used in the code are shown in Fig. 5.12, they approximate the experimentally measured ones [116]. Plasma occupies the whole volume: the plasma density is non-zero at the conducting wall, $a = b = 30$ cm, and in the antenna region. In Fig. 5.12, the $n_e(r)$ was taken from early experimental

measurements which were not quite reliable in the plasma periphery: it is likely that the edge density was several times overestimated. On the other hand, these measurements were made far from the antenna location, and we can suppose that the n_e near the antenna is actually higher. We will further see that this may have important consequences, so it is of significant interest to consider this, "high edge density", case. Later in this Section we will also consider the "low edge density" case for which $n_e(a) \approx 4 \times 10^{10}$ cm^{-3} and which looks more realistic. The plasma consists of 100% Ar^+. Note that the maximum ionization rate (in the plasma center) is only $\approx$ 60%, so it is reasonable to suppose that the plasma density is somehow proportional (through the ionization) to the antenna radiated power.

Curiously, in the H-mode the ion temperature reaches 85 eV in the plasma center, while the electron temperature is much lower, being $\approx$ 6 eV in the center and reaching $\approx$ 30 eV near the antenna. This unusual temperature difference also remains unexplained.

The antenna used in the code approximates the double saddle coil used in H-1NF (Appendix B (F), Fig. B.4, [16]) with $\theta_a = 0.3$ rad, $\theta_b = 1.3$ rad, $d = 1.2$ cm (the wire diameter) and $2l = 11.3$ cm (the antenna axial length). The radius of inner antenna edge, $s = 20$ cm. Since $\theta_a + \theta_b \approx \pi/2$, the $m = \pm 2$ azimuthal modes are the largest in the antenna current Fourier-spectrum. The antenna is "electrically long": the current is not constant along the antenna length and hence there is a charge distribution (Appendix B); it is also unshielded (no Faraday screen and no side limiters), so it operates in the plasma and is capable of drawing a significant sheath current through the plasma so that the current through the output feeder can be 5 — 35 % smaller than the current through the input feeder, $I_0 = 300$ A (peak value). To model this, we take the "current propagation constant", $\tilde{\beta} = 2 \times 10^{-3}$ cm^{-1} in the code (Appendix B) which corresponds to the 7% current difference. It should be noted however that even the 35% current difference ($\tilde{\beta} = 0.01$ cm^{-1}) does not have a significant effect on the wavefield structure and the antenna loading. The antenna excitation frequency, $f = 7$ MHz, which is close to the LHR frequency. The constant magnetic field, $B_0 = 0.077$ T in the code.

Under the above conditions, there is no LHR in plasma: $min(n_e) = n_e(a) = 1.92 \times 10^{11}$ cm^{-3} while the LHR layer appears in the plasma at $n_e \approx 1.915 \times 10^{11}$ cm^{-3}. (As mentioned in § 4.2, Eq. (4.21), for these conditions, the position of the LHR depends, with high accuracy, on density only and practically does not depend on the wavenumber.)

Figure 5.13 demonstrates the antenna impedance spectrum for this case. The best excited mode is $\{m{=}{+}1,\ n{=}6\}$ ($k_z = 0.06$ cm^{-1}), apparently, it is a global eigenmode. (In this Section, we do not account for the full spectrum of the antenna reactance, so the *Im(Z)* can be underestimated. Also note that the spectrum is discrete over k_z: by n we designate the toroidal mode number here, $k_z = n/R_{tor}$.)

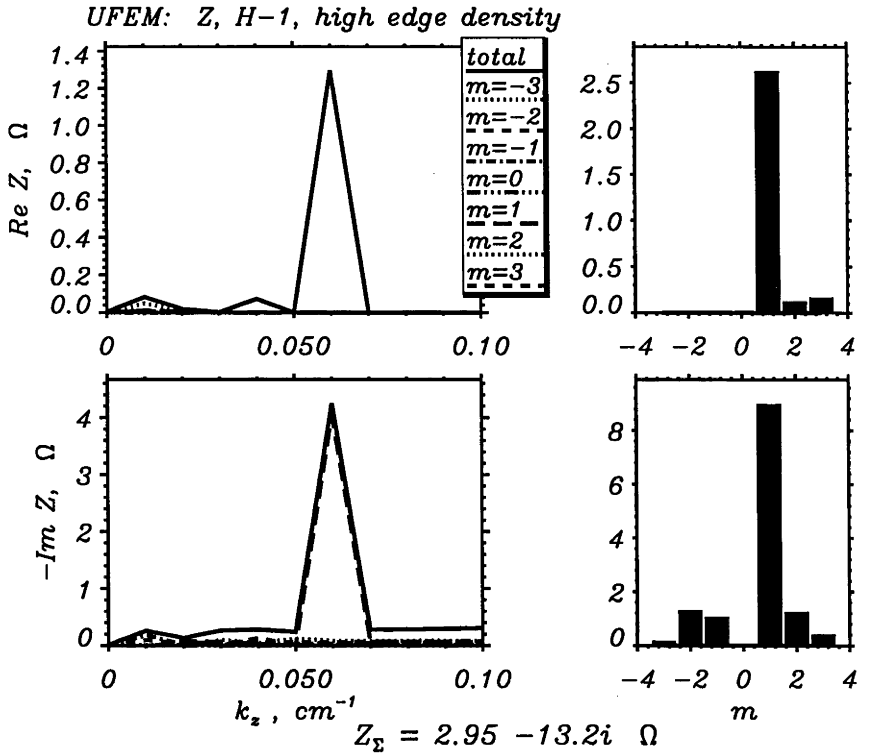

Figure 5.13: The antenna radiation resistance spectrum for the "high edge density" case.

$R_{rad} \approx 3\ \Omega$, the total radiated power, $P \approx 133$ kW.

Figure 5.14 shows a radial profile of E_r for this case. The wavefield structure is determined by the fast wave since the slow wave is evanescent in the entire volume. The remarkable feature of the FW under the conditions close to the LHR is that it very much resembles the LH wave: it is shortwavelength and almost purely electrostatic, yet "forward propagating" (§ 4.2). For this case, an attempt was made to compute the ion heating straightforwardly, by taking the ion part of the current (through the "ion" part of the plasma dielectric tensor, Eq. (4.2)) in $(1/2)Re(\mathbf{E}\cdot\mathbf{j}^*)$. The result was that only $\approx$ 100 W goes into the ion heating, while it can be estimated by a simple transport analysis that minimum $\approx$ 20 kW is required to maintain the ion temperature that high. We can safely conclude that the linear model used in UFEM is unable to explain this super-efficient ion heating in H-1NF and look for nonlinear mechanisms.

One reasonable possibility is the ion stochastic heating. The threshold criterion for this phenomenon to occur has been derived by C. Karney in several works on the stochastic ion heating by LH waves [79, 80, 81]. It states that the wave amplitude must be larger than the threshold value (in SI units),

$$E_{th} = \frac{1}{4}\left(\frac{\omega_{ci}}{\omega}\right)^{\frac{1}{3}} \frac{\omega}{k_\perp} B_0 \ , \tag{5.1}$$

where $k_\perp$ is the wavenumber perpendicular to the static magnetic field B_0. We

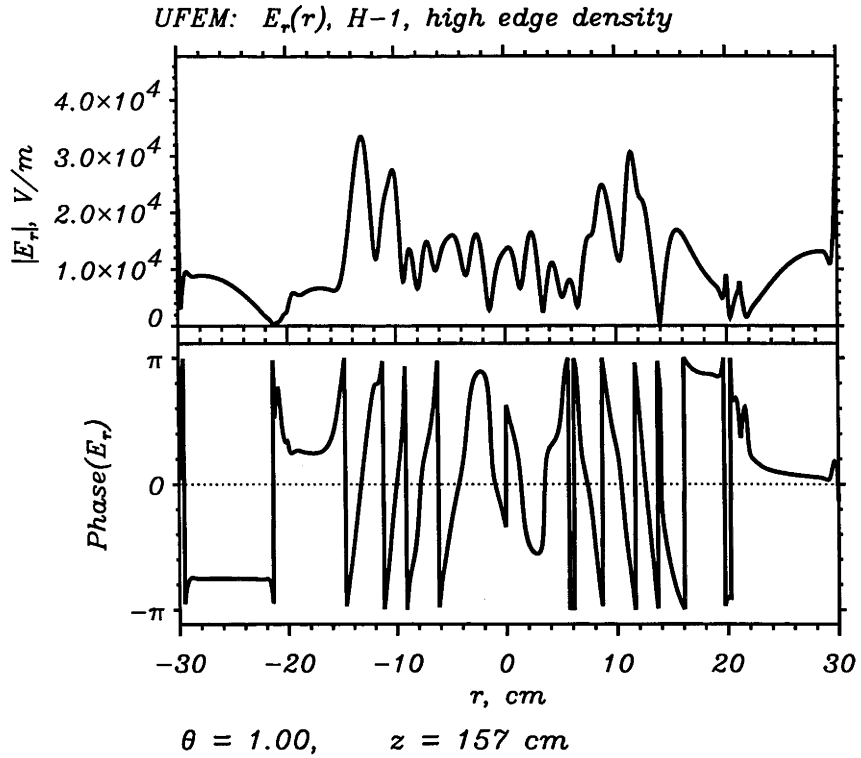

Figure 5.14: Radial profile of E_r in H-1NF at $z = 157$ cm, $\theta = 1$ rad. "High edge density" case.

can safely apply this theory under these conditions since the physical situation is almost equivalent to the LHH scenario. (In addition, it must be mentioned here that the theory of the stochastic ion heating can be considered very reliable, as it has been proven in both special experiments and LHH in tokamaks with the accuracy ±20%, [80, 81].) Calculation of $k_\perp$ of the FW for this case according to Eq. (4.17) shows that in the plasma center $k_{\perp FW} \approx 95$ m^{-1}, and Eq. (5.1) gives $E_{th} \approx 1.44$ kV/m. The wave amplitude in Fig. 5.14 is 10 — 20 times higher. Thus, we can expect that under these conditions the stochastic ion heating can be very robust. C. Karney shows in [81] that when $|\mathbf{E}| \gg E_{th}$, from 70% (in the regime when the dissipation is dominated by ion Landau damping on quiver motion) to almost 100% (in the regime dominated by collisional damping) of the wave energy goes into the ion heating. It should be further checked, both numerically and experimentally, whether the deformation of the ion distribution function in H-mode obeys Karney's theory. Later in this Section we will discuss a more realistic possibility of the wave amplitude being close to the stochastic heating threshold.

It is curious that the code-produced amplitude of the wave scalar potential for this case (Fig. 5.15) forms a "well" (yet zigzagged by the wavefield structure) dropping from 400 — 800 V near the antenna to 100 — 150 V in the center. The same order of magnitude drop has been measured in experiments for the *stationary* electric potential in the plasma. On the other hand, the wave of this amplitude can

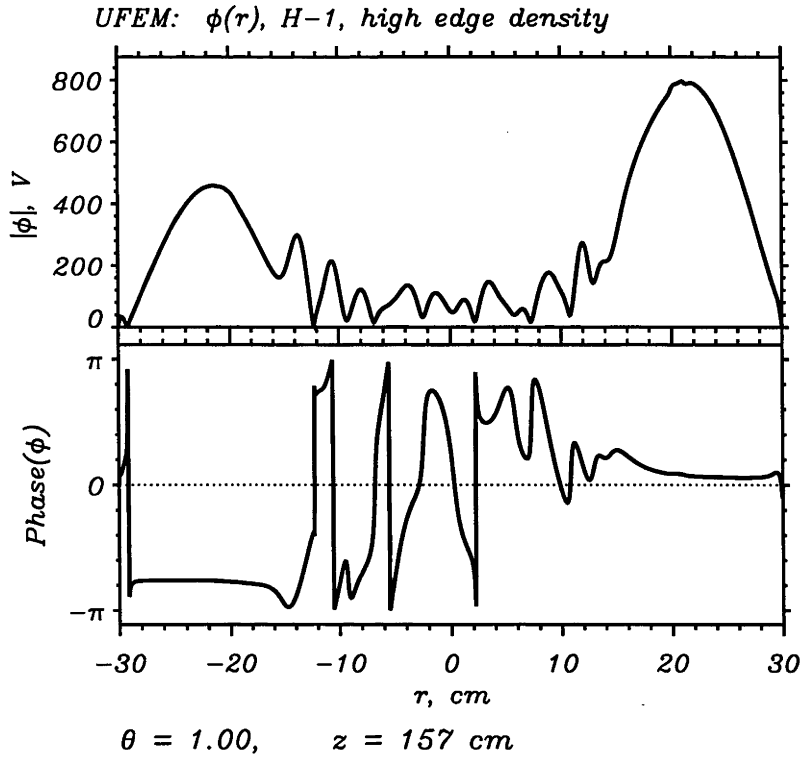

Figure 5.15: Radial profile of the wave scalar potential as in Fig. 5.14

develop a significant rf pressure [3, 61] which can also create a potential "well" in the plasma.

We now consider the "low edge density" case by changing the plasma density profile near the edge so that $n_e(a) \approx 4 \times 10^{10}$ cm^{-3}. Other system parameters are as in the previous case (Fig. 5.12). In this case, the LHR layer ($n_e = 1.915 \times 10^{11}$ cm^{-3}) is at $r \approx 15$ cm, i. e. ≈ 5 cm in front of the antenna (from the high density side). Figure 5.16 shows the antenna impedance spectrum for this case. The best excited mode in the spectrum of $Re(Z)$ is $\{m{=}{+}2,\ n{=}1\}$ ($k_z = 0.01$ cm^{-1}). R_{rad} is low ($\approx 0.14\ \Omega$) and so is the antenna radiated power, $P \approx 6.3$ kW. Figure 5.17 demonstrates a radial profile of E_r for this case. There is a large amplitude LH wave (which can only propagate in the low density edge plasma between the LHR layer and the wall, § 4.2), however the wave amplitude is much lower in the plasma bulk beyond the LHR layer. It looks like the LHR layer "shields" the antenna from the plasma. We have established that this picture remains qualitatively the same if we scan the plasma density (multiplying the above density profile by a factor) within the limits $n_e(0) = [7.46 - 8.13] \times 10^{11}$ cm^{-3} (except the small region near $n_e(0) = 7.65 \times 10^{11}$ cm^{-3} which we discuss below), despite the fact that R_{rad} is very sensitive to n_e due to a large number of close eigenmodes of the short wavelength LH wave: the 1 — 2 % change of n_e may result in a 20 — 30 % (or even larger) change of R_{rad}.

Comparing Figs. 5.13 and 5.14 with Figs. 5.16 and 5.17, one may suggest the

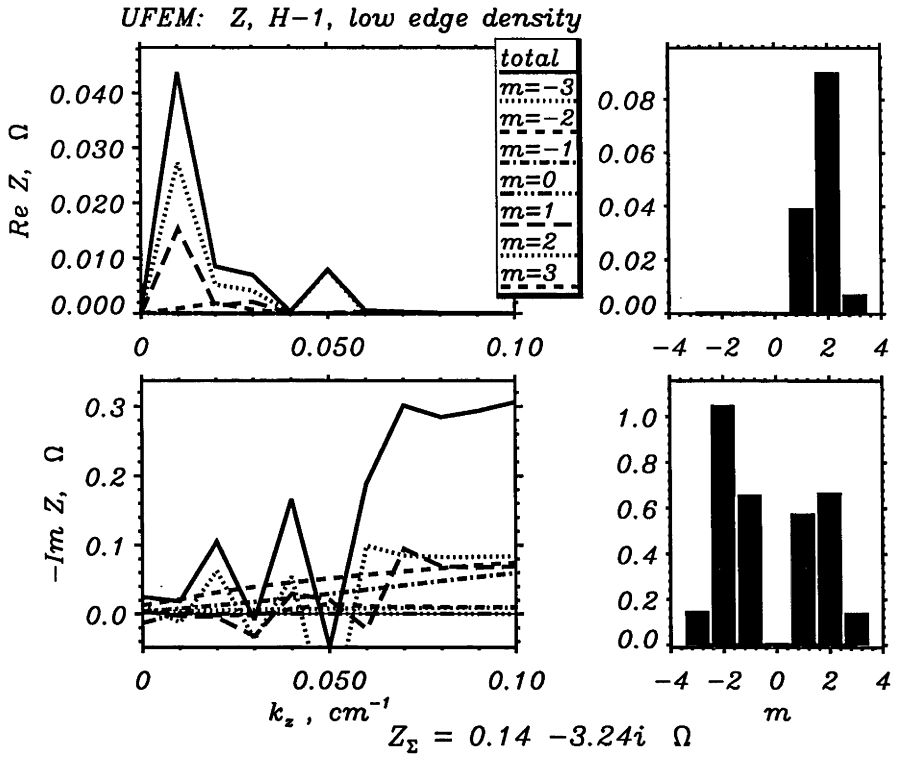

Figure 5.16: The antenna radiation resistance spectrum for the "low edge density" case, $n_e(0) = 7.94 \times 10^{11}$ cm^{-3}.

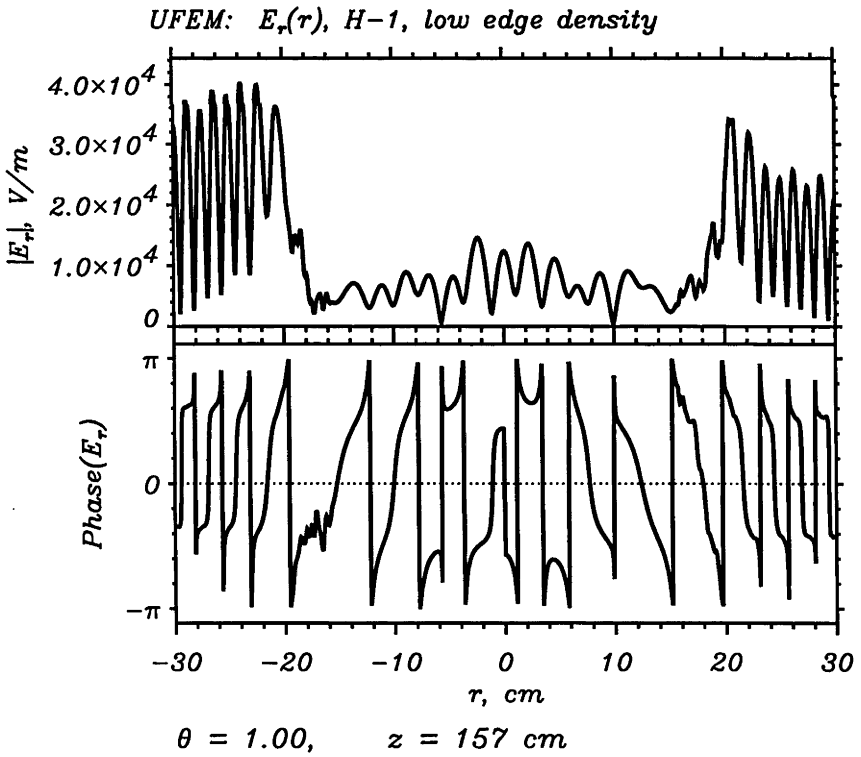

Figure 5.17: Radial profile of E_r for the "low edge density" case as in Fig. 5.16.

following explanation for the L – H transition. If we perform the power scan, then first, when the power (and density) is small, almost all of it is deposited in the plasma periphery since the LHR layer efficiently "shields" it from the plasma bulk. As the density grows, at a certain moment the n_e in front of the antenna becomes large enough, the LHR layer moves behind the antenna, so the wave suddenly "breaks through" into the plasma bulk causing the density and temperature jump. Further, the system picks up the nearest global eigenmode (not necessarily the $\{m{=}{+}1, n{=}6\}$ as in the above "high edge density" case, UFEM's periodic cylinder is too simple to model the real H-1NF's geometry) and stabilizes on it. This operational point can be stable (at least, it is clear that it can be stable in one direction) because

- if the density (power) sporadically rises, the system moves away from the resonance condition, the R_{rad} decreases and so does the power and, finally, the ionization rate and the density.

- if the density (power) sporadically drops, then we can expect that the LHR layer appears in front of the antenna, almost all the power is deposited near it, so the density rises back, eliminating the LHR.

It is also noticeable (in favour of the above hypothesis) that the position of the LHR depends on B_0, frequency and ion mass in the same way as the experimentally observed L – H transitions depend on the above values. To demonstrate the point, we re-write Eq. (4.21), which determines the LHR condition, in the following form in practical units:

$$\frac{4.3 \times 10^5}{M_i f^2} - \frac{1}{B_0^2} = \frac{9.72 \times 10^{12}}{n_e} , \tag{5.2}$$

where n_e is in cm^{-3}, B_0 is in T, f is in MHz and M_i is in atomic units. For example, if we take $B_0 = 0.1$ T instead of 0.07 T, then $n_{eLHR} = 8.14 \times 10^{10}$ cm^{-3}. If we fix $n_{eLHR} = 1.915 \times 10^{11}$ cm^{-3}, then the "critical" magnetic field, $B_0 = 0.051$ T for Ne^+ and $B_0 = 0.022$ T for He^+, etc.

Now, it is difficult to say whether the plasma density can be high enough near the antenna for this mechanism to work. The known peripheral n_e is well within the margin of experimental error; moreover, it has not been measured near the antenna itself.

This qualitative analysis would be incomplete if we did not consider the situation when a global eigenmode is excited in the presence of the LHR layer in front of the antenna. Figures 5.18 and 5.19 are obtained for the "low edge density" case with $n_e(0) = 7.65 \times 10^{11}$ cm^{-3} and show a strong resonance of the $\{m{=}{+}2, n{=}5\}$ mode. We can see that, in spite of the LHR layer in front of the antenna, a strong fast wave is excited in the plasma center and its structure very much resembles the first radial mode of $m{=}{+}2$. The ion stochastic heating is also possible: $k_{\perp FW} \approx 17.3$

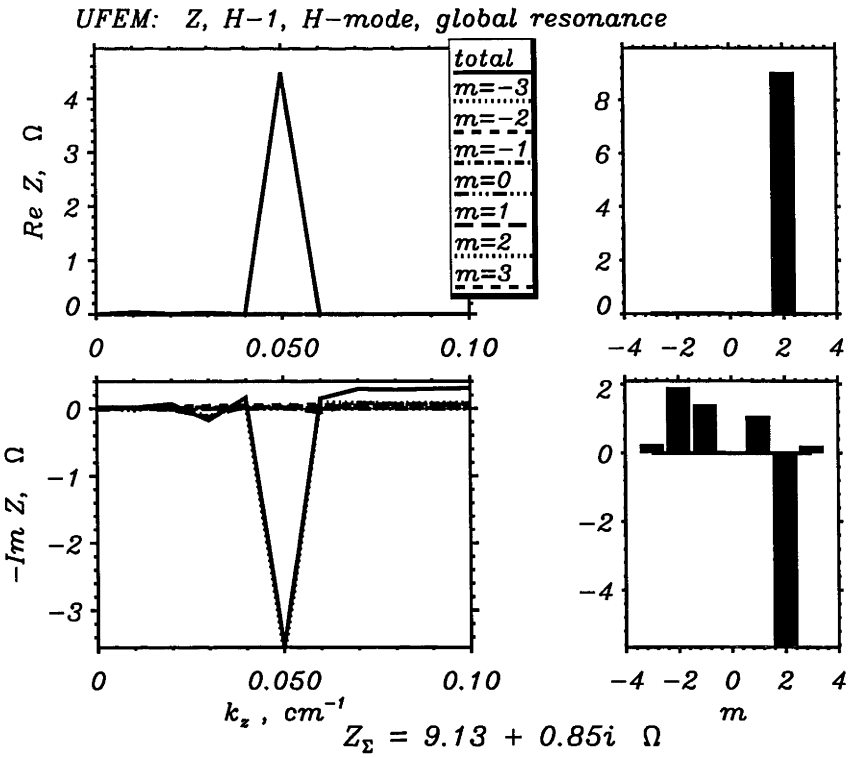

Figure 5.18: The antenna radiation resistance spectrum for the "low edge density" case with $n_e(0) = 7.65 \times 10^{11}$ cm^{-3}.

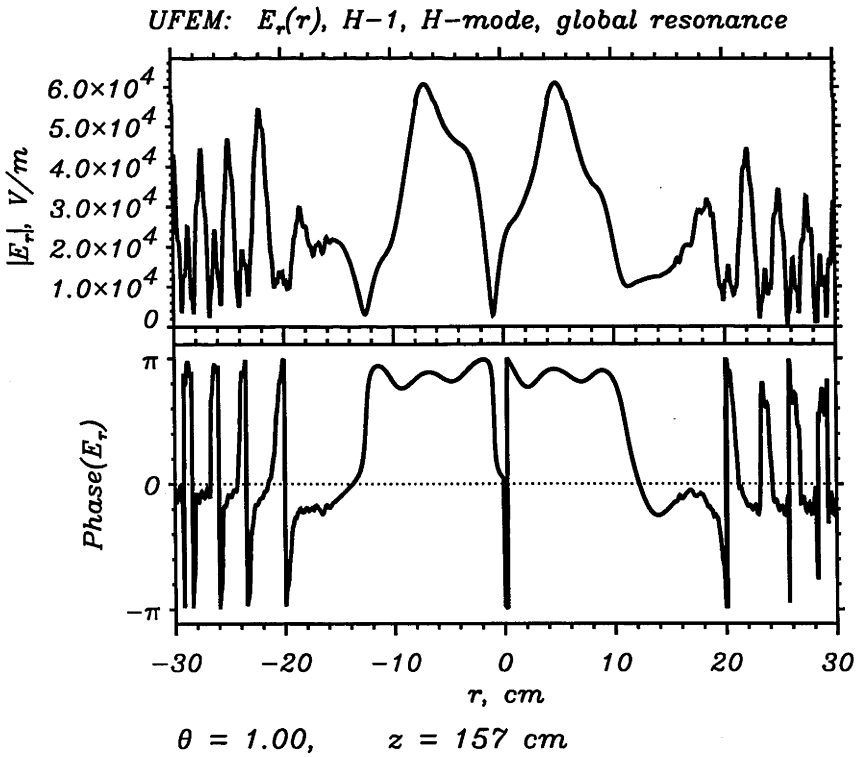

Figure 5.19: Radial profile of E_r for the case of Fig. 5.18.

m^{-1} in the center, and from Eq. (5.1), $E_{th} \approx 7.9$ kV/m which is 4 – 8 times lower than the wave amplitude in Fig. 5.19.

As a modification of the above hypothesis (which is probably more realistic), we can suggest that in the H-mode the system subsists on the first global eigenmode of the FW which becomes available in H-1NF with the rising density. The FW dissipation in H-1NF (at least in the present linear model) is low, and the "spike" on the R_{rad} vs. n_e scan corresponding to this resonance is sharp (compare, for example, R_{rad} in Figs. 5.16 and 5.18). Once the density reaches the "positive" slope part of the spike, the situation becomes "self-developing": the density rise results in the rise of R_{rad} which causes the increase of n_e, etc. The system quickly passes the maximum of $R_{rad}(n_e)$ and stabilizes at some point on the negative slope part of the curve. As discussed in § 2.3.3, such a point is stable because the density increase causes the R_{rad} to decrease, and the density drop results in an increase of R_{rad} (and hence, the ionization rate and the density rises back).

There is a lot of similarity between the "E"-to-"H" coupling mode transitions observed in the low density helicon source WOMBAT [48, 49, 54, 55] and the L – H mode transitions in H-1NF. When the density is low (no "global" eigenmodes of the FW available in the system), the antenna radiation resistance is low and the discharge is unstable (high level of fluctuations). Once the density becomes large enough so that the first possible ("global") eigenmode of the FW can be excited (in helicon sources this is commonly the mode $\{m{=}{+}1,\ N_r{=}1\}$ or $\{m{=}0,\ N_r{=}1\}$ depending on the antenna type), the system picks up this operational point and subsists on it stably within a certain region in the system parameter space (Chapter 3). Similarly to H-1NF, the antenna radiation resistance and the plasma density in "H" mode are significantly higher than in "E" mode [49] and the discharge is stable.

It is clear that the present linear model overestimates the wave amplitude at resonances (Figs. 5.14, 5.15 and 5.19) since it underestimates the wave damping; a proper account for the ion stochastic heating for example, would definitely lower the wave amplitude. In fact, the steady state amplitude can be right near the threshold of the stochastic heating (Eq. (5.1)). This can play the role of another stabilizing factor: once the wave amplitude rises above the E_{th}, an additional dissipation mechanism "switches on" causing it to decrease, and vice versa. Or the amplitude and the dissipation rate can be stabilized at a level above (but not very much) the threshold, since the stochastic ion heating efficiency is proportional to the wave amplitude unless $|\mathbf{E}| \gg E_{th}$ [81].

From this point of view, we can expect that:

- No similar L – H transitions should be observed if the plasma is formed and sustained by other means, for example by ECRH only.
- Numerous L – H (and possibly H – L) transitions will be observed as higher

order global eigenmodes will be excited at higher densities.

- The system behavior can be different at full ionization since the partial gas ionization is one of the main stabilizing factors for the H-mode.

Presently, there is very little experimental proof for any of the above hypotheses. Further experimental and theoretical investigation should answer the question of how the L – H mode transitions in H-1NF are related to the rf plasma formation and heating. Nevertheless, the author believes that this connection should be very close since the L – H transitions were only observed with rf system in operation, and since in this case, the rf heating is the primary factor determining the plasma condition.

Chapter 6

Summary, Conclusions, Further Development

6.1 Summary and Conclusions

We have employed the MHD numerical model (the FEM code) to study the antenna radiation resistance and the helicon wave dispersion in high density helicon sources. For such devices, the double saddle coil and the helical antenna have the highest R_{rad} for densities corresponding to optimum excitation of the m=+1 first radial mode. The double half-turn and helical antennas mainly excite the m=+1 mode, whilst the double saddle coil also well excites the m=+3 mode.

A double half-turn antenna has a low R_{rad} in small high density devices but a satisfactory R_{rad} in large (low density, low magnetic field) devices (§ 5.2). Experimentally it has the advantage that it can launch the $|m|$=1 modes with no constraints imposed by the antenna geometry on the k_z-spectrum. Recent experimental investigations of plasma formation using this antenna have demonstrated explicitly that a wider range of plasma conditions can be obtained than for a double saddle coil [48]. We emphasize however the importance of a series feed for all antennas in order to maximize the ratio of the R_{rad} to the matching network loss resistance.

We have numerically confirmed the well known experimental fact that in high density sources negative m modes are not efficiently excited, especially in small devices. The poor excitation of negative azimuthal modes is mainly due to the effect of the plasma density gradient. Consequently, an attempt to excite the m=–1 mode in BASIL by quadrature phasing of a pair of double saddle coils so as to eliminate the m=+1 mode has resulted in the excitation of the m=+3 mode instead of m=–1 [111].

We have numerically investigated the dependence of the R_{rad} of the double saddle coil on density. The R_{rad} is seen to reach a limiting value above densities where the first radial mode parallel wavelength of m=+1 approaches the antenna length. This

may explain the often observed experimental result that the plasma density attains a value that fixes the wavelength at about twice the antenna length for both double saddle coils and helical antennas [19, 97]. It is often observed for these antennas that the density rises in proportion to magnetic field in order to keep the helicon wavelength constant.

We have examined the effect of the density profile on the R_{rad}. Even though the shape of the R_{rad} spectrum is sensitive to the profile, for broad profiles the m=+1 mode radiation resistance is fairly constant. As the profile becomes steeper, the R_{rad} decreases, suggesting that the plasma formation process is inherently stable with respect to profile.

The helical antenna has an excellent directivity in high density sources when optimized for the m=+1 mode due to the fact that negative m modes are not efficiently excited. This is in good agreement with experiments and is linked to the fact that the helical antenna can form one-sided plasmas. We have also shown that the helical antenna excites wavefields of larger amplitudes (in the direction where $k_z > 0$) than the double saddle coil. We propose that the helical antenna is the best choice for a plasma source in which the antenna is to be located at one end of the plasma column. In large devices, the directivity of the helical antenna also appears to give the best chance of exciting the m=–1 mode separately.

The interference of several radial modes is shown to be responsible for axial beat patterns commonly observed in experiments. Radial modes higher than N_r=1, which may be unimportant in the spectrum of the antenna impedance, are observed to be nonetheless quite visible in the spectrum of the wavefield in the plasma center.

Detailed wavefield measurements performed in BASIL have confirmed that the helicon wave launched by both double saddle coil and helical antennas is composed mainly of the m=+1 first radial mode. For both antennas, good agreement was found between experimental measurements of the wave dispersion and the antenna radiation resistance and the results of the MHD numerical model. This justifies, to a certain extent, the neglect of finite electron mass (implying E_z=0) by the FEM code for those conditions. We also conclude that there are negligible power losses through parasitic effects in BASIL.

The numerical model was further upgraded so as to take into account parallel electron dynamics and, to a certain extent, other kinetic effects. The pollution-free finite element numerical scheme, formulated in terms of electromagnetic potentials and suitable for computations in the presence resonances in plasma, has been developed and realized in the UFEM code. The code has been successfully benchmarked with the code ISMENE 5 for four important frequency ranges, from Alfvén to above the lower hybrid.

Comparison between the MHD and kinetic models for BASIL conditions demonstrated that the MHD model is fairly accurate in the computation of the radia-

tion resistance and the helicon wave dispersion, however it underestimates the wave damping. Specifically, the MHD model does not account for the possibly large effect of the surface lower hybrid wave on energy deposition.

Modelling of the low density, low magnetic field helicon plasma sources WOMBAT and HARE [52], using UFEM code, demonstrated that both helicon and Trivelpiece-Gould waves are important in such devices. The m=–1 mode can be excited in low density plasmas almost as well as m=+1, but the m=–1 wavefield corresponds to longer wavelengths and higher phase velocities. TG modes were found to be responsible for the deposition of a significant fraction of rf power in the plasma periphery near the antenna.

The application of UFEM code to model the rf plasma heating in H-1NF heliac demonstrated that the L – H transitions in H-1NF could be linked to the excitation of global eigenmodes of the fast wave. First global eigenmodes were found in the code for conditions close to the system parameters when L – H transitions were observed experimentally. It was also demonstrated that an operational point close to the eigenmode can be stable, first of all due to partial gas ionization, and that the ion stochastic heating can be very efficient for those conditions.

The UFEM code has proven to be a useful tool for the investigation of rf wave physics in low temperature current-free cylindrical plasmas. Work with the code is only beginning and promises interesting findings in the near future.

This study is but a first, simple step toward a complete understanding and quantification of the helicon discharge physics.

6.2 Further Development

In this Section we consider a possible strategy to develop a 3D ICRH [1] code which could be applicable for stellarators (paying special attention to the H-1NF) and tokamaks.

It is also becoming clear that the proper account for the real system geometry is important for low density, low field helicon sources. For example, an attempt to model such a source HARE [52] by the UFEM code yielded an agreement with experimentally obtained data which was not satisfactory (this could partially be attributed to possible experimental mistakes, but not completely), indicating the need for a more sophisticated and more adequate modelling for such devices which are commonly at least 2-dimensional. Particularly in HARE [52], the "antenna region" tube (b = 10.2 cm) is rather short (L = 30.5 cm) and followed by a small

[1]For the sake of simplicity, the whole [Alfvén – LH] frequency range will be often referred to as the "ICRH" in this Section, despite the fact that it is actually much broader than the conventional frequency range for Ion Cyclotron Resonance Heating.

diffusion chamber having $b = 16$ cm and $L = 30$ cm. The external magnetic field and the plasma density vary up to 2 — 3 times over the device length.

As mentioned in § 5.3, the code UFEM can only be applied for a qualitative analysis in the case of H-1NF. From the point of view of a theorist, the heliac is a fully 3D machine. The proper account for the 3D heliac geometry may result in a significant change of the eigenmode spectra, compared to the "periodic cylinder", and of the wave dissipation, due to several specifically 3D effects such as the toroidal and poloidal mode coupling. To the best of the author's knowledge however, there are no codes directly applicable to ICRH modelling in H-1NF. In particular, little work in global wave codes has been performed to model waves in the LH range. The real ICRH system in the H-1NF operates for frequencies from below ω_{ci} up to (and above) the LHR, while no one existing or proposed code covers this frequency range. Recently, a 3D ICRH code STELION [136] has been developed. However,

- STELION is still not well trusted. Partially, because it is currently the only 3D ICRH code in the world, hence its full benchmarking is still incomplete.

- The frequency range for which STELION is definitely applicable is limited to [1 – several]$\times\omega_{ci}$, while the frequency range employed in the experiments in H-1NF is much broader: [Alfvén – LH]. The divergence-free finite difference discretization scheme in terms of $\mathbf{E}$ employed in STELION is quite suitable for weak resonances, such as ion-ion hybrid or ion minority cyclotron resonance in the case of a strong dissipation in hot dense thermonuclear plasma, but it is difficult to use it in the case of strong resonance (such as the LHR), especially in the case of weak dissipation, without facing the numerical pollution problem.

- It is unclear whether STELION can be easily modified so that to place an antenna into the plasma, which is its operational condition in H-1NF (§ 5.3).

- The "reduced order" form of plasma dielectric tensor [120] employed in STELION is a kind of WKB approximation, since it requires the solution of the local dispersion relation to separate the fast wave. In fact, it is only well applicable in large devices, while the vast majority of experimental devices in the world are small- and medium- size (including the H-1NF).

- STELION can only use magnetic configurations with nested magnetic surfaces, while in the H-1NF (and other stellarators) magnetic islands are very common.

All these problems can be resolved by means which are significantly simpler than those employed in STELION (and some other 2D and 2.5D codes).

At first sight, the straightforward 3D finite element discretization in real space seems to be the most natural way to create a 3D code. However, it is extraordinarily time- and work- consuming. In addition, present day computers can provide only a

coarse numerical resolution for this scheme, and such resolution may appear to be incompatible with the short wavelength plasma oscillations (such as LH waves) to be studied.

Another possible approach which should be more realistically achievable in reasonable time, is to use a Fourier-decomposition in toroidal and poloidal angles for the field, the plasma dielectric tensor and other terms in the equations (similarly to [120]) which results in a system of 1D differential equations for the "radial" coordinate. Thus, the 3D task is effectively being reduced to 1D. Commonly, in medium-size devices not many toroidal and poloidal modes are efficiently excited, which results in a considerable reduction of required computer resources. However, there is a price to pay: the resulting system of equations is mode-coupled over both toroidal and poloidal modes and its convergence properties with respect to the number of modes (which is always limited in real computations) should be further studied. On the other hand, the same approach was adopted, for example, in [120], in the code STELION [136] and 3D stability code TERPSICHORE [4] and it was found that this problem is commonly not very significant.

Such a code could be relatively easily interfaced with the standard 3D equilibrium code VMEC [66] to obtain the plasma equilibrium quantities. The presence of the wave vectors, due to the Fourier-decomposition, also makes the incorporation of kinetic damping mechanisms through the plasma dielectric tensor straightforward and natural.

The advantages of using the electromagnetic potentials, $\{\mathbf{A},\phi\}$, are discussed in § 4.3. It is particularly important for a 3D code that in this case the matrix in the linear system is usually so well conditioned [73] that it enables the application of fast iterative algorithms requiring much less computer memory and time than the standard Gaussian elimination. (There is also an idea, which deserves to be studied, to employ a conformal transformation, preserving Maxwell's equations, to the $(\mathbf{A},\phi)$ field in order to realize a simplified change of geometry from a cylindrical one to a heliac-like bean shape, if such a transformation can be found.)

The coordinate system used together with the above Fourier-transform in the codes STELION [136] and TERPSICHORE [4] are the so-called "flux coordinates" in which the "radial" coordinate is the magnetic surface number [138]. This yields a non-orthogonal coordinate system which makes the analytic and programming work very complicated and cumbersome. The advantage of using the flux coordinates is that the wave equations contain only first derivatives over the "radial" coordinate. However, this is not a large advantage when one uses the $(\mathbf{A},\phi)$-technique because the variational form in it (Eq. (4.29)) contains only the first derivatives anyway. Hence, it would be easier to construct an *orthogonal* coordinate system. In particular, if there is a vacuum gap between the plasma and the conducting wall, it can be constructed in a conventional way [74, 138] so that the last pseudo-flux surface

coincides with the conducting wall. Specifically for the H-1NF, common *straight toroidal coordinates* can be used in the 1st approximation (since there is, strictly speaking, no conducting shell surrounding plasma in H-1NF). Moreover, the $r = 0$ can be placed in the central conductor thus eliminating any problems with the singular wave behavior on the magnetic axis. Further, since it is not necessary to follow nested magnetic surfaces in this approach, magnetic islands can be treated as well.

To model the plasma, it is possible and necessary to use the "full physics" plasma dielectric tensor derived in [30] and used in the codes ISMENE [7, 133] and PENN [74]. Despite having a complicated form (the dielectric tensor becomes a differential operator), it contains all the linear wave physics relevant to the H-1NF conditions, particularly, all kinds of kinetic effects, including the FLR effects up to the second order, and linear mode conversion. Since it also accounts for the plasma current, such a code can be used for tokamaks as well. The use of the "reduced order" form of the dielectric tensor in STELION [120, 136] was, probably, prompted by the evaluation of supercomputer resources available about 2 years ago. In practice, the development of supercomputers is nowadays so rapid that it is quite possible to use the VPP300 supercomputer installed at the ANU Supercomputer Facility to model medium-size devices, such as H-1NF, without any oversimplifying assumptions. Moreover, unlike the finite difference discretization scheme employed in STELION, the finite element method allows the short-wavelength slow wave structure to be underresolved without the algorithm divergence at the resonance. Commonly, in such a case, the antenna coupling and the global wavefield and power deposition structure are not affected, except near the thin resonance layer. Further, the application of cubic Hermite finite elements (as, for example, in [7]), though more difficult to program compared to standard linear ones, enables one to speed up the code and reduce the memory consumption up to 4 times, and simultaneously eliminates problems with accurate numerical differentiation of potentials in the computation of electric and magnetic fields and improves the wavefield behavior on the magnetic axis (§ 4.5).

So, the best approach to the creation of a 3D ICRH code suitable for H-1NF would probably be the combination of Fourier-decomposition in orthogonal coordinates with the finite element discretization in terms of $(\mathbf{A},\phi)$ with the use of cubic Hermite finite elements and the use of the "full physics" plasma dielectric tensor [30]. This approach however also requires a lot of analytic and programming work. To a certain extent, it can be facilitated by the use of symbolic manipulation software, such as the MAPLE language [32].

Appendix A

Different System Geometries

In this Section we describe how 4 different system geometries can be treated in the same numerical algorithm.

Having solved the wave equations for separate k_z-modes of the wave field, $\sim \exp(ik_z z)$, it is not difficult to describe an infinite plasma cylinder, a plasma cylinder bounded by conducting plates at one or both ends, or approximately model toroidal geometry by a periodic cylinder. We will demonstrate how this can be accomplished through manipulation of the k_z-harmonics of the wave field and the antenna current and charge.

In all cases below, we take Fourier-transforms of various functions so that inverse Fourier-transforms are simply sums (for discrete k_z-spectra) or integrals (for continuous k_z-spectra) over all k_z-modes.

(A) Infinite cylinder. This is the "basic" geometry for the algorithm. This model is adequate when the plasma cylinder is long enough, waves are sufficiently damped along z so that there is no reflection from the cylinder ends. The k_z-spectrum is continuous. The Fourier-transform over z is

$$\mathbf{j}(k_z) = \frac{1}{2\pi} \int_{-\infty}^{+\infty} e^{-ik_z z} \mathbf{j}(z) dz \ , \tag{A.1}$$

and the inverse Fourier-transform,

$$\mathbf{j}(z) = \int_{-\infty}^{+\infty} e^{ik_z z} \mathbf{j}(k_z) dk_z \ . \tag{A.2}$$

In Eqs. (A.1), (A.2) $\mathbf{j}$ can be the antenna current, charge or any wavefield component.

The origin of the coordinate system in this transform, $z = 0$, we define as the *antenna geometric center* (AGC) (In fact, this point can be arbitrary; note however that the Fourier-transforms presented in Appendix B for different antennas

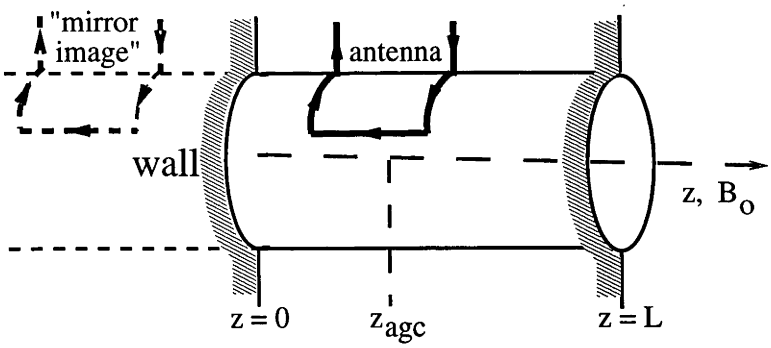

Figure A.1: Plasma cylinder bounded by a conducting wall at $z = 0$ (cases (C) and (D)) and at $z = L$ (case (C) only).

are expressed with respect to the real antenna geometric centers at $z = 0$; in this case formulae are usually simpler.)

(B) Cylinder with equalized ends ("torus"). We can partially account for toroidicity by equalizing the cylinder ends, i.e. using the periodic boundary condition, $A(z) = A(z + 2\pi n R_{tor})$, where A is any value, R_{tor} is the torus major radius and n is any integer number. This yields the discrete k_z-spectrum, $k_{z(n)} = n/R_{tor}$. The $z \leftrightarrow k_z$ Fourier-transforms in this case are

$$\mathbf{j}(k_{z(n)}) = \frac{1}{2\pi R_{tor}} \int_0^{2\pi R_{tor}} e^{-ik_{z(n)}z} \mathbf{j}(z) dz \ , \tag{A.3}$$

$$\mathbf{j}(z) = \sum_n e^{ik_{z(n)}z} \mathbf{j}(k_{z(n)}) \ . \tag{A.4}$$

Again, in Eqs. (A.3) and (A.4), $\mathbf{j}$ can be the antenna current, charge or any wavefield component.

(C) Finite-length cylinder. The plasma cylinder is bounded by conducting plates at both ends. Axial eigenmodes can be excited in the system due to wave reflection from the ends. For this case we place the coordinate system origin, $z = 0$, at one of the cylinder ends, the AGC at $z = z_{agc}$ and another conducting boundary at $z = L$ (Fig. A.1). ($z = 0$ can be chosen at any one of the conducting plates. Note also that as we take the positive direction of z coinciding with the external magnetic field, $\mathbf{B}_0$, both z_{agc} and L can be either positive or negative, depending on the direction of $\mathbf{B}_0$.)

To satisfy the boundary conditions at $z = 0$ and $z = L$,

$$\{E_r, E_\theta, B_z\}|_{z=0} = \{E_r, E_\theta, B_z\}|_{z=L} = 0 \ ,$$

we have to Fourier-expand $\{E_r, E_\theta, B_z\}(z)$ in discrete series of $\sin(k_{z(n)}z)$ [57],

$$\{E_r, E_\theta, B_z\}(z) \sim \sum_n \sin(k_{z(n)}z) \dots \ , \tag{A.5}$$

$$k_{z(n)} = \frac{\pi n}{L}\,, \qquad n = 0,\ 1,\ 2,\ \ldots\ .$$

The analysis of Maxwell's equations shows that other functions must be Fourier-expanded as follows,

$$\begin{aligned} \{j_r, j_\theta, \rho\}(z) &\sim \sum_n \sin(k_{z(n)} z) \ldots\ , \\ \{E_z, B_r, B_\theta, j_z\}(z) &\sim \sum_n \cos(k_{z(n)} z) \ldots\ , \end{aligned} \tag{A.6}$$

where $\mathbf{j}$ and ρ are the antenna current and charge.

We can further split $\sin(k_{z(n)}z)$ and $\cos(k_{z(n)}z)$ into $\exp(\pm i k_{z(n)} z)$ to obtain the "standard" representation of the Fourier-expansion. Note that in this case, the resulting spectrum is formally equivalent to the k_z-spectrum of the "torus" (Eq. (A.4)) if we take $R_{tor} = L/\pi$ and an equal number of positive and negative n-modes.

(D) Half-infinite cylinder. In helicon plasma sources, it is often the case that an antenna is placed not far from a conducting plate at the end of the cylinder. Here we must take into account the possibility of wave reflection from this plate. However, the plasma is long enough in one direction ($z > 0$ or $z < 0$) so that the reflection from the other end can be neglected.

As for the finite-length cylinder (C), we place $z = 0$ at the conducting plate (Fig. A.1). The Fourier-expansion of variables is analogous to case (C), Eqs. (A.5), (A.6), but the k_z-spectrum is continuous,

$$\begin{aligned} \{E_r, E_\theta, B_z, j_r, j_\theta, \rho\}(z) &\sim \int dk_z \{\sin(k_z z) \ldots\}\ , \\ \{E_z, B_r, B_\theta, j_z\}(z) &\sim \int dk_z \{\cos(k_z z) \ldots\}\ , \end{aligned} \tag{A.7}$$

and we can also split $\sin(k_z z)$ and $\cos(k_z z)$ into exponents, as for the case (C). Note that the use of the expansion (A.7) is equivalent to having an "antenna mirror image" at $z = -z_{agc}$ in an infinite cylinder (Fig. A.1), so that

$$\begin{aligned} \{j_r, j_\theta, \rho\}(-z) &= -\{j_r, j_\theta, \rho\}(z)\ , \\ j_z(-z) &= j_z(z)\ . \end{aligned}$$

We will formulate the results of this analysis into a set of rules which are easily programmable and allow us to include all four system geometries into the one code, once the wave equations are solved for separate k_z-modes of the type $\sim \exp(i k_z z)$. (The rigorous proof of these rules is cumbersome but trivial, and we will not reproduce it here.)

- In the inverse Fourier-transform (obtaining the wave fields in real space, the antenna impedance, etc.) we take the integral over k_z for continuous spectra (cases (A) and (D)) and the sum over discrete k_z-modes, $\sum_n$, for discrete spectra (cases (B) and (C)).

- We can treat the spectrum for the finite-length cylinder (C) as a spectrum of a "torus" (B), $k_{z(n)} = n/R_{tor}$, with $R_{tor} = L/\pi$ and equal number of positive and negative n-modes.

- We can always use Eq. (A.1) for the computation of the Fourier-transforms of antenna currents and charges with respect to the AGC regardless of the type of spectrum and system geometry. The z-integration in Eq. (A.1) is always performed over the *finite* antenna z-length. For a bounded cylinder (cases (C) and (D)) we must further make the transformation of the antenna currents and charges in Fourier space,

$$\begin{aligned} \{j_r, j_\theta, \rho\}(k_z) &= \exp(-ik_z z_{agc})\{j_r^o, j_\theta^o, \rho^o\}(k_z) \\ &- \exp(ik_z z_{agc})\{j_r^o, j_\theta^o, \rho^o\}(-k_z) \ , \\ j_z(k_z) &= \exp(-ik_z z_{agc}) j_z^o(k_z) + \exp(ik_z z_{agc}) j_z^o(-k_z) \ , \end{aligned} \tag{A.8}$$

  where $\{j_r^o, j_\theta^o, j_z^o, \rho^o\}(k_z)$ are obtained, using Eq. (A.1), with respect to the AGC. (The transforms (A.8) reflect the z-shift of the $z = 0$ point in the cases (C) and (D).)

  For the discrete spectra (cases (B) and (C)) we must also account for an additional factor $1/R_{tor}$ in the Fourier-transforms of antenna currents and charges (Eq. (A.3)).

- For a bounded cylinder (cases (C) and (D)) the k_z-spectrum must be strictly anti-symmetric, $k_{z(-n)} = -k_{z(n)}$, with equal number of positive ($n > 0$) and negative ($n < 0$) modes. All values involving the integration over the entire system z-length (such as the antenna impedance, the electromagnetic energy flux, $P_r(r)$, or the total power deposition, $Q(r)$, § 4.4), and which we can split into k_z-modes, in cases (C) and (D) must be reduced by a factor of two (in case (D) this simply means the elimination of the "antenna mirror image").

Appendix B

Antennas; Fourier-Transforms of Antenna Currents and Charges

In this Section we describe the antennas used in this thesis and present the Fourier-transforms of the antenna currents and charges for them. All antenna types discussed below have been pre-programmed in the code UFEM (Appendix C). In Appendix A we also demonstrate how these Fourier-transforms can be used in 4 different system geometries.

The Fourier-transform,

$$\mathbf{j}(r,m,k_z) = \frac{1}{4\pi^2}\int_0^{2\pi} d\theta \int dz \cdot \mathbf{j}(r,\theta,z)\exp\{-i(m\theta + k_z z)\}\ , \qquad \text{(B.1)}$$

is performed in the coordinate system with the origin placed in the *antenna geometric center* (see also Appendix A). The position of $\theta = 0$ in the whole system coincides with its position with respect to a specific antenna. The integration over z in Eq. (B.1) is always performed over the *finite* z-length of the antenna.

For 3 antenna types below ((A), (B) and (F)) we consider the **charge distribution** along the antenna length ($\nabla \cdot \mathbf{j} \neq 0$); other antennas are divergence-free. For these antennas we will compute $\nabla \cdot \mathbf{j}$ which is proportional to the antenna charge density, $\rho = -i(\nabla \cdot \mathbf{j})/\omega$. To model the charge distribution, we assume that the antenna current is distributed as $\sim \cos(\tilde{\beta}x)$, where x is the distance along the antenna azimuthal and axial elements located near the plasma from the input to the output feeder (x varies from 0 to $\tilde{l}$), and $\tilde{\beta}$ is the "current propagation constant". The current in the radial elements (feeders) is assumed constant. The complex parameter $\tilde{\beta}$ can be calculated if we consider the above antenna elements as an "electrically long" line with distributed parameters,

$$\tilde{\beta} = \frac{1}{\tilde{l}}\sqrt{\omega C(\omega L - iR)}\ ,$$

where C is the antenna–plasma capacitance, L is the antenna inductance, and R is its Ohmic resistance, all per unit length. Often $\omega L \gg R$ and $\tilde{\beta}$ is real, $\tilde{\beta} = \omega\sqrt{LC}/\tilde{l}$.

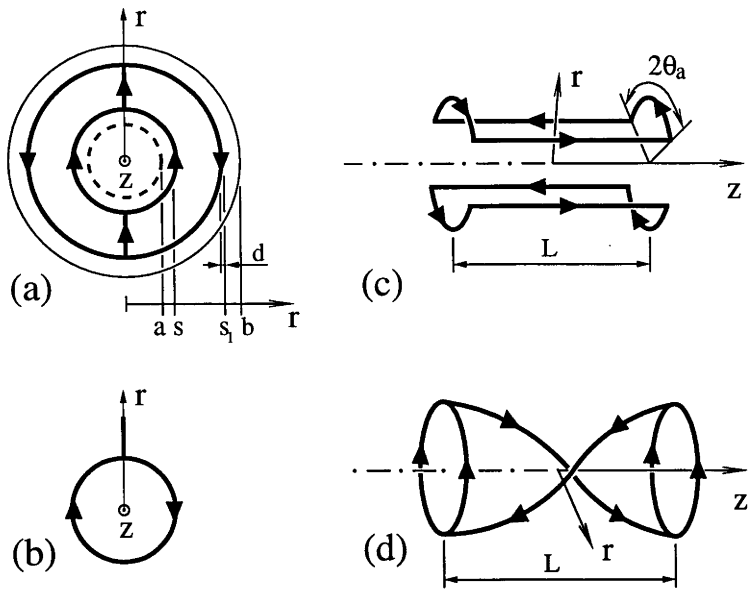

Figure B.1: 4 antenna types: (a) double half-turn antenna, (b) single (m=0) loop, (c) double saddle coil, (d) $\lambda/2$ helical antenna. Radius-vector designates the position of $\theta = 0$. The system radial dimensions [shown for (a)]: a is the plasma edge radius, s is the radius of the inner antenna edge, d is the radial thickness of antenna wire, s_1 is the radius of the outer antenna edge (for the double half-turn antenna only) and b is the conducting wall radius. L is the antenna length (for double saddle coil and helical antenna).

$\tilde{\beta}$ can also be evaluated if we know the amplitude and the phase difference between the input and output currents measured experimentally. $\tilde{\beta} = 0$ means a divergence-free antenna, i. e. no charge.

Four antenna types are shown in Fig. B.1. We also employ the notation of § 2.2 and Fig. B.1 for the antenna geometric parameters. We always consider the antenna wire to have a finite radial thickness d, while (except for antenna type (E) below) its axial (z-) thickness is expressed by a Dirac δ-function. We also introduce the following designations:

$$U(x_1 \le x \le x_2) = \begin{cases} 1 & \text{if} \quad x_1 \le x \le x_2 \\ 0 & \text{otherwise} \end{cases} ,$$

$$D(r) = \frac{U(s \le r \le s+d)}{d} ,$$

(s is the radius of inner antenna edge, Fig. B.1(a)), and $l = L/2$ is the half of the total antenna axial length. The total antenna current is assumed to be unity.

(A) Double half-turn antenna [Fig. B.1(a)]. For this antenna $j_z = 0$ and we take $\nabla \cdot \mathbf{j} = 0$ (the case $\nabla \cdot \mathbf{j} \neq 0$ for the modification of this antenna is considered below). The spatial distribution of the antenna current density is

$$\begin{cases} j_r(r,\theta,z) = \dfrac{f_r(r)}{r}\{\delta(\theta) - \delta(\theta-\pi)\}\delta(z) \\ \\ j_\theta(r,\theta,z) = \dfrac{f_\theta(r)}{2}\{U(-\pi \le \theta \le 0) - U(0 \le \theta \le \pi)\}\delta(z)\ , \end{cases}$$

where

$$f_r(r) = \begin{cases} (r-s)/d & \text{if} \quad s \le r \le s+d, \\ 1 & \text{if} \quad s+d < r < s_1 - d, \\ (s_1 - r)/d & \text{if} \quad s_1 - d \le r \le s_1, \\ 0 & \text{elsewhere}\ , \end{cases} \tag{B.2}$$

and

$$f_\theta(r) = D(r) - \frac{U(s_1 - d \le r \le s_1)}{d}\ , \qquad \frac{d}{dr} f_r(r) = f_\theta(r)\ . \tag{B.3}$$

This yields

$$\begin{cases} j_r(r,m,k_z) = \dfrac{f_r(r)}{2\pi^2 r} \\ \\ j_\theta(r,m,k_z) = \dfrac{i}{2\pi^2 m} f_\theta(r) \qquad \text{for} \quad m = \ \pm 1,\ \pm 3,\ \pm 5, \ldots \end{cases}$$

and

$$j_r(r,m,k_z) = j_\theta(r,m,k_z) = 0 \qquad \text{for} \quad m = 0,\ \pm 2,\ \pm 4, \ldots\ .$$

As a **variation** of this antenna type we also consider the double half-turn antenna with the outer loop outside the conducting wall, $s_1 - d > b$ [Fig. B.1(a)], which we also sometimes refer to as the "*Degeling antenna*" [48]. For such an antenna we consider $\nabla \cdot \mathbf{j} \neq 0$: the current is distributed as $\sim \cos[\gamma(\theta - \pi)]$ along the azimuthal elements of the inner loop, where $\gamma = \tilde{\beta} s$ and $\tilde{\beta}$ is the "current propagation constant" described above. The spatial current distribution is then

$$\begin{cases} j_r(r,\theta,z) = \dfrac{f_r(r)}{r}\{\cos(\gamma\pi)\delta(\theta) - \delta(\theta-\pi)\}\delta(z) \\ \\ j_\theta(r,\theta,z) = \dfrac{D(r)}{2}\cos[\gamma(\theta-\pi)]\{U(-\pi \le \theta \le 0) - U(0 \le \theta \le \pi)\}\delta(z)\ . \end{cases}$$

This yields

$$\begin{cases} j_r(r,m,k_z) = \dfrac{f_r(r)}{r}\alpha \\ \\ j_\theta(r,m,k_z) = -iD(r)\dfrac{m}{\gamma^2-m^2}\alpha \\ \\ \nabla\cdot\mathbf{j}(r,m,k_z) = \dfrac{D(r)}{r}\dfrac{\gamma^2}{\gamma^2-m^2}\alpha \qquad \text{for } \gamma^2 \neq m^2 \ , \end{cases}$$

where

$$\alpha = \frac{1}{4\pi^2}[\cos(\gamma\pi) - (-1)^m] \ ,$$

and

$$j_r(r,m,k_z) = j_\theta(r,m,k_z) = \nabla\cdot\mathbf{j}(r,m,k_z) = 0 \qquad \text{for } \gamma^2 = m^2 \ .$$

(B) Single loop which for $\nabla\cdot\mathbf{j}=0$ becomes the $\mathbf{m=0}$ **loop**, [Fig. B.1(b)]. For this antenna $j_z = 0$, and we also consider $\nabla\cdot\mathbf{j}\neq 0$ with j_θ distributed as $\sim\cos(\gamma\theta)$ along the loop, where $\gamma = \tilde{\beta}s$,

$$\begin{cases} j_r(r,\theta,z) = -\dfrac{f(r)}{r}\delta(\theta)\delta(z)\Delta \\ \\ j_\theta(r,\theta,z) = D(r)\cos(\gamma\theta)\delta(z) \ , \end{cases}$$

where $\Delta = 1-\cos(2\pi\gamma)$ is the current in the radial "feeder", and

$$f(r) = \begin{cases} 0 & \text{if} \quad r < s \\ (r-s)/d & \text{if} \quad s \le r \le s+d \\ 1 & \text{if} \quad r > s \end{cases} \ , \qquad \frac{d}{dr}f(r) = D(r) \ . \tag{B.4}$$

For $\tilde{\beta}\neq 0$ and $\gamma^2 \neq m^2$ this yields

$$\begin{cases} j_r(r,m,k_z) = -\dfrac{f(r)\Delta}{4\pi^2 r} \\ \\ j_\theta(r,m,k_z) = \dfrac{D(r)}{4\pi^2}\dfrac{1}{\gamma^2-m^2}\{\gamma\sin(2\pi\gamma) + im\Delta\} \\ \\ \nabla\cdot\mathbf{j}(r,m,k_z) = \dfrac{D(r)}{4\pi^2 r}\dfrac{\gamma}{\gamma^2-m^2}\{im\sin(2\pi\gamma) - \gamma\Delta\} \ . \end{cases}$$

For $\gamma^2 = m^2 \neq 0$

$$\begin{cases} j_r(r,m,k_z) = 0 \\ \\ j_\theta(r,m,k_z) = \dfrac{D(r)}{4\pi} \\ \\ \nabla\cdot\mathbf{j}(r,m,k_z) = \dfrac{im}{r}j_\theta(r,m,k_z) \ . \end{cases}$$

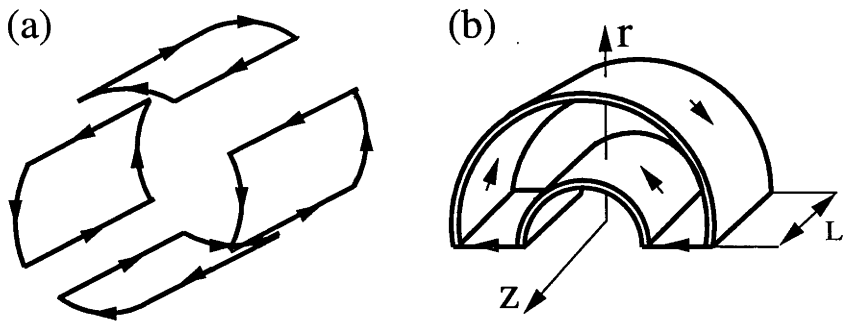

Figure B.2: (a) The phased array of two double saddle coils. The current in the side coils is proportional to the factor $e^{i\varphi}$ (φ is the phase difference); the direction of currents is shown for $\varphi = 0$. (b) Half-turn antenna, (E).

Note that this axisymmetric antenna can launch modes $m \neq 0$ if $\nabla \cdot \mathbf{j} \neq 0$.

And finally, for $\tilde{\beta} = 0$ (the $m = 0$ loop),

$$\begin{aligned} j_r(r,m,k_z) &= \nabla \cdot \mathbf{j}(r,m,k_z) = 0, \\ j_\theta(r,m,k_z) &= \begin{cases} D(r)/2\pi & \text{for} \quad m = 0 \\ 0 & \text{for} \quad m \neq 0 \, . \end{cases} \end{aligned}$$

(C) Double saddle coil [Fig. B.1(c)]. The angular half-width of an azimuthal element, θ_a, is typically $\pi/4$. For $\theta_a = \pi/2$ it becomes the **Nagoya type III** antenna [95]. For this antenna we consider $\nabla \cdot \mathbf{j} = 0$ only. $j_r = 0$, j_θ and j_z are connected through the condition $\nabla \cdot \mathbf{j} = 0$, so it is enough to consider, for example, j_z only.

$$\begin{aligned} j_z(r,\theta,z) = \; & \frac{D(r)}{r} U(-l \leq z \leq l) \{ \delta(\theta + \theta_a) - \delta(\theta - \theta_a) \\ & + \delta(\theta - \pi - \theta_a) - \delta(\theta - \pi + \theta_a) \} \, , \end{aligned}$$

$$\begin{cases} j_z(r,m,k_z) = i \dfrac{2D(r)}{\pi^2 r} \sin(m\theta_a) \dfrac{\sin(k_z l)}{k_z} \\ \\ j_\theta(r,m,k_z) = -\dfrac{r k_z}{m} j_z(r,m,k_z) \qquad \text{for} \quad m = \pm 1, \; \pm 3, \ldots \end{cases} \tag{B.5}$$

and $j_\theta(r,m,k_z) = j_z(r,m,k_z) = 0$ for $m = 0, \; \pm 2, \; \pm 4, \ldots$. (The appropriate limit should be taken in Eqs. (B.5) for $k_z = 0$.)

For **2 phased double saddle coils** rotated 90^o with respect to each other (Fig. B.2(a)) having the phase difference φ between their currents, the Fourier-transform can be obtained from Eqs. (B.5) if we formally make the replacement

$$i \rightarrow i + e^{i\varphi} \sin\left(m \frac{\pi}{2}\right) \, .$$

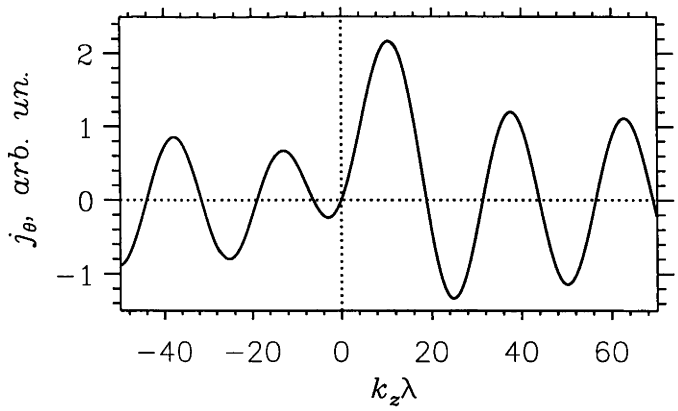

Figure B.3: k_z-spectrum of j_θ for $\lambda/2$ helical antenna (Fig. B.1(d)) for m=+1 mode.

Obviously, $\varphi = -\pi/2$ eliminates the $m = +1$ mode from the spectrum,

$$j_\theta(r, m = 1, k_z) = j_z(r, m = 1, k_z) = 0 \ ,$$

so this antenna has been used to separate the excitation of m=+1 and m=−1 [112].

(D) Helical antenna [Fig. B.1(d)]. For this antenna we consider an arbitrary relation between length L and the length of one turn of a helical winding λ. We also consider $\nabla \cdot \mathbf{j} = 0$ only. $j_r = 0$,

$$\begin{aligned} j_\theta(r,\theta,z) &= D(r)\Big[U(-l \le z \le l)[\delta(z+\beta\theta) - \delta(z+\beta\theta+\lambda/2)] \\ &+ \frac{1}{2}\delta(z-l)[U(-\theta_0-\pi \le \theta \le -\theta_0) - U(-\theta_0 \le \theta \le -\theta_0+\pi)] \\ &+ \frac{1}{2}\delta(z+l)[U(\theta_0 \le \theta \le \theta_0+\pi) - U(\theta_0-\pi \le \theta \le \theta_0)]\Big] \ , \end{aligned}$$

where $\theta_0 = l/\beta$ and $\beta = \lambda/2\pi$. This yields

$$\begin{cases} j_z(r,m,k_z) = -\dfrac{D(r)}{\pi^2 r}\dfrac{\sin(\gamma l)}{\gamma} \\ \\ j_\theta(r,m,k_z) = -\dfrac{rk_z}{m} j_z(r,m,k_z) \qquad \text{for} \quad m = \ \pm 1, \ \pm 3, \dots \ , \end{cases} \tag{B.6}$$

where $\gamma = k_z - 2\pi m/\lambda$ (for $\gamma = 0$ the appropriate limit in Eq. (B.6) must be taken), and

$$j_\theta(r,m,k_z) = j_z(r,m,k_z) = 0 \qquad \text{for} \quad m = 0, \ \pm 2, \ \pm 4, \dots . \tag{B.7}$$

Figure B.3 demonstrates the k_z-spectrum of j_θ for $\lambda/2$ helical antenna ($L = \lambda/2$, Fig. B.1(d)) for m=+1. The absolute maximum of $|j_\theta|$ is reached at $k_z\lambda \approx 10.5$. The latter relation was used in Chapter 2 for the optimization of $\lambda/2$ helical antenna for a specific k_z-mode of m=+1.

This antenna has a positive helicity which is demonstrated by the relation

$$\{j_\theta, j_z\}(m, -k_z) = \{j_\theta, j_z\}(-m, k_z) \ ,$$

which means that if, for example, some positive k_z is dominant for m=+1 in the antenna spectrum, the same modulus negative k_z is dominant for m=–1.

In this antenna (Fig. B.1(d)) there are two antiphased azimuthal elements at each end of the antenna. A **variation** of this antenna type which has **only one** azimuthal element at both ends [112] and which was employed in the experimental study discussed in Chapter 3 has exactly the same spectrum, Eqs. (B.6, B.7), but $j_\theta(r, m, k_z)$ has an additional non-zero harmonic $m = 0$:

$$j_\theta(r, m = 0, k_z) = i\frac{D(r)}{2\pi}\sin(k_z l) \ .$$

(E) Half-turn antenna of finite axial length L [Fig. B.2(b)]. With the outer half-loop ("return conductor") placed outside the system conducting boundary it becomes a single-strip $\Delta\theta = \pi$ antenna with radial feeders. $j_z = \nabla \cdot \mathbf{j} = 0$,

$$\begin{cases} j_r(r, \theta, z) = \dfrac{f_r(r)}{r}\left\{\delta\left(\theta - \dfrac{\pi}{2}\right) - \delta\left(\theta + \dfrac{\pi}{2}\right)\right\} U(-l \le z \le l) \\ \\ j_\theta(r, \theta, z) = f_\theta(r) U\left(-\dfrac{\pi}{2} \le \theta \le \dfrac{\pi}{2}\right) U(-l \le z \le l) \end{cases} ,$$

where $f_r(r)$ and $f_\theta(r)$ are given by Eqs. (B.2, B.3) (we use the same designations as for the double half-turn antenna (A), Fig. B.1(a)).

$$\begin{cases} j_r(r, m, k_z) = -\dfrac{i}{\pi}\dfrac{f_r(r)}{r}\sin\left(\dfrac{m\pi}{2}\right) F(k_z) \\ \\ j_\theta(r, m, k_z) = f_\theta(r) F(k_z) G(m) \ , \end{cases}$$

where

$$F(k_z) = \frac{\sin(k_z l)}{2\pi k_z l}$$

($F(k_z) = 1/2\pi$ for $k_z = 0$) and

$$G(m) = \begin{cases} \dfrac{1}{m\pi}\sin\left(\dfrac{m\pi}{2}\right) & \text{for} \quad m \neq 0 \\ \\ 1/2 & \text{for} \quad m = 0 \ . \end{cases}$$

(F) H1–type double saddle coil [Fig. B.4]. The double saddle coil employed in the toroidal heliac H1–NF [16] is different from the double saddle coil (C): 2 axial

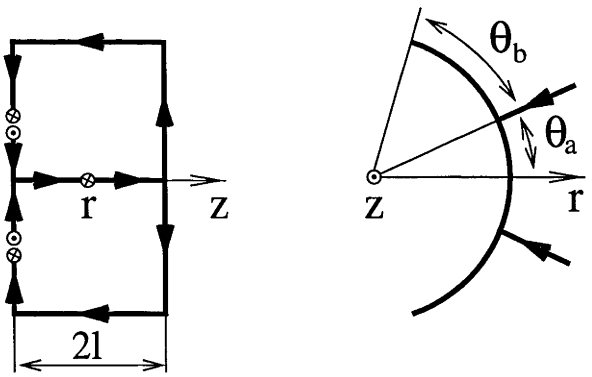

Figure B.4: The model of the double saddle coil used in H1–NF toroidal heliac [16].

elements (in the center) are close to each other, so in our model we join them for simplicity. This antenna is "electrically long", so it is important to account for the charge distribution ($\nabla \cdot \mathbf{j} \neq 0$). The current in the radial feeders is non-zero. Using the above "current propagation constant", $\tilde{\beta}$, to describe the current distribution, we obtain:

$$j_r(r,\theta,z) = -\frac{f(r)}{r}[1-\cos(2\gamma\theta_s + 4\tilde{\beta}l)]\delta(z+l)[\delta(\theta-\theta_a)+\delta(\theta+\theta_a)] \ ,$$

where $f(r)$ is given by Eq. (B.4), $\gamma = \tilde{\beta}s$, $\theta_s = \theta_a + \theta_b$ (θ_a and θ_b are shown in Fig. B.4).

Since $j_\theta(-\theta) = -j_\theta(\theta)$, we present j_θ for $\theta > 0$ only:

$$\begin{aligned} j_\theta(r,\theta>0,z) = D(r)\Big\{ & \delta(z-l)U(0\le\theta\le\theta_s)\cos(\gamma\theta+\phi_2) \\ & -\delta(z+l)\Big[U(0\le\theta\le\theta_a)\cos(\gamma(\theta-\theta_a)) \\ & +U(\theta_a\le\theta\le\theta_s)\cos(\gamma\theta-\phi_1)\Big]\Big\}, \end{aligned}$$

where $\phi_1 = \gamma(2\theta_s+\theta_a)+4\tilde{\beta}l$, $\phi_2 = \gamma\theta_a + 2\tilde{\beta}l$,

$$\begin{aligned} j_z(r,\theta,z) = \frac{D(r)}{r}U(-l\le z\le l)\Big\{ & 2\delta(\theta)\cos[\tilde{\beta}(z+l)+\gamma\theta_a] \\ & -[\delta(\theta-\theta_s)+\delta(\theta+\theta_s)]\cos[\tilde{\beta}(3l-z)+\gamma(\theta_a+\theta_s)]\Big\} \end{aligned}$$

This yields

$$j_r(r,m,k_z) = -\frac{f(r)}{2\pi^2 r}\left[1-\cos(\phi_1-\gamma\theta_a)\right]e^{ik_z l}\cos(m\theta_a) \ , \tag{B.8}$$

$$\begin{aligned} j_\theta(r,m,k_z) = \frac{iD(r)}{2\pi^2}\Bigg\{ & e^{ik_z l}\Bigg[\frac{2m}{\gamma^2-m^2}\sin\left(\frac{\gamma+m}{2}\theta_a\right)\sin\left(\frac{\gamma-m}{2}\theta_a\right) \\ & +\frac{1}{\gamma+m}\sin\left(\frac{\gamma+m}{2}\theta_b\right)\sin\left(\frac{\gamma+m}{2}(\theta_a+\theta_s)-\phi_1\right) \end{aligned}$$

$$-\frac{1}{\gamma-m}\sin\left(\frac{\gamma-m}{2}\theta_b\right)\sin\left(\frac{\gamma-m}{2}(\theta_a+\theta_s)-\phi_1\right)\Bigg]$$
$$+e^{-ik_z l}\Bigg[\frac{-1}{\gamma+m}\sin\left(\frac{\gamma+m}{2}\theta_s\right)\sin\left(\frac{\gamma+m}{2}\theta_s+\phi_2\right)$$
$$+\frac{1}{\gamma-m}\sin\left(\frac{\gamma-m}{2}\theta_s\right)\sin\left(\frac{\gamma-m}{2}\theta_s+\phi_2\right)\Bigg]\Bigg\} \qquad \text{(B.9)}$$

(for $\{m=0,\ \gamma\neq 0\}\quad j_\theta(r,m,k_z)=0$),

$$j_z(r,m,k_z)=\frac{D(r)}{2\pi^2 r}\Bigg\{\frac{\sin((\tilde{\beta}+k_z)l)}{\tilde{\beta}+k_z}\Big[e^{-i(\gamma\theta_a+\tilde{\beta}l)}-\cos(m\theta_s)e^{i[\gamma(\theta_a+\theta_s)+3\tilde{\beta}l]}\Big]$$
$$+\frac{\sin((\tilde{\beta}-k_z)l)}{\tilde{\beta}-k_z}\Big[e^{i(\gamma\theta_a+\tilde{\beta}l)}-\cos(m\theta_s)e^{-i[\gamma(\theta_a+\theta_s)+3\tilde{\beta}l]}\Big]\Bigg\}\ . \qquad \text{(B.10)}$$

Appropriate limits must be taken in Eq. (B.9) for $\gamma^2=m^2$ and in Eq. (B.10) for $\tilde{\beta}^2=k_z^2$. It is easy to obtain $\nabla\cdot\mathbf{j}(r,m,k_z)$ from Eqs. (B.8) — (B.10) if we note that $f'(r)=D(r)$ (Eq. (B.4)).

For $\tilde{\beta}=0$ ($\nabla\cdot\mathbf{j}=0$) the above spectrum is much simpler:

$$j_r(r,m,k_z)=0\ ,$$

$$j_z(r,m,k_z)=\frac{D(r)}{\pi^2 r}\frac{\sin(k_z l)}{k_z}[1-\cos(m\theta_s)]\ ,$$

$$j_\theta(r,m,k_z)=\begin{cases}-\dfrac{rk_z}{m}j_z(r,m,k_z) & \text{for}\quad m\neq 0\\[2ex] 0 & \text{for}\quad m=0\ .\end{cases}$$

Appendix C

Code UFEM

In this Section we present a short description of the code UFEM designed on the theoretical basis presented in § 4.3.

The code UFEM solves the wave equations in 1D cylindrical geometry with a warm plasma column, a conducting wall and an optional vacuum layer. Four different variations of cylindrical geometry can be employed (Appendix A). The plasma composition, the number of ion species and the radial profiles of plasma parameters can be almost arbitrary. UFEM can use an arbitrary antenna geometry and the antenna can have an arbitrary location (in the plasma and/or in a vacuum). The code can account for antenna charge (if applicable), so non-divergence-free antennas can be studied (an example is that of an antenna in contact with the plasma and capable of drawing sheath current). Ten antenna types have been pre-programmed in the code (3 of which can be non-divergence-free), each of them can be selected by a simple switch.

Radial and k_z-meshes used in the code can be almost arbitrary. The number of m- and k_z- modes in the spectrum can be arbitrary and is limited only by the available computer memory and speed. The memory requirements have been minimized so that even in the most complicated cases the memory consumption does not usually exceed 100 MB. The code is rather efficient: with 100 — 500 radial mesh points and several hundreds of (m, k_z)-modes, in DEC Alpha workstations it works practically in "real time" (1 — 5 minutes per run). This makes the code especially suitable for realistic antennas which have broad k_z-spectra and which can, in principle, deposit significant energy in high $k_\perp$ modes.

The code is rather compact (about 230 kB of source text files). The code is also quite transparent and so not difficult to understand and modify, if necessary. The code is also supplied with comprehensive "*User's Guide*". Both the code and the guide can be requested from the author.[1]

A significant effort has been made to make the code easily transportable, reliable

[1]Can be also downloaded from `http://rsphysse.anu.edu.au/~ivk112/`

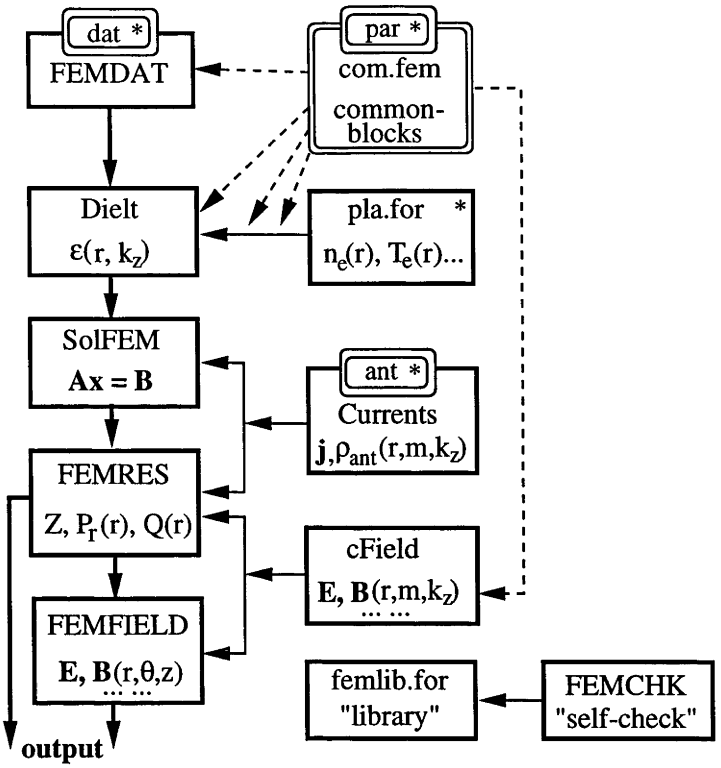

Figure C.1: Structure of the code UFEM. Double squares designate include-files, asterisk designates the task input.

and user-friendly. The code is written in standard ANSI Fortran–77. It does not need any external libraries. The code performs some self-checks in each run and is sufficiently "fool-proof" that many possible user mistakes in the input (such as formally incorrect r- or k_z- mesh, locally negative density or temperature, not quasi-neutral plasma, etc.) are automatically detected.

UFEM can compute the antenna impedance and its spectrum over m- and k_z-modes, the Poynting vector flux and the total power deposition (§ 4.4), the uniform plasma dispersion (Eq. (4.17)) and the wave field structure which includes all wave field components ($\mathbf{E}$, $\mathbf{B}$, $\mathbf{A}$, ϕ), the wave-induced current in plasma, $\mathbf{j}$, the local power deposition (§ 4.4) and the "pollution factor", $a|\nabla \cdot \mathbf{A}|/|\mathbf{A}|$ (§ 4.5). The latter characteristics of the wave field can be produced as 1D profiles over r, θ or z at an arbitrary location, as well as 2D contour plots in any azimuthal or axial cross-section or on a cylindrical surface.

The code structure is presented in Fig. C.1. The code input (see below) is organized with the use of include-files making it flexible and transparent. A part of the input is arranged so that the user can choose which input parameters to pre-set and which to enter interactively. The radial profiles of plasma parameters are set (in the file "pla.for") in 3 functions (the plasma density, $n_e(r)$, the neutrals' density, $n_n(r)$, and the electron temperature, $T_e(r)$) and 2 subroutines (the ion temperatures,

$T_i(r)$, and ion fractions, $n_i(r)/n_e(r)$, for all ion species) which can be defined by the user as almost arbitrary functions of r. Artificial collisions in a thin layer can be set to facilitate the numerical resolution of a very sharp field variation which may occur at the plasma edge and/or at a resonance in plasma in the case of weak dissipation.

The "library" (file "femlib.for") includes all the necessary subroutines; no external libraries are required which makes the main, Fortran part of the code fully transportable. In particular, it contains 4 functions which facilitate the construction of proper radial profiles of plasma parameters using "experimental" points with the use of cubic interpolation and adjustable smoothing. It also contains the plasma dispersion function (§ 4.1), real and complex error functions and the function $w(z)$ [1]. Three subroutines perform the solution of the linear system of equations which has a complex band matrix structure using Gaussian elimination with matrix renormalization (pre-conditioning). Only the matrix band part is used and memorized. A special library subroutine "FEMCHK" (Fig. C.1) performs the elementary "self-check" of several other library subroutines in each code run to trace their possible corruption.

All main subroutines (Fig. C.1) are interfaced through the include-file "com.fem" which contains a number of common-blocks and description operators for their variables. This is the data "store" for the subroutines.

The subroutine "FEMDAT" arranges the task input and the "dialogue" with the user, performs some checks of the input data, and makes some preliminary computations.

The subroutine "Dielt" computes 3 components of the plasma dielectric tensor $\varepsilon_{1,2,3}(r, k_z)$ (Eq. (4.2)) on a r-mesh which is twice as dense as the basic one (necessary to compute the coefficients in Eqs. (4.34) — (4.37)) and performs the formal check of plasma parameters.

The subroutine "Currents" computes Fourier-transformed antenna current density components (j_r, j_θ and j_z) and $\nabla \cdot \mathbf{j}$ for 10 antenna types. Antenna type and parameters are set in the include-file "ant".

The subroutine "SolFEM" constructs, using the finite element method, the linear system of equations (4.34) — (4.37) and solves it. As a result, it produces Fourier-harmonics of potentials $\{\mathbf{A}, \phi\}(r, m, k_z)$. The subroutine is well optimized and the computation is efficiently parallelisable.

The function "cField" computes Fourier-harmonics of the field components, $\mathbf{E}$, $\mathbf{B}$, $\mathbf{j}$ (the wave-induced current) and $\nabla \cdot \mathbf{A}$ using the potentials ($\mathbf{A}$, ϕ). Special care is taken in the computation of the radial derivatives of the potentials: the formulae for the 5-point differentiation of the polynomials of best quadratic mean approximation ([87], § 20.6-1) are used to minimize numerical errors.

The subroutine "FEMRES" computes the antenna impedance, its m- and k_z-spectra, the Poynting vector flux, $P_r(r)$, and the total power deposition, $Q(r)$ (§

4.4).

The subroutine "FEMFIELD" computes the wave field and power deposition structure in real space using the inverse Fourier-transform of the field Fourier-harmonics. The inverse Fourier-transform is organized so that to maximize the advantage resulting from the fact that one (for contour plots) or two (for 1D profiles) coordinates (r, θ or z) are constant. Up to 6 field components (necessary to compute the local power deposition) are inverted simultaneously.

The graphic interface for the code is provided (starting from the code version 1 (25.11.97)) by the program written in IDL[2] (version 4.0.1). In particular, it contains a program for the animation of the wave propagation (for any field component) which is convenient for a qualitative analysis. If IDL is not available for the user, the structure of the output data files (which is very simple) is explained in the User's Guide. The files containing the data for 1D (r- θ- and z-) profiles can be also used in GNUPLOT[3] or GRAPHER[4] directly, without any adjustments.

In the rest of this Section we present an example of the code input (files "dat", "par", "ant" and "pla.for") to demonstrate the code's abilities and the code "appearance" for an external user. The code output produced with this input is (partially) presented in Figs. 5.6 — 5.11.

```
c$$$$$$$$$$$$$$ File "dat",  code UFEM 1  Version 25.11.97 $$$$$$$$$$
       DATA
c$$$$$$$$$$$$$$$$$$$$$$$$$$$ 1.TASK PARAMETERS: $$$$$$$$$$$$$$$$$$$$$
     . Version  /
     . 'UFEM 1: WOMBAT, Bo = 50 G                    Te(r) = const '
     .,'  100% Ar+,  Nn(p_fill=0.92mTorr) = const, Ti = 0          '
     .,'  Ne(r)/Ne(0) = 0.2 + 0.8*[1 - (r/a)**2]                    '/
c      '<------------------ ( up to 60 symbols ) ----------------->'

     .,     a / 9.     /!  Plasma edge radius,      [cm]
     ., a_wall/.true.  /!  There is a (glass) wall at r = a
                       !    (.true./.false.) (To account for e-wall
                       !     collisions set dr < rho_e  near  r = a)
     .,     b / 18.5   /!  Conducting wall radius, [cm]
     .,   Rtor/  1.    /!  Torus major radius,      [cm]
                       !    For continuous Kz-spectrum set Rtor = 1.
                       !    For finite cylinder of length L set
                       !              Rtor = L/pi # 1.
     .,    Zagc/ 7.5   /! "z", [cm]  of the antenna geometric center,
                       !    if there is a conducting plate at z = 0.
                       !    For infinite cylinder or torus set Zagc=0.

     .,     f / 13.56 /!  Frequency, [MHz]
     .,    Io /  50.   /!  Peak amplitude of antenna current, [A]
```

[2]© Research Systems, Inc.

[3]© Borland (T. Williams and C. Kelley)

[4]© Golden Software, Inc.

```
c    "Active" (non-zero) antenna m-modes (total number = ma_max):
     .,  m_act/ -3, -1, 1, 3 /

c--------------------------- Plasma: -------------------------------
     .,   Neo / 3.e11   /!  Central plasma density,          [cm-3]
     .,   Teo / 3.      /!  Central electron temperature,    [eV]
     .,    Bo / 0.005   /!  Constant axial magnetic field,  [T]
     .,   Nna / 2.97e13 /!  Neutrals' density at r = a,     [cm-3]

c    Plasma composition ("Nfrac" species):
     .,   Mi/ 40. /!  Ion masses, [at.un.]
     .,   Zi/  1  /!  Ion charges
     .,   Tio/ 0. /!  Central ion temperatures, [eV]

c          ---------- Artificial ion collisions: ----------
c ------------ Near r = a: --------
     .,  fci_a  / 0.  /!   (Collision frequency)/Omega  at r = a
     .,  sig_a  / 0.2 /!   'sigma' of Gaussian profile, [cm]
c ------------ Near LHR: ----------
     .,  fci_LHR/ 0.  /!   (Collision frequency)/Omega  at r = r_LHR
     .,  sig_LHR/ 0.2 /!   'sigma' of Gaussian profile, [cm]
     .,    r_LHR/ 1.9 /!   'Central' r, [cm]

c======================== Output configuration: ====================
c-------- Set 1/0 if you need/needn't the "field component": --------

c       ----- The wave electric (E) and magnetic (B) field: --------
c                E_r    E_theta    E_z    B_r    B_theta    B_z
     .,Ifield/   0 ,       0 ,     1 ,    0 ,      0 ,      0

c       ----- The wave vector (A) and scalar (phi) potentials: -----
c                A_r    A_theta    A_z    phi    a*|div(A)|/|A|
     .,          0 ,      0 ,      0 ,    0 ,       0

c       ----- Wave-induced currents (J) in plasma: -----------------
c                J_r    J_theta    J_z    local power deposition
     .,          0 ,      0 ,      1 ,          1             /

     .,    iaph /  2 / !  Set +2  to get the field amplitude & phase
                       !      -1  - - - - - - real & imaginary parts
                       ! (except a*|div(A)|/|A| and power deposition)

c------------------- Dialogue and output setting: -------------------
c    in_... =  1 - executed (without asking) with data pre-set here
c           =  0 - will ask to set data in dialogue
c           = -1 - will not ask and will not execute
c--------------------------------------------------------------------
     .,  in_ file Name  / 1 /  !  Main output file name:
     .,                           file Name /'result'/

c - - - - - - - - Graphic output: - - - - - - - - - - - - - -
     .,  in_ Ne /  0 /  !  Plots of Ne(r), Te(r), Nn(r)
                        !     & Ti(r) for 1st ion species
```

```
     .,  in_ Zs /  1 /  !  Antenna impedance & its spectrum
     .,  in_ Pr /  0 /  !  Total power deposition
                        !     & radial Poynting vector flux

     .,  in_ xy /  1 /  !  Wave field 1D profiles (skip if -1):
     .,  in_ Fr /  1 /  !    - radial profiles:
     .,                          theta r / 0.785 /,   Zr / 50. /
     .,  in_ Fa / -1 /  !    - azimuthal profiles:
     .,                          ra / 5. /,        Za / 30./
     .,  in_ Fz /  1  / !    - axial profiles:
     .,                          rz / 3.  /,       Zmin / 0. /
     .,                          theta z / 0. /,   Zmax / 200. /

     .,  in_ CP /  1 /  !  Contour plots (skip if -1):
     .,  in_ Pcs/  1 /  !    - azimuthal (poloidal) cross-section:
     .,                          Z_cs / 50. /
     .,  in_ Acs/  1 /  !    - axial cross-section:
     .,                          Zmin_cs /   0. /,   theta_cs / 0./
     .,                          Zmax_cs / 200. /
     .,  in_ Cs / -1 /  !    - cylindrical surface:
     .,                          rc / 18./
     .,                          thetaCs_min /-2./,  Zcs_min /-150./
     .,                          thetaCs_max / 2./,  Zcs_max / 150./

c============================ r-mesh, [cm]: ========================
c          Desired:  r(1) > 0,   r(Nr_max) = b,   r(i+1) > r(i)

                   r(1) = 0.01
                   r(2) = 0.05
      do i = 3, Nr_max
                     dr = 0.05
        if(i.gt.179) dr = 0.02
        if(i.gt.184) dr = 0.05
        r(i) = r(i-1) + dr
      enddo
c---------------------------------------------------------------------
c  The radius to match with asymptotic solution at r -> 0 for |m|>2
                        r_m = 0.5        !  [cm]

c========================== Kz-mesh, [1/cm]: =======================
c--------------- ( Set for continuous Kz-spectrum only ) ------------
                       IF(Rtor.eq.1.) THEN
c Desired: Kz(n+1) > Kz(n);  Keep 2*pi/max.dKz >> the system z-length

              Kz(0) = 0
             do n = 1, n_max
              Kz( n) =  Kz(n-1) + 0.002
              Kz(-n) = -Kz(n)
             enddo
                       ENDIF

c-------------------- Uniform plasma dispersion: --------------------
        in_ disp = -1    !   r-profiles for K_perp**2 of SW & FW
```

```
        Kz_disp = 0.2    !    [1/cm]


c$$$$$$$$$$$ File "par",  code UFEM 1  Version 25.11.97 $$$$$$$$$$$
      PARAMETER(
c$$$$$$$$$$$$$$$$$$$$$$  2.TASK PARAMETERS:  $$$$$$$$$$$$$$$$$$$$$$
c                        (Dimensions of arrays)

     .  Nr_max  =  374 ! - Number of r-mesh points
     ., ma_max  =   4  ! - Number of "active" (non-zero) m-modes
     .,  n_min  = -200 ! - Min. &  max. indices of Kz(n)
     .,  n_max  =  200 !     for continuous spectrum  n_max > n_min
                       !     if  Zagc # 0  set  n_min = -n_max

     .,  Nfrac  =  1   ! - Number of ion species
c( If you have changed Nfrac, check subroutines "Frac_i" & "Prof_Ti")

c------ Number of points for plots: --------------------------------
     .,      Nt = 150  ! - Number of theta-mesh points
                       !     for both "y" vs "x" & contour plots
     .,      Nz = 801  ! - Number of z-mesh points
                       !     for 1D z-profiles only
c    - - - - - - - - for contour plots only: - - - - - - - -
     ., Nr_maxa = 374  ! - Max. index of r(i) for cross-section plots
     ., Nr_rar  =  2   !     r-mesh rarefaction step for these plots
     .,     Nza = 801 )! - Number of z-mesh points for axial cross-
                       !     section and cylindrical surface

c%%%%%%%%%%%% The memory used by the task is about %%%%%%%%%%%%%%%
c         32*Nr_max*{(ma_max + 1.5)*(n_max - n_min + 1) + 32}
c       + 8*{Nr_maxa*(2*Nza + Nt)/Nr_rar + Nza*Nt}      bytes
c%%%%%%%%%%%%%%%%%%%%%%%%%%%%%%%%%%%%%%%%%%%%%%%%%%%%%%%%%%%%%%%%


c$$$$$$$$$$$$$ File "ant",  code UFEM 1  Version 25.11.97 $$$$$$$$$
      parameter(
c------------- Antenna parameters (dimensions in [cm]):--------------
     .        s = 9.7    ! radius of inner antenna edge
     .,       d = 0.3    ! antenna radial thickness (wire diameter)
     .,       l = 13.5   ! 1/2 of antenna z-length (for No.1,2,4,7,8)
     .,      s1 = 24.7   ! radius of outer antenna edge (for No.4,6)
     .,  lambda = 18.    ! z-length of 1 helical turn (for No.1,7)
     ., theta_a = pi/4.  ! azimuthal angle, [rad] (for No.2,8)
     ., theta_b = 1.3    ! - - - - - - - - - - - -  (for No.8)
     ., phase_d = 0.     ! phase difference, [rad] (for No.9)
     .,   cbeta = (0,0)  ! current propagation constant, [1/cm]
                         !  (j ~ cos(cbeta*x) along antenna length x)
c-----------------------------------------------------------------------
     .,                                Antenna No = 3    )
      data          Antenna type                    /!   :
     .     'BASIL-type helical antenna:    ' !   1
     .,    'Double saddle coil:            ' !   2
     .,    'Degeling antenna:              ' !   3  *
```

```
     .,    'Pi/2 single strip FW antenna: ' !   4
     .,    'Single loop:                  ' !   5  *
     .,    'Double half-turn antenna:     ' !   6
     .,    'Helical antenna:              ' !   7
     .,    'H1-type double saddle coil:   ' !   8  *
     .,    '2 phased double saddle coils: ' !   9
     .,    'K.Appert''s helical antenna:  '/!  10
c-------------------------------------------------------------------
c         * - accepts  cbeta # 0 (i.e. div(j) # 0 )


c$$$$$$$$$$$$ File "pla.for",  code UFEM 1  Version 25.11.97 $$$$$$$$
c$$$$$$$$$$$$$$$$$$ Radial profiles of plasma parameters $$$$$$$$$$$$$
      FUNCTION  Prof_Ne(r, a)
c=============== Electron density profile Ne(r)/Ne(0): ==============
c============  r - radius,  a - plasma edge radius,  [cm] ===========
c============ Desired: Prof_Ne(r<a) > 0,  flat at r -> 0  ===========
c====================================================================

       Prof_Ne = 0.2 + 0.8*(1.- (r/a)**2)
      end


      FUNCTION  Prof_Nn(r, a)
c========== Neutral particles' density profile Nn(r)/Nn(a)  =========
c============  r - radius,  a - plasma edge radius,  [cm] ===========
c==================== Desired: Prof_Nn(r<a) > 0 ====================

       Prof_Nn = 1.
      end


      FUNCTION  Prof_Te(r, a)
c============   Electron temperature profile Te(r)/Te(0)  ===========
c============  r - radius,  a - plasma edge radius,  [cm] ===========
c==================== Desired: Prof_Te(r<a) > 0 ====================

       Prof_Te = 1.
      end


      SUBROUTINE  Prof_Ti(r, a, Pr_Ti, Nfrac)
c====================== Ion temperature profiles: ==================
c============  r - radius,  a - plasma edge radius,  [cm]  ==========
c============  Pr_Ti(r,i) = Ti(r)/Ti(0),  i = 1, ... Nfrac ==========
c====================== Desired: Pr_Ti(r<a) > 0   ==================
       real Pr_Ti(Nfrac)

        Pr_Ti(1) = 1.
      end


      SUBROUTINE  Frac_i(r, a, frac, Nfrac)
```

```
c============================ Ion fractions: ========================
c============  r - radius,  a - plasma edge radius,  [cm] ===========
c========       frac(r,i) = Ni(r)/Ne(r),  i = 1, ... Nfrac      =====
c======== Keep  Sum( Zi*frac ) = 1 for plasma quasi-neutrality! =====
      real  frac(Nfrac)

       frac(1) = 1.
      end
```

Bibliography

[1] M. Abramowitz and I. A. Stegun, *Handbook on Mathematical Functions*, (Dower, New York, 1972).

[2] P. Aigrain, In: Proc. Internat. Conf. on Semiconductor Phys., Prague, 1960, p. 224.

[3] A. I. Akhiezer, I. A. Akhiezer, R. V. Polovin, A. G. Sitenko and K. N. Stepanov, *Plasma Electrodynamics*, (Pergamon Press, New York, 1975).

[4] D. V. Anderson, W. A. Cooper, R. Gruber, S. Merazzi and U. Schwenn, Int. J. Supercomp. Appl. **4**, 34 (1990).

[5] K. Appert, B. Balet, R. Gruber, F. Troyon and J. Vaclavik, Comput. Phys. Commun. **24**, 329 (1981).

[6] K. Appert, J. Vaclavik and L. Villard, *An Introduction to the Theory of Alfvén Wave Heating*, Lecture notes, LRP 238/84, CRPP, Lausanne, 1984.

[7] K. Appert, T. Hellsten, J. Vaclavik and L. Villard, Comput. Phys. Commun. **40**, 73 (1986).

[8] M. J. Ballico and R. C. Cross, Plasma Phys. Controlled Fusion **31**, 1141 (1989).

[9] J. F. Bamber, W. Gekelman and J. E. Maggs, Phys. Rev. Lett. **73**, 2990 (1994).

[10] D. B. Batchelor, E. F. Jaeger and H. Weitzner, in: *Theory of Fusion Plasmas*, Proc. Int. Workshop, (Varenna, 1988), p. 691 (Editrice Compositori, Bologna, 1988).

[11] P. L. Bhatnagar, E. P. Gross and M. Krook, Phys. Rev. **94**, 511 (1954).

[12] H. A. Blevin and P. J. Christiansen, Australian J. Phys. **19**, 501 (1966).

[13] G. G. Borg, Plasma Phys. Controlled Fusion **36**, 1419 (1994).

[14] G. G. Borg, Bull. Am. Phys. Soc. **40**(11), 1683 (1995).

[15] G. G. Borg and R. W. Boswell, *Power Coupling to Helicon and Trivelpiece-Gould Modes in Helicon Sources*, accepted for publication in *Phys. Plasmas.*

[16] G. G. Borg, B. D. Blackwell, S. M. Hamberger, D. Rudakov, D. A. Schneider, L. E. Sharp, M. Shats and B. C. Zhang, Fusion Engineering and Design **26**, 191 (1995).

[17] G. G. Borg, J. Bright and I. V. Kamenski, *Collisionless Energy Coupling to High Velocity Electrons in the Near Field of an Antenna: Neutral Gas Ionisation by Helicon Waves*, accepted for publication in *Plasma Phys. Controlled Fusion.*

[18] G. G. Borg and I. V. Kamenski, Phys. Plasmas **4**, 529 (1997).

[19] G. G. Borg, D. A. Schneider and I. V. Kamenski, Bull. Am. Phys. Soc. **40**(11), 1679 (1995).

[20] R. W. Boswell, Phys. Lett. **33**A, 457 (1970).

[21] R. W. Boswell, *A Study of Waves in Gaseous Plasma*, PhD thesis, Flinders University, 1970.

[22] R. W. Boswell, Nature, **258**, 58 (1975).

[23] R. W. Boswell, J. Plasma Phys. **31**, 197 (1984).

[24] R. W. Boswell, Plasma Phys. Controlled Fusion **26**, 1147 (1984).

[25] R. W. Boswell and D. Henry, Appl. Phys. Lett. **47**, 1095 (1985).

[26] R. W. Boswell, R. K. Porteous, A. Prytz, A. Bouchoule and P. Ranson, Phys. Lett. **91A**, 163 (1982).

[27] R. W. Boswell and R. K. Porteous, Appl. Phys. Lett. **50**, 1130 (1987).

[28] M. Brambilla and M. Ottaviani, Plasma Phys. Controlled Fusion **27**, 1 (1985).

[29] M. Brambilla, Phys. Plasmas **2**, 1094 (1995).

[30] S. Brunner and J. Vaclavik, Phys. Fluids **B5**, 1695 (1993).

[31] M. D. Carter, D. A. Rasmussen, P. M. Ryan, G. R. Hanson, D. C. Stallings, D. B. Batchelor, T. S. Bigelow, A. C. England, D. J. Hoffman, M. Murakami, C. Y. Wang, J. B. Wilgen, J. H. Rogers, J. R. Wilson, R. Majeski and G. Schilling, Nucl. Fusion, **36**(2), 209 (1996).

[32] B. W. Char, *MAPLE-V Language Reference Manual*, (Springer–Verlag, New York, 1991).

[33] F. F. Chen, *Introduction to Plasma Physics and Controlled Fusion*, (Plenum Press, 1984).

[34] F. F. Chen, Phys. Scr. **T30**, 14 (1990).

[35] F. F. Chen, Plasma Phys. Controlled Fusion **33**, 339 (1991).

[36] F. F. Chen, J. Vacuum Sci. Technol. **A10**, 1389 (1992).

[37] F. F. Chen and D. Arnush, Phys. Plasmas **4**, 3411 (1997).

[38] F. F. Chen and C. D. Decker, Plasma Phys. Controlled Fusion **34**, 635 (1992).

[39] F. F. Chen, M.-K. J. Hsieh and M. Light, Plasma Sources Sci. Technol. **3**, 49 (1994).

[40] F. F. Chen, I. D. Sudit and M. Light, Plasma Sources Sci. Technol. **5**, 173 (1996).

[41] R. T. S. Chen, R. A. Breun, N. Hershkowitz and M.-K. J. Hsieh, Plasma Sources Sci. Technol. **4**, 337 (1996).

[42] S. C. Chiu and T. K. Mau, Nucl. Fusion **23**, 1613 (1983).

[43] S. Cho and J.-G. Kwak, Phys. Plasmas **4**, 4167 (1997).

[44] P. L. Colestock and R. J. Kashuba, Nucl. Fusion **23**, 763 (1983).

[45] G. A. Collins, N. F. Cramer and I. J. Donnelly, Plasma Phys. Controlled Fusion **28**, 597 (1986).

[46] R. C. Cross, *An Introduction to Alfvén Waves*, (Adam Hilger, Bristol, 1988).

[47] B. Davies and P. J. Christiansen, Plasma Phys. **11**, 987 (1969).

[48] A. W. Degeling, C. O. Jung, R. W. Boswell and A. R. Ellingboe, Phys. Plasmas **3**, 2788 (1996).

[49] A. W. Degeling, N. Mikhelson, R. W. Boswell and N. Sadeghi, *Characterisation of Helicon Waves in a Magnetised Inductive Discharge*, accepted for publication in *Phys. Plasmas.*

[50] A. N. Dellis and J. M. Weaver, Proc. Phys. Soc. **83**, 473 (1964).

[51] V. V. Dolgopolov, A. I. Ermakov, N. I. Nazarov, K. N. Stepanov and V. T. Tolok, Nucl. Fusion **3**, 296 (1963).

[52] A. Durandet, R. W. Boswell and D. McKenzie, Rev. Sci. Instrum. **66**, 2908 (1995).

[53] A. R. Ellingboe, J. P. Booth, N. Sadeghi and R. W. Boswell, Phys. Plasmas **2**, 1807 (1995).

[54] A. R. Ellingboe and R. W. Boswell, Phys. Plasmas **3**, 2797 (1996).

[55] A. R. Ellingboe, *Waves and Power Absorbtion in a Magneto-Plasma*, PhD thesis, ANU, Canberra, Jan. 1998.

[56] R. L. Ferrari and J. P. Klozenberg, J. Plasma Phys. **2**, 283 (1968).

[57] B. Fischer, M. Kramer and T. Enk, Plasma Phys. Controlled Fusion **36**, 2003 (1994).

[58] J. L. A. Francey and D. J. Gates, J. Phys. **A1**, 710 (1968).

[59] B. D. Fried and S. D. Conte, *The Plasma Dispersion Function*, (Academic Press, New York, 1961).

[60] R. M. Gallet, J. M. Richardson, B. Wieder, G. D. Ward and G. N. Harding, Phys. Rev. Lett. **4**, 347 (1960).

[61] V. E. Golant and V. I. Fedorov, *RF Plasma Heating in Toroidal Fusion Devices*, (Consultants Bureau, New York, 1989).

[62] R. Gruber and J. Rappaz, *Finite Element Methods in Linear Ideal Magnetohydrodynamics*, (Springer-Verlag, Berlin, 1985).

[63] R. Gruber, J. Comput. Phys. **26**, 379 (1978).

[64] S. M. Hamberger, B. D. Blackwell, L. E. Sharp and D. B. Shenton, Fusion Technol. **17**, 123 (1990).

[65] B. M. Harvey and C. N. Lashmore-Davies, Phys. Fluids **B5**, 3864 (1993).

[66] S. P. Hirshman and O. Betancourt, J. Comput. Phys., **96**, 99 (1991).

[67] W. M. Hooke, M. A. Rothman, P. Avivi and J. Adam, Phys. Fluids **5**, 864 (1962).

[68] J. R. Houck and R. Bowers, Phys. Rev. **166**, 397 (1968).

[69] J. D. Huba, *NRL Plasma Formulary*, (Naval Research Lab., Washington DC, 1994).

[70] S. W. Hui, Brit. J. Appl. Phys. **17**, 1405 (1966).

[71] S. W. Hui, Phys. Rev. Lett. A**24**, 265 (1967).

[72] T. Intrator, S. Meassick, J. Browning, R. Majeski, J. R. Ferron and N. Hershkowitz, Nucl. Fusion **29**, 377 (1989).

[73] A. Jaun, *Linear Wave Propagation in a Hot Axisymmetric Toroidal Plasma*, PhD thesis, Report LRP 513/95, CRPP, Lausanne, March 1995.

[74] A. Jaun, K. Appert, J. Vaclavik and L. Villard, Comput. Phys. Commun. **92**, 153 (1995).

[75] A. Jaun, K. Appert and J. Vaclavik, *Pollution Free Discretization of Maxwell's Equations in Terms of Potentials*, Report LRP 492/94, CRPP, Lausanne, March 1994.

[76] D. F. Jephcott and A. Malein, Proc. Roy. Soc. A**278**, 243 (1963).

[77] I. V. Kamenski and G. G. Borg, Phys. Plasmas **3**, 4396 (1996).

[78] I. V. Kamenski and G. G. Borg, *A 1D Cylindrical Kinetic Wave Code for Helicon Plasma Sources*, submitted to *Comput. Phys. Commun.*, 1998.

[79] C. F. F. Karney and A. Bers, Phys. Rev. Lett. **39**, 550 (1977).

[80] C. F. F. Karney, Phys. Fluids **21**, 1584 (1978).

[81] C. F. F. Karney, Phys. Fluids **22**, 2188 (1979).

[82] V. P. Katyukha, G. S. Kirichenko, A. V. Rusavskii, V. B. Taranov and K. P. Shamrai, Rev. Sci. Instrum. **65**, 1368 (1994).

[83] P. A. Keifer, E. E. Scime and M. M. Balkey, Phys. Plasmas **4**, 2741 (1997).

[84] J. H. Kim, S. M. Yun and H. Y. Chang, IEEE Trans. Plasma Sci. **1**, 999 (1996).

[85] J. P. Klozenberg, B. McNamara and P. C. Thonemann, J. Fluid Mech., **21**, 545 (1965).

[86] A. Komori, T. Shoji, K. Miyamoto, J. Kawai and Y. Kawai, Phys. Fluids **B3**, 893 (1991).

[87] G. A. Korn and T. M. Korn, *Mathematical Handbook for Scientists and Engineers*, (McGraw-Hill, New York, 1961).

[88] M. Koshiba, K. Hayata and M. Suzuki, IEEE Trans. Microwave Theory Tech. v. MTT-30, 900 (1985).

[89] I. A. Kovan, B. I. Patrushev, V. D. Rusanov, V. P. Smirnov and D. A. Frank-Kamenetsky, in: Proc. IAEA Conf. on Plasma Phys. and Controlled Fusion, Vienna 1962, v. 3, p. 1067.

[90] C. R. Legendy, Phys. Rev. **135**(6A), 1713 (1964).

[91] J. A. Lehane and P. C. Thonemann, Proc. Phys. Soc. **85**, 301 (1965).

[92] M. A. Lieberman and R. A. Gottscho, *Physics of Thin Films*, (Academic Press, New York, 1994).

[93] M. A. Lieberman and R. A. Gottscho, *Design of High Density Plasma Sources for Materials Processing*, Report UCB/ERL M93/3, University of California, Berkley, 1993.

[94] M. A. Lieberman and A. J. Lichtenberg, *Principles of Plasma Discharges and Materials Processing*, (John Wiley, New York, 1994), Chap. 13.

[95] M. Light and F. F. Chen, Phys. Plasmas **2**, 1084 (1995).

[96] X. Llobet, K. Appert and J. Vaclavik, in: *Theory of Fusion Plasmas*, Proc. Int. Workshop, (Varenna, 1990), (Editrice Compositori, Bologna, 1990).

[97] P. K. Loewenhardt, B. D. Blackwell, R. W. Boswell, G. D. Conway and S. M. Hamberger, Phys. Rev. Lett. **67**, 2792 (1991).

[98] P. K. Loewenhardt, B. D. Blackwell and S. M. Hamberger, Phys. Plasmas **1**, 875 (1994).

[99] B. D. McVey, *ICRF Antenna Coupling Theory for a Cylindrically Stratified Plasma*, Report PFC/RR-84-12, Plasma Fusion Center, Massachusetts Inst. of Technol. (1984).

[100] B. D. McVey, *ANTENA User Guide*, Report PFC/RR-84-13, Plasma Fusion Center, Massachusetts Inst. of Technol. (1984).

[101] B. D. McVey, R. S. Sund and J. E. Scharer, Phys. Rev. Lett. **55**, 507 (1985).

[102] Y. Mouzouris and J. E. Scharer, IEEE Trans. Plasma Sci. **24**, 152 (1996).

[103] N. I. Nazarov, A. I. Ermakov, V. V. Dolgopolov, K. N. Stepanov and V. T. Tolok, Nucl. Fusion **3**, 255 (1963).

[104] K. D. Paulsen and D. R. Lynch, IEEE Trans. Microwave Theory Tech. v. MTT-39, 395 (1991).

[105] P. Pavlo, V. Petržílka, J. A. Tataronis, G. G. Borg, I. V. Kamenski and L. Krlín, *Nonlinear Density Profile Changes in Helicon Wave Plasmas*, 24th EPS Conf. on Controlled Fusion and Plasma Physics, Berchtesgaden (Germany), 9–13 June 1997.

[106] A. J. Perry and R. W. Boswell, Appl. Phys. Lett. **55**, 148 (1989).

[107] A. J. Perry, D. Vender and R. W. Boswell, J. Vac. Sci. Technol. **B9**, 310 (1991).

[108] V. Petržílka, Austr. J. Phys. **47**, 315 (1994).

[109] B. M. A. Rahman and J. B. Davies, IEEE Trans. Microwave Theory Tech. v. MTT-32, 922 (1984).

[110] S. Sazhin, *Whistler-mode Waves in a Hot Plasma*, (Cambridge University Press, 1993).

[111] D. A. Schneider, *Helicon Waves in High Density Plasmas*, PhD thesis, ANU, Canberra, Jan. 1998.

[112] D. A. Schneider, G. G. Borg and I. V. Kamenski, *Measurements and Code Comparison of Wave Dispersion and Antenna Radiation Resistance for Helicon Waves in a High Density Cylindrical Plasma Source*, submitted to *Phys. Plasmas*, 1998.

[113] K. P. Shamrai and V. B. Taranov, Plasma Phys. Controlled Fusion **36**, 1719 (1994).

[114] K. P. Shamrai and V. B. Taranov, Plasma Sources Sci. Technol. **5**, 474 (1996).

[115] M. G. Shats, D. L. Rudakov, B. D. Blackwell, G. G. Borg, R. L. Dewar, S. M. Hamberger, J. Howard and L. E. Sharp, Phys. Rev. Lett. **77**, 4190 (1996).

[116] M. G. Shats, D. L. Rudakov, R. W. Boswell and G. G. Borg, Phys. Plasmas **4**, 3629 (1997).

[117] S. Shinohara, Y. Miyauchi and Y. Kawai, Plasma Phys. Controlled Fusion **37**, 1015 (1995).

[118] S. Shinohara, S. Takechi, N. Kaneda and Y. Kawai, Plasma Phys. Controlled Fusion **39**, 1479 (1997).

[119] T. Shoji, Y. Sakawa, S. Nakazawa, K. Kadota and T. Sato, Plasma Sources Sci. Technol. **2**, 5 (1993).

[120] D. N. Smithe, P. L. Colestock, R. J. Kashuba and T. Kammash, Nucl. Fusion **27**, 1319 (1987).

[121] C. Steinbruchel, J. Vac. Sci. Technol. **A8**, 1663 (1990).

[122] J. E. Stevens, M. J. Sowa and J. L. Cecchi, J. Vac. Sci. Technol. **A13**, 2476 (1995).

[123] T. H. Stix, *Waves in Plasmas*, (American Inst. of Phys., New York, 1992).

[124] L. R. O. Storey, Philos. Trans. **A 246**, 113 (1953).

[125] H. Sugai, M. Maruyama, M. Sato and S. Takeda, Phys. Fluids **21**, 690 (1978).

[126] D. W. Swain, R. I. Pinsker, F. W. Baity, M. D. Carter, J. S. deGrassie, E. J. Doyle, G. R. Hanson, K. W. Kim, R. A. Moyer and C. C. Petty, Nuclear Fusion **37**, 211 (1997).

[127] D. G. Swanson, *Plasma Waves*, (Academic Press, London, 1989).

[128] D. G. Swanson, Phys. Fluids **24**, 2035 (1981).

[129] J. A. Tataronis, V. Petržílka, G. G. Borg and I. V. Kamenski, *Nonlinear Propagation of Helicon Waves in Inhomogeneous Plasma Columns*, 18th Symp. Plasma Phys. Technol., Prague, 17–20 June 1997.

[130] J. A. Tataronis, V. Petržílka, G. G. Borg and I. V. Kamenski, *Nonlinear Propagation of Helicon Waves*, 50th Gaseous Electronics Conf. of APS (GEC-97), Madison, WI, USA, 6–9 Oct. 1997.

[131] A. W. Trivelpiece and R. W. Gould, J. Appl. Phys. **30**, 1784 (1959).

[132] J. Vaclavik and K. Appert, Plasma Phys. Controlled Fusion **29**, 257 (1987).

[133] J. Vaclavik and K. Appert, Nucl. Fusion **31**, 1945 (1991).

[134] V. L. Vdovin and I. V. Kamenskij, *3D Structure of FMS Waves in Large Scale Tokamak Plasma*, in the USSR Contribution to the 9th Session of the Phase IIA Part 2 of the INTOR Workshop, Group B (RF Heating and Current Drive), v.1, pp. 48–89, Vienna, May 1984. Rep. EURFUBRU/XII-1/84/EDV23.

[135] V. L. Vdovin and I. V. Kamenskij, *Modelling of ICR Heating in INTOR*, in the USSR Contribution to the 13th Session of the Phase IIA Part 2 of the INTOR Workshop, Group B, Chapter 4, pp. 73–127, Vienna, March 1986. Rep. EURFUBRU/XII-52/86/EDV13.

[136] V. L. Vdovin, T. Watari, and A. Fukuyama, *3D Maxwell–Vlasov Boundary Value Problem Solution in Stellarator Geometry in Ion Cyclotron Frequency Range*, Report NIFS-469, NIFS (Nagoya, Japan), Dec. 1996.

[137] V. L. Vdovin and I. V. Kamenskij, *3D Electromagnetic Theory of ITER ICRF Multi Port Multi Loop Antenna*, ITER Progress Report, Physics Design Group, RNRC "Kurchatov Institute", Moscow, May 1996. IDOMS No. S 19 IP 2 97-01-28 F 1. Also: Report NIFS-479, NIFS, (Nagoya, Japan), Jan. 1997.

[138] L. Villard, K. Appert, R. Gruber and J. Vaclavik, Comput. Phys. Rep. **4**, 95 (1986).

[139] L. Villard, *Finite Element Methods Applied to Radiofrequency Waves*, Lecture Notes, CRPP, Lausanne, 1988.

[140] L. C. Woods, J. Fluid Mech. **13**, 570 (1962).

[141] E. Yamashita, *Analysis Methods for Electromagnetic Wave Problems*, (Artech House, Boston, 1990).

[142] B. C. Zhang, G. G. Borg and B. D. Blackwell, Phys. Plasmas **2**, 803 (1995).

[143] P. Zhu and R. W. Boswell, Phys. Rev. Lett. **63**, 2805 (1989).

[144] P. Zhu and R. W. Boswell, J. Appl. Phys. **68**, 1981 (1990).